# Nanoengineered Functional Structures for Photonic and Microfluidic Applications

by

**Long Chen**

A dissertation submitted in partial fulfillment
of the requirements for the degree of
Doctor of Philosophy
(Applied Physics)
in the University of Michigan
2017

Doctoral Committee:

Professor L. Jay Guo, Chair
Professor Mackillo Kira
Professor Cagliyan Kurdak
Professor Zetian Mi
Professor Nils G. Walter

*To my family:*

*Your love and dedication enabled everything*

# ACKNOWLEDGEMENTS

It has been an amazing and rewarding experience to study and reach this point at the University of Michigan – a place full of inspirations unending, resources unbounded, and people unforgettable. It is my greatest pleasure now to thank all who spurred, nurtured, and furthered this thesis work.

First of all, I would like to express my sincere gratitude to my PhD advisor: Professor L. Jay Guo. In the past few years, I have known Professor Guo as a sympathetic, rational and principle centered person, not to forget his undying love for breakthrough research. Professor Guo has been providing me invaluable guidance and support along my PhD study, and have taught me various things, including research methodologies, effective writing, presentation skills, etc. He has always been willing to give me great freedom to explore new ideas, and offer plenty of opportunities for both internal and external collaborations. His instructions, valuable ideas and continuous encouragement kept me motivated and will also do in the future. I would also like to express my sincere gratitude to my other committee members: Prof. Cagliyan Kurdak, Professor Nils Walter, Professor Zetian Mi, Professor Mackillo Kira, for their guidance and serving on my committee.

I would also like to thank my group members and collaborators who not only complement my work with their ideas and analysis but also kept an eye on the progress of my work and introduced me to novel research methods. My research would not have been possible

without their efforts and help. I would also like to thank the staff and my friends in Applied Physics program, Center for Photonic and Multiscale Nanomaterials (CPHOM), The Optical Society at the University of Michigan (OSUM), Department of Electrical Engineering and Computer Science (EECS), Lurie Nanofabrication Facility (LNF), the Electron Microbeam Analysis Laboratory (EMAL), the Solid State Electronics Laboratory (SSEL) for their support and insightful discussions.

Last, but most importantly, I would like to express my deep appreciation to my parents and family for their constant encouragement, unconditional love, and unfailing support. I am truly blessed to have them in my life.

# TABLE OF CONTENTS

# LIST OF FIGURES

# ABSTRACT

## Nanoengineered Functional Structures for Photonic and Microfluidic Applications

Owing to their extraordinary ability to interacting with external stimuli as well as their versatile functionalities hardly observed in bulk systems, micro- and nano-scale materials, structures, and phenomena have been the subject of increasing interest from both academia and industry. Many diverse fields including optoelectronics, photonics, bioengineering, and energy conversion have all shown significant increases in utilization of, and need for, micro/nano-scale features. To meet this demand, not only novel manufacturing methodologies, but also underlying physics and design principles are called for.

This thesis work addresses these issues while focusing on three main topics: (1) how certain fundamental nanostructures such as periodic nanopatterned surface, multilayers and charged particle-line can be utilized as functional building blocks for multidisciplinary applications ranging from nanoparticle/biomolecule manipulation to optoelectronics/photonics; (2) how these functional nanoarchitectures can be engineered in a continuous and scalable manner to increase the manufacturing throughput; and (3) the underlying physics and the design principles of these nanostructures in particular application systems.

More specifically, large area, 1D/2D periodic sinusoidal nanopatterned surface based on Dynamic Nano-inscribing (DNI) patterning technique is developed. And its applications to nanoparticle assembly/sorting and light extraction from GaN LED are investigated. By exploiting this sinusoidal nanovoid pattern and geometry-dependent ionic entropy, we successfully realized the size-selectively confinement and patterning of submicron-sized particles over a large area. Moreover, general method of light extraction from trapped modes by using these 1D/2D sinusoidal nanogratings have been developed. We applied our method to flip-chip GaN LED and a further enhancement of the total radiative power in addition to the PSS structures have been observed.

Metal/dielectric multilayer structures are widely used as fundamental building blocks for photonic crystal/metamaterials, color filters and anti-reflection coatings. Here in this work, we are focus on the applications of metal/dielectric multilayers on hyperbolic metamaterials (HMM) and surface-plasmon-coupled light emission from 2D materials and organic light emission materials. For hyperbolic metamaterials, we show that by using thin (~7nm) Al doped Ag metal films, we can dramatically improve the performance as well as the photon density of state (DOS) of the HMM. However, a further discussion on the nonlocal response of electrons in ultrathin (sub-1nm) metal films have been conducted and shows that the nonlocality induced by quantum effects of electrons (degeneracy pressure, diffusion kinetics and tunneling) can dramatically induce the transitions of the photonic topology of the metamaterials and intrinsically limit the DOS. Metal/dielectrics multilayers are also used to study the exciton-plasmon energy transfer and surface plasmon coupled

light emission from 2D semi-conductors ($WSe_2$) and organic light emission materials (Super Yellow). Based on one optimized planar multilayer structure we observed an 8 times enhancement of the PL signal. And we applied this concept to OLED structure, enhancement of the efficiency were also observed from SY-based OLEDs.

# Chapter 1

# Introduction

## 1.1 Background

In our daily life, lot of things naturally or artificially share similar fundamental structures in vary scales and areas, showing dramatically different functionalities. These fundamental structures, even those are very common in macroscale and in our daily life, could show fantastic novel properties and enable great applications when reproduce and implement smartly in nanoscale. Those nanoscale structures are of great interests due to their ability to sensitively interacting with external stimuli such as light, force, charges and chemical species, as well as their extraordinary properties (e.g. mechanical, electrical, optical, and chemical) which are hardly observed in bulk systems. These outstanding characteristics found in nanoscale structures have led to a significant amount of research effort for their utilizations to a variety of applications ranging from photonics to microfluidcs. Thus nanostructures, working as functional building blocks, are of great interest and not only novel fabrication technique but also the "smart" way of utilizing them are highly desired. This PhD thesis presents some of the recent developments of the above aspects.

Periodic nanoscale patterned surfaces are one of the most widely used nanostructures, due to their various functionalities and all kinds of established fabrication methods. However, the applications of nanopatterned surfaces are still far to be fully explored and making

desirable, large area nanopatterned surface on specific substrate in a low cost manner are still demanded. Here in this thesis, we introduce a kind of 1D/2D sinusoidal nanopattered surface by utilizing Dynamic Nano-inscribing (DNI) patterning technique. This technique enables large area pattering on flexible substrate in a very cheap manner. Based on a 2D DNI nanovoid pattern, we realized size-selective confinement, patterning and sorting of different size of sub-micron particles. Size-selective particle confinement, separation and sorting are highly desired in various applications such as diagnostics, chemical and biological analyses. But conventional methods such as pinched flow fractionation (PFF), lateral displacement sorting, dielectrophoresis (DEP), optical and acoustic manipulation usually require a continuous driving flow, complicated streamline and microfluidic channel design and usually work for particles with size in microns. Thus separation and sorting submicron-sized particles and biological objects with high throughput are still very challenging and demanding. The size-selective localization of particles in the void patterns are due to the interplay among the nanoparticle-pattern geometry, electrostatic interaction and ionic entropy change induced by charge regulation in the electrical double layer (EDL) overlap region. The principle can be generally applied to other particle-surface systems of different sizes and geometry, and this method could be extended to applications of biological objects directed assembly, separation and patterning.

Trapped modes of light are very general, which intrinsically limit the performance and applications of many photonic/plasmonic systems such as LED, OLED and photonic metamaterials (HMM). Here in this thesis, we experimentally demonstrate a mask-free,

low-cost and highly scalable method of light extraction from trapped modes by using 1D sinusoidal nanogratings fabricated by Dynamic Nanoinscribing patterning technique (DNI). We applied our method to flip-chip GaN LED and a further enhancement of 10% of the total radiative power in addition to the PSS structures have been observed. A general model describing the light-out coupling from trapped modes by using gratings are also developed in the language of photon population distribution and photon momentum transforming. Based on this model, we discovered the general efficiency enhancing conditions and the design principles to optimize the out-coupling efficiency by engineering both the nanoscale grating structures and the photonic density of states in the systems.

Planar metal/dielectric multilayer structures are one of the most important fundamental structures for nanophotonics and plasmonics with various applications like metamaterials, plasmonic waveguide, thin film color filter and multilayer optoelectronic devices. Here in this thesis, we demonstrated a high performance hyperbolic metamaterials based on metal/dielectric multilayers with home developed ultrathin (7nm), smooth, wetting layer free Al-doped Ag films. This hyperbolic metamaterial showed continuous optical response, great hyperbolic dispersion and much higher photonic density of states compared to conventional HMM made with thicker metal films. This ultrathin Al-doped Ag film also provide other potential applications such as transparent electrode and plasmonic waveguide. Moreover, motivated by the question of exploring ultrathin limit of HMM by using some atomic level thin metal films and 2D materials, an theoretic study on the nonlocal response of electrons in ultrathin (sub-1nm) metal films have been conducted and

shows that the nonlocality induced by quantum effects of electrons (degeneracy pressure, diffusion kinetics and tunneling) can dramatically induce the transitions of the photonic topology of the metamaterials and intrinsically limit the DOS. We demostrated that the mechanism is due to the reduced electron response and excited bulk plasmon induced by electron-electron interactions. These results also provide an alternatively explanation to the plasmonics behaviors of monolayer and multilayers graphene based materials.

Plasmonics enhanced light-matter interaction obtain great interest in optical and quantum communities due to its fundamental importance and various applications such as Raman detection, LED, photodetector, light modulators and so on. Metal/dielectrics multilayers are also used to study the exciton-plasmon energy transfer and surface plasmon coupled light emission from 2D semi-conductors (WSe2) and organic light emission materials (Super Yellow). Based on a 3 layers, deep sub-wavelength, dielectrics/metal/dielectrics structures, we observed a very sensitive separation distance dependent light emission enhancement phenomena. Based on one optimized planar multilayer structure we observed an 8 times enhancement of the PL signal. And we applied this concept to OLED structure, the distance dependent enhancement of light emission were also observed from SY-based OLEDs with both optical and electrical pumping. A decent analysis were conducted for the mechanism of these phenomena. We found the well-established conventional light-emitting theory cannot give a good explanation. A new model considering the FRED like non-radiative exciton-surface plasmon energy transfer have been suggested for the explanation.

## 1.2 Thesis outline

The thesis can be categorized into two parts: Periodic 1D/2D DNI nanopatterns and their applications for nanoparticle assembly/sorting and light-extraction from trapped modes; Metal/dielectrics multilayer structures and their applications for hyperbolic metamaterials and surface-plasmon-coupled light emission. These parts are closely correlated with each other.

**DNI nanopatterns and their applications for nanoparticle assembly/sorting and light-extraction**

**Chapter 2** presents a sinusoidal nanovoid surface enabled by Dynamic Nano-inscribing (DNI) patterning technique and its application for nanoparticle assembly/sorting. We introduce briefly this DNI fabrication technique. We demonstrates the size-selective confinement, pattering and sorting of sub-mirosized particles which are typically difficult in other particle sorting system. The mechanism is also demonstrated as geometry induced ionic entropy change and electric double layer overlapping.

**Chapter 3** presents the application of 1D DNI patterned nanograting in application of light extraction. For demonstration, we integrate this nanograting to flip-chip GaN LED and a further enhancement of 10% of the total output power in addition to the PSS structures

have been observed. A general model describing the light-out coupling from trapped modes by using gratings are also developed in the language of photon population distribution and photon momentum transforming. A mixed level simulation is also introduced.

**Metal/dielectrics multilayers and their applications for hyperbolic metamaterials and surface-plasmon-coupled light emission**

**Chapter 4** presents a high performance hyperbolic metamaterials (HMM) enabled by ultra-thin, smooth and low-loss Al-doped Ag film. We briefly introduce this Al-doped Ag film and the basics of HMM. HMMs consisting of thin constituent layers of Al-doped Ag films have both a low-loss and homogenous response. Also, they support a broader bandwidth of high-k modes as well as higher photonic density of states compared to HMMs made of thicker layers.

**Chapter 5** presents a theoretic study exploring the ultrathin limit of HMM based on ultrathin (sub-1nm) metal films or 2D materials. The nonlocal response of electrons are studied, showing that the nonlocality induced by quantum effects of electrons (degeneracy pressure, diffusion kinetics and tunneling) can dramatically induce the transitions of the photonic topology of the metamaterials and intrinsically limit the DOS. The mechanism is demonstrated as the reduced electron response and excited bulk plasmon induced by electron-electron interactions. These results also provide an alternatively explanation to the plasmonics behaviors of monolayer and multilayers graphene based materials.

**Chapter 6** presents a 3 layer, deep sub-wavelength DMD structures to study the exciton-plasmon energy transfer and surface plasmon coupled light emission from 2D semi-conductors (WSe2) and organic light emission materials (Super Yellow). A great enhancement of the PL signal has been observed from this 2D material-DMD structure and the enhancement shows very rapid distance dependence. Similar phenomena are presented in SY-based OLEDs with both optical and electrical pumping. The mechanism is discussed and a model considering the FRET like non-radiative exciton-surface plasmon energy transfer have been suggested for the explanation.

**Chapter 7** summaries the work in this thesis.

# Chapter 2

# Size-selective Confinement of Nanoparticles in Nanovoid Patterns by Exploiting Ionic Entropy

## 2.1 Introduction

Nanoparticles are of great interest in various research areas where their unique properties are exploited such as the strong interaction with light[1]–[3], their well-defined surface properties[4], [5], their high catalytic activity[6], [7] and in sufficiently small particles, their quantum confinement[8], [9] properties. In particular, if particles of a certain size can be placed in the array format many other applications can be exploited including photonic crystals[10]–[12], nanoelectronic devices[13]–[15], optical switches[16], [17] and filters[18], [19], filtration devices[20] and biological assays[21]–[23]. A prerequisite for these applications using particles ensembles as functional entities is the control and position selectivity of their arrangement on a surface. Doing so with standard microfabrication techniques is difficult, and it is often time-consuming and inefficient to create sparse patterns of small nanoparticles using subtractive top-down processing[24], [25]. Therefore a suitable particle patterning and assembly method with low cost and complexity are highly desired. Besides, size-selective particle confinement, separation and sorting are highly desired in various applications such as diagnostics, chemical and biological analyses, food and chemical processing and environmental assessment[26].

A number of methods have been reported for size-selective particle confinement, separation and sorting, including pinched flow fractionation (PFF)[27], lateral displacement sorting[28], hydrodynamic chromatography[29],electrophoretic deposition (EPD)[30], dielectrophoresis (DEP)[31], [32] and other active means utilizing magnetic, optical and acoustic manipulation techniques[26]. But most of these methods require a continuous driving flow, complicated streamline and microfluidic channel design and usually work for particles with size in microns. For submicron-sized particles, the intrinsic limitation of these methodologies make them not applicable. Thus separation and sorting submicron-sized particles and biological objects with high throughput are still very challenging.

In comparison, self-assembly emerge from particle-particle interactions enables the possibility of packaging particles over large scale. However, most self-assembly processes lack size-selectivity and the controllability of the particle arrangements as well as pattern features. However, directed assembly of particles utilizing particle-substrate interactions allow the greater control of the final particle positions as well as the selectivity. In contrast to conventional self-assembly, the geometry-induced electrostatic interaction[33] between charged particles and nanostructured substrate in ionic solution enable the directed assembly of particles, which does not merely fill predefined structures with randomly dispersed nanoparticles in solution, yet arranges nanoparticles at positions that are defined by the substrate's nanostructured geometry and surface charge.

Here in this work, based on a nanovoid substrate fabricated by 2D dynamic nano-inscribing (DNI) patterning technique[34], [35], we present a low-cost and highly scalable method of trapping and sorting nanoparticles in a size-selective manner governed by the geometric-induced electrostatic and entropic interaction between nanoparticles and the nanovoid surface patterns.

## 2.2 Methods and Materials

### 2.2.1 Experimental system

Colloidal particles assemble into arrays whose order depends closely on the relative dimensions of the spheres as well as the pattern geometry. In the methodology proposed here, discrete nanoparticles are arranged on nanostructured surfaces using directed self-assembly of particles which is governed by the geometry-induced electrostatic interaction between the particles and the substrate. This is accomplished by creating a nanostructured 2D sinusoidal void pattern on a polymer substrate using the Dynamic Nano-Inscribing (DNI) technique (as seen in Figure 2.1). A sputter-coated oxide layer provides this void pattern with a surface charge when exposed to an ionic solution containing charged nanoparticles of opposite charge polarity, which initiates the spatial confinement.

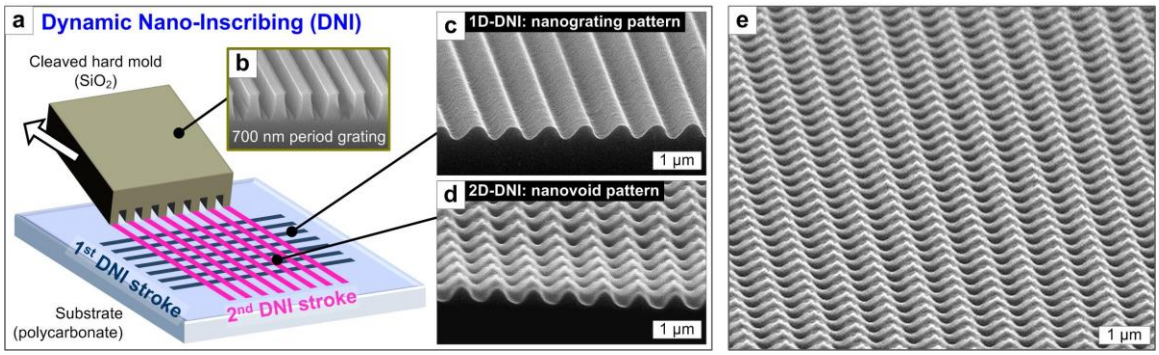


Figure 2.1: Dynamic nano-inscribing patterning technique. (a) Schematic illustration of dynamic nano-inscribing (DNI) process for single-stroke 1D nanopatterning or 2D nanopatterning by sequential combination. A well-cleaved edge of the 700 nm-period nanograting mold of SiO2 (b) contacts to and slides over a polymeric substrate under a conformal contact and localized heating, continuously creating 1D grating (c) and 2D nanovoid patterns (d) having well-defined sinusoidal surface profiles. (e) Perspective view of 2D-DNI-fabricated nanovoid arrays.

Our process is based on generating a sinusoidal electrostatic potential on the 2D-DNI-patterned substrate that has the ability to couple with oppositely charged nanoparticles in an ionic solution ($10^{-3}$[M]). Most macromolecules as well as many oxide surfaces develop a net electric charge (by either the dissociation of chemical groups or the adsorption of ions from solution) when suspended in an ionic solution. The charged NPs undergoing Brownian motion in solution experience an electrostatic attraction in the vicinity of the oppositely charged surface. Our experimental device (Figure 2.2a) consists of a microfluidic cell chamber consisting of two transparent cover slips. One of these cover slips contains the 700 nm-pitched nanovoid array fabricated by 2D-DNI, coated with 10 nm thick $Al_2O_3$ oxide layer which is positively charged when immersed in an ionic solution. The other acts as a transparent medium for top-down microscopic characterization. As the suspension of negatively charged polystyrene NPs ($-1.8$ e/nm$^{-2}$ -

−56 ± 13 mV) flows into the fluidic cell, their size and surface charge density control the trapping behavior. We can directly visualize the instantaneous confinement and assembly of fluorescently labelled 500 nm diameter polystyrene particles in the patterned voids. The 2D sinusoidal potential profile accentuates the trapping process, enabling the size specificity of this confinement methodology. A schematic, shown in Figure 2.2a, depicts the experimental setup.

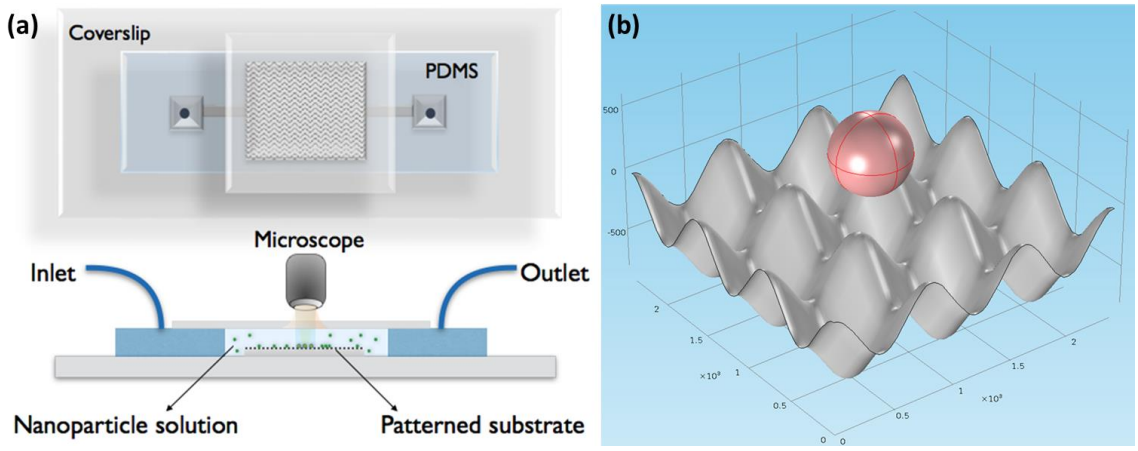


Figure 2.2: Experimental and simulation systems. (a) Experimental fluidic cell chamber schematic. (b) Simulation characteristics as the particle descends into the nanovoid in the z-direction.

## 2.2.2 Nanostructured substrate preparation

Commercially available flexible substrates films like phenol formaldehyde resins (PF), polycarbonate (PC) and polyethylene terephthalate (PET) were pre-cleaned before patterning. Details of DNI processes along with mold preparation and cleaving procedure can be found elsewhere[34], [35]. All polymer substrates (PET and PC from Tekra Corp.) were used as purchased and cleaned using IPA followed by nitrogen drying before the

patterning process. To Perform DNI, we prepare a well-cleaved $SiO_2$ nanograting mold containing the desired pattern along the edge; then bring the mold edge in contact with the substrate at a proper angle and force, and then slide the mold edge over the substrate while maintaining a conformal contact. The polymer surface is plastically deformed by the nano-features on the mold edge, leaving behind a well-defined nanograting pattern. This process is subsequently repeated in the orthogonal direction, which produces the sinusoidal void pattern as shown in Figure 1. In DNI, the pattern period is dictated by that of the grating mold and voids of various sizes and geometry can be inscribed in a continuous manner at high speed (~ 1 m/min or greater). For instance, we used a $SiO_2$ grating mold with 700 nm-period for 2D nanovoid patterning in this work (unless otherwise noted in our data). Therefore the void patterns can be precisely inscribed to a certain size, depending on the size of the particle to be selectly trapped. Furthermore, the morphologies of the sinusoidal voids created by 2D-DNI can be specifically tailored by changing the substrate material, applied force, and processing temperature.

### 2.2.3 Microfluidic cell preparation

For the NP confinement cell fabrication, a 2D-DNI-patterned PC substrate was coated with a 10 nm-thick $Al_2O_3$ layer by RF sputtering (Lab 18-2, Kurt J. Lesker) and was put in the microfluidic cell chamber held at a separation of 1 mm by PDMS spacers between two transparent cover slips. Fluorescent labelled (FITC-525nm) polystyrene nanoparticles were purchased from Molecular Probes Ltd. and centrifuged and re-aliquoted into solutions with

varying ionic concentrations. This nanoparticle suspension at an initial volume fraction of 0.1 % wt was injected into the chamber at a fixed flow rate (10 µl/min). The ionic solution containing NPs was allowed to equilibrate inside the chamber for 15 minutes before microscopic observation.

### 2.2.4 Microscopic Characterization

Electron Microscopy was performed using a Philips XL30-FEG at the typical operating voltage of 5-25 kV. Solution conductivity and nanoparticle measurements were quantified using commercial DLS light scattering instrumentation (Zetasizer Nano, Malvern Instruments). For Fluorescence microscopy, we used an Olympus BX-100 to gather frames at various time intervals. Exposure times of 10ms, 30ms and 100ms were used to visualize the movement of particles in solution. As the particles were coated with FITC dye molecules, a 485 nm excitation light source was used to illuminate the sample. The experimental microscopy setup is shown in the Figure below.

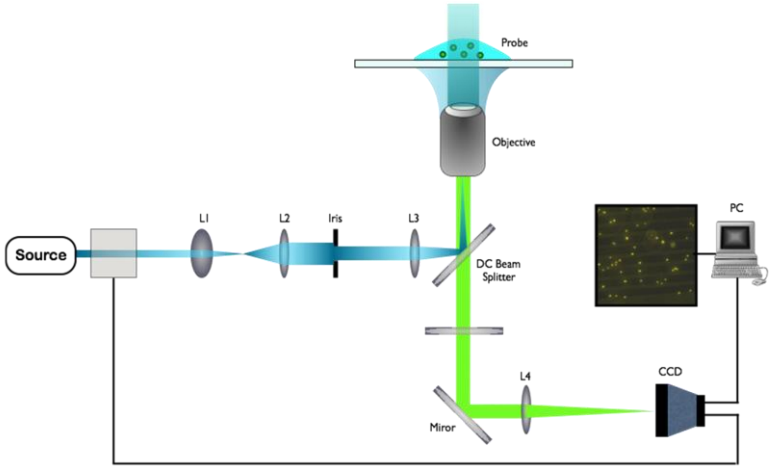


Figure 2.3: Fluorescence microscopy setup for in-situ visualization.

### 2.2.5 Surface charge characterization

Solution conductivity and nanoparticle measurements were quantified using commercial DLS light scattering instrumentation (Zetasizer Nano, Malvern Instruments). The value of the zeta potential for the slit surfaces was estimated from electro-osmotic flow measurements in fluidic slits. For the oxide coated void patterns, the electrostatic potential distribution was theoretically estimated by solving the Poisson-Boltzmann equation using constant-charge boundary conditions and verifying overall electroneutrality of the system. Experimental surface charge density deviated from theoretical results due to three dimensional structuring of the surface. Metallic oxides form surface charges in the presence of ionic solution through dissolution and subsequent adsorption of hydroxyl ions in solution. Alumina surfaces immersed in an ionic solution acquire a positive surface charge density primarily through the dissociation of terminal -OH groups (see below). The degree of dissociation and thus the surface charge density results from an equilibrium between counter ions at the surface and free ions in the bulk electrolyte:

$$\text{Al-OH} + \text{H}^+ \longrightarrow \text{Al}^+\text{OH}_2 \qquad \text{pH} < 7.0$$

$$\text{Al-OH} \longrightarrow \text{AlO}^- + \text{H}^+ \qquad \text{pH} < 8.2$$

$$\text{Al-OH} + \text{OH}^- \longrightarrow \text{AlO}^-\text{OH}_2 \qquad \text{pH} > 8.2$$

This behavior and the polarity is highly dependent on the pH of the interacting solution. Electroosmotic flow experiments were performed to quantify and estimate the surface charge density of our void pattern. As seen in Figure 2.4, for a sputter coated $Al_2O_3$ film the surface charge density is positive at neutral pH and can be tuned by changing the pH of the solution.

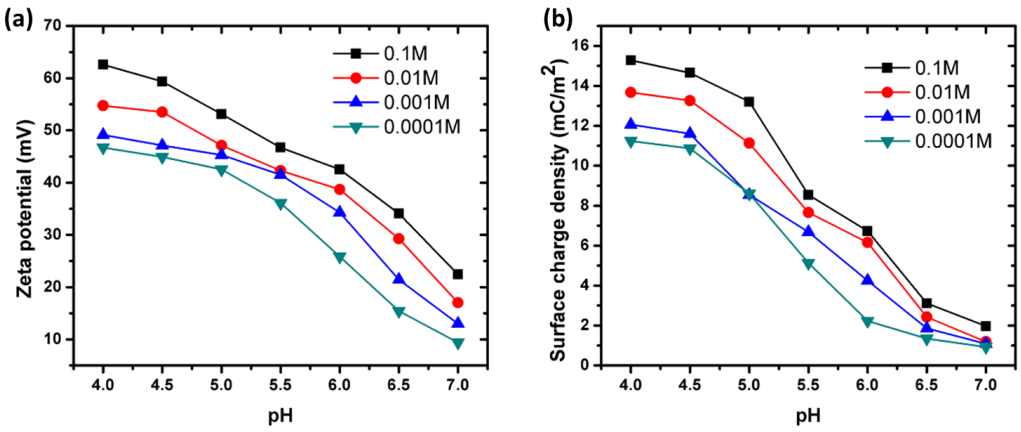


Figure 2.4: Zeta potential (a) and electroosmotic surface charge density (b) estimations at various pH and ionic concentrations.

The charging behavior and capacity of Al2O3 films in solution have been extensively studied in the past and it should be noted that the surface charge density of Al2O3 films degrade overtime in ambient conditions caused by the above mentioned reactions. Conformity of the coating was confirmed using an SEM. The deduced surface charge densities are in relatively good agreement with other research groups that experimented with similar volumetric structures3. Furthermore, various other oxides like CaO, NiO and MgO can also be used to vary the polarity and degree of charging at the desired operating pH.

## 2.3 Directed nanoparticle assembly

Figure 2.5 shows the microscope images of 500nm PS nanoparticles trapped on the substrates with different surface conditions. In the absence of the nanovoid pattern on the substrate, only very few amount of particles are randomly adsorbed on the surface, even in the case when surface charges are presented by the $Al_2O_3$ layer. In contrast, in the presence

of the patterned surface with the oxide layer, much larger amount of particles are trapped onto the substrate. Moreover, as seen in the zoom-in image (and verified by SEM image) in Figure 2.5C, almost all trapped particles are well confined inside the nanovoids, i.e. they assemble into the pre-defined pattern on the substrate. The trapping is stable, even without any direct chemical linkage. The confined particles adhere to the surface strongly and cannot be removed by rinsing the channel with DI water. Only by using stronger physical force e.g. placing the substrate in an ultrasonic bath, most of the particles can be dislodged from the surface.

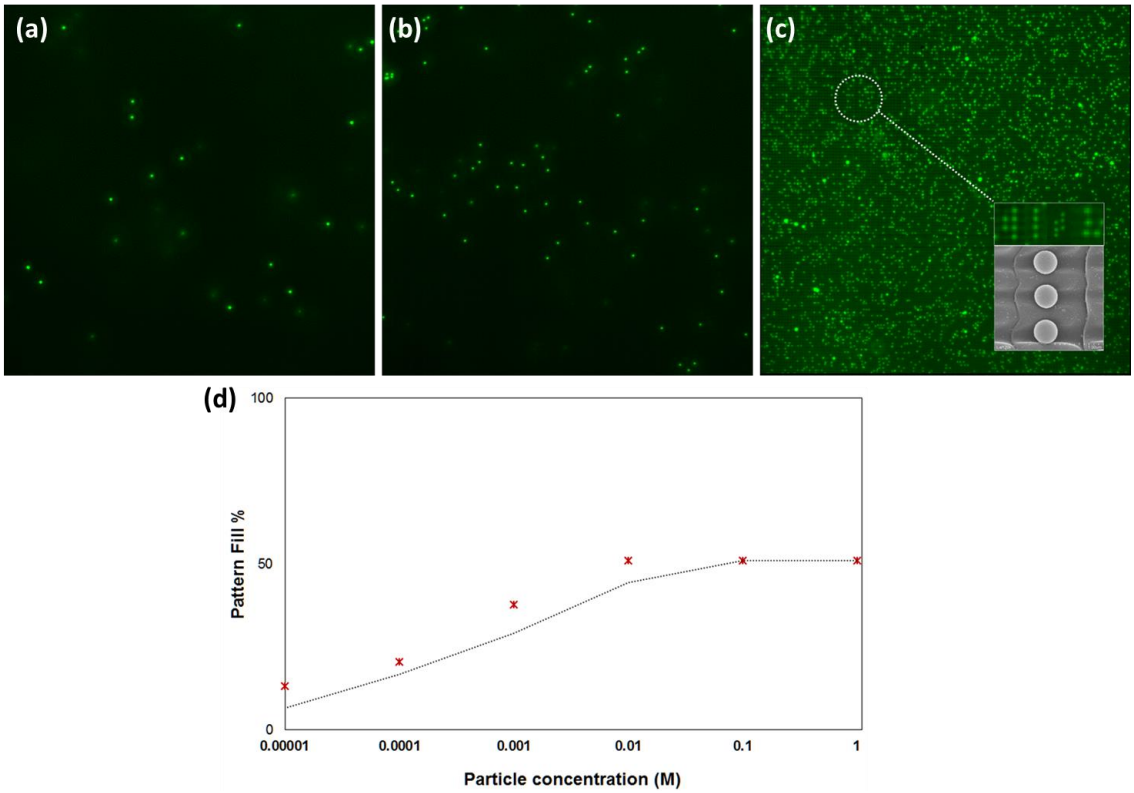


Figure 2.5: Particle directed assembly. Epi-fluorescent micrograph of 500nm diameter particles on (a) Un-patterned, uncoated polycarbonate substrate. (b) Un-patterned, 10nm $Al_2O_3$ coated polycarbonate substrate. (c) Patterned substrate coated with 10nm $Al_2O_3$. The insert charts show the zoon-in microscopy and SEM images of the trapped particles. (d) Nanovoids fill ratio as the function of the particle concentration. The diameter of the particles is 500nm.

In order to improve the trapping efficiency and particle pattern quality, we studied how the particle concentration affect the void pattern fill ratio. As this process is diffusion limited and no external stimuli is applied, increasing the particle concentration increases the fill ratio to a certain degree and further increasing the particle concentration beyond 0.01M did not appreciably increase the fill ratio as shown in Figure 2.5d. The fill ratio is saturated around 50% and this can be possibly explained due to the electrostatic repulsion from the particles already confined on the surface. Thus by increasing the spacing between the nanovoid or increasing the attractive particle-substrate interaction such as by increasing the nanovoid surface charge density, the fill ratio can be enhanced as well as the pattern quality.

## 2.4 Size-selectivity

While the 500nm size particles trapped in a similarly sized void could be expected, but an equally interesting occurrence would be whether a nanoparticle with other sizes could also be trapped in these voids. Therefore we performed experiment with a fixed void size and tested three different particle sizes (200nm, 500nm, 1000nm) to evaluate the trapping behavior. Under similar conditions and at the same mentioned flow rate we found that only particles of 500nm diameter were confined in the voids (Figure 2.6b and e). In the case of 200nm particles some non-specific adsorption was observed but no appreciable confinement in the voids (Figure 2.6a and d). Similar results were obtained when testing 1μm particles (Figure 2.6c and f).

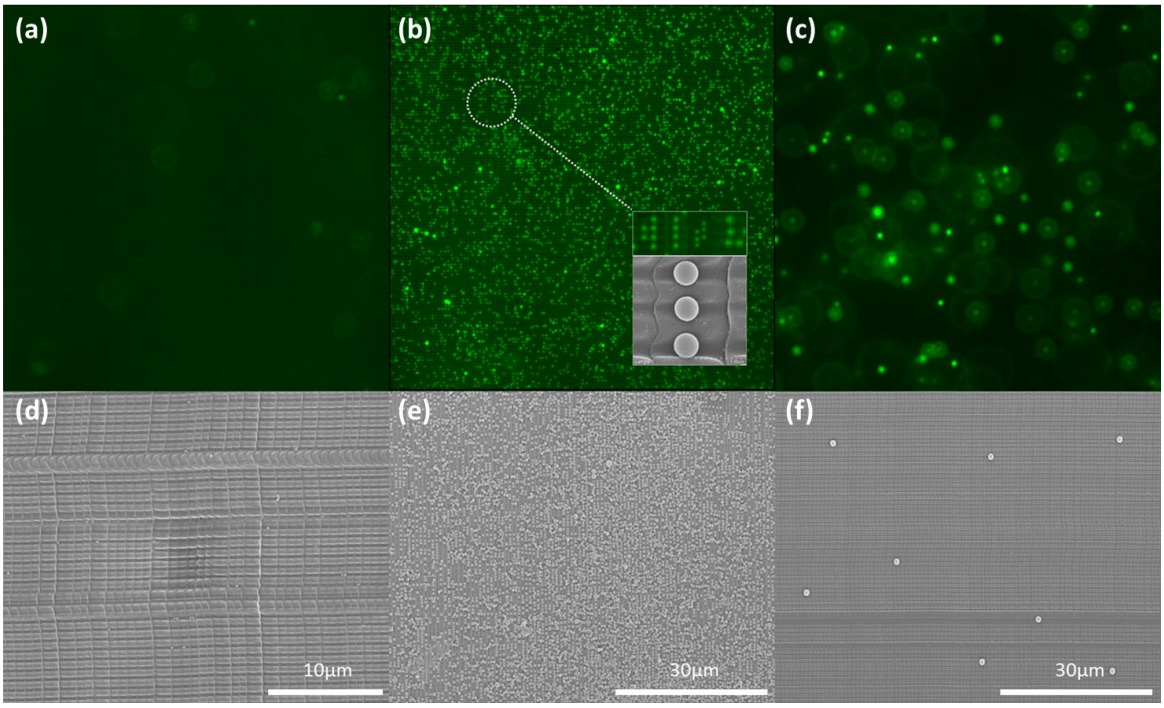


Figure 2.6: Size-selected trapping. Microscope and SEM images of the nanoparticles trapped to the patterned structure for 200nm particles (a and d), 500nm particles (b and e) and 1µm particles (c and f). The inset picture in (b) shows the zoom in view of the trapped particles.

## 2.5 Mechanism of size-selective nanoparticle confinement

These results indicate the size-selective nature of this method and provide the possibility for submicron-sized particle separation and sorting based on their size and surface charges. To understand this size-selective behavior, we modeled this system and simulated the interaction between the charged particles and the charged void surface using finite element analysis (FEA) method in COMSOL Multiphysics. We calculated the free energies for this system based on mean field Poisson-Boltzmann (PB) theory[36] and analyzed in detail the

electrostatic and entropic contributions as a function of particle position above the patterned structure.

The electrostatic potential contributed by both surface charges and ions can be calculated by the dimensionless PB equation,

$$\nabla^2\psi = \kappa^2 \sinh(\psi) \tag{2. 1}$$

where $\psi = \frac{e\varphi}{k_B T}$ is the dimensionless electrostatic potential, $\kappa = \sqrt{\frac{2c_0 e^2}{\varepsilon\varepsilon_0 k_B T}}$ and $\kappa^{-1}$ defines the "Debye length" of the electrical double layers (EDLs).

We assume fixed surface charge at both particle surface and the surface of the void structures. The boundary conditions for the potential are defined by the surface charge densities:

$$\boldsymbol{n}\bullet\nabla\psi = -\frac{\sigma}{\varepsilon\varepsilon_0 k_B T} \tag{2. 2}$$

These equations were numerically solved using COMSOL Multiphysics, and next we calculated the free energy of the system by taking into account both the energetic and entropic contributions as a function of particle position above the patterned structure. The free energy of a charge distribution may be analyzed in terms of its electrostatic potential energy and the configurational entropy of the ions and solvent in the electrolyte. The electrostatic energy of the system is given by [36]:

$$U_{es} = \frac{\varepsilon\varepsilon_0}{2}\int_V (\boldsymbol{E}\bullet\boldsymbol{E})dV \tag{2. 3}$$

The entropy change of the system is given by (details see Section 2.8):

$$\Delta S = k_B \int_V \left\{ \sum_i c_0 \left[ z_i\psi \exp(-z_i\psi) + \exp(-z_i\psi) - 1 \right] \right\} dV \tag{2. 4}$$

The integration volumes in both equations are the whole simulation system comprising the charged particle, ions and the surface of the nanovoids. The system's free energy is then obtained:

$$F = U_{es} - T\Delta S \tag{2. 5}$$

So for our system, we can write the free energy as:

$$F = \int_V \left\{ \frac{\varepsilon\varepsilon_0}{2} (\boldsymbol{E} \bullet \boldsymbol{E}) - 2c_0 k_B T (-\psi \sinh\psi + \cosh\psi - 1) \right\} dV \tag{2. 6}$$

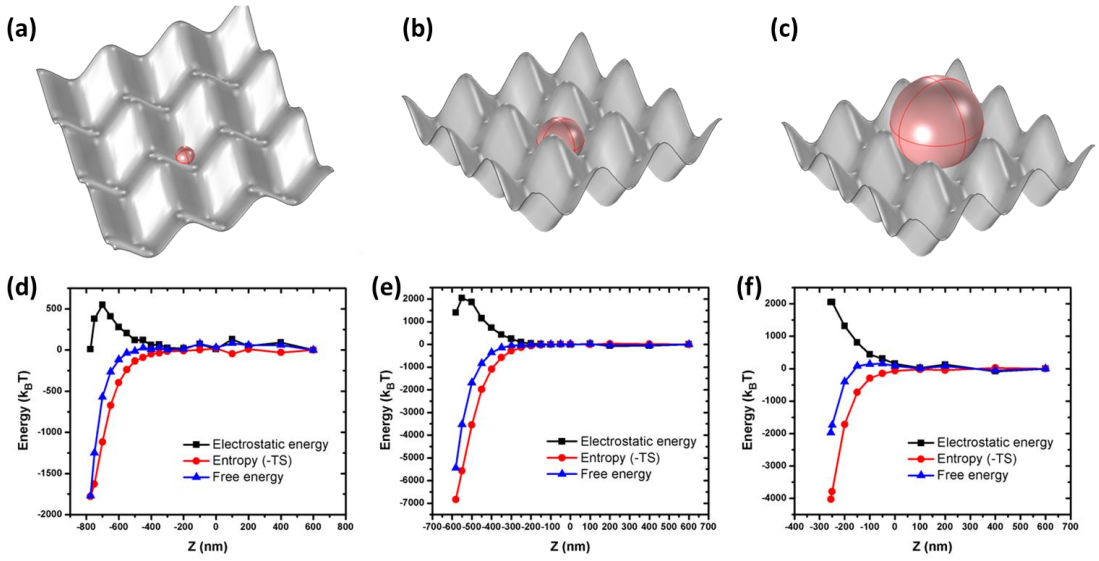


Figure 2.7: Energy profiles of the traps. (a, b, c) Geometry of the particles at the lowest positions in the voids for 200nm, 500nm and 1μm particles respectively. (d, e, f) Calculated energy change of the system, when particles are approaching the bottom of the void in z-direction for 200nm, 500nm and 1μm particles respectively.

Figure 2.7 shows the calculated energy change of the system, when particles with different size approach the bottom of the void in z-direction. Though from a purely electrostatic energy standpoint, there exists a counterintuitive energetic barrier preventing the particles reaching the bottom of the voids, which is due to the high E field as well as the stored

electrostatic energy between the particle and the substrate surface when they get close that depletes the initial screening ions in the EDLs, the free energy of the system that governs the final net force and potential experienced by the particles shows a clearly attractive interaction between the particles and the voids. The appearance of electrostatic energy barrier can be better understood by considering two parallel charged surface, which can be found in Section 2.6.1. The free energy of the two surfaces follow exactly the same behavior as the particle-void system. The attractive interaction governed by the free energy of the system makes the void behave like a trap and clearly for the 500nm particle, this trap has the deepest potential well and strongest confinement as compared to that for the 200nm and 1μm diameter particles. These results perfectly explained that the size-selectivity observed in the experiment is due to the free energy potential well for particles with size that appropriately fits the void.

It is instructive to examine the different roles of electrostatic and entropic contributions to the trapping process. The electrostatic interaction is responsible for attracting the particles toward the void surface, but when the surfaces of the particle and the void get close, the EDLs of the two oppositely charged surfaces overlap, the surrounding cations and anions are depleted in the EDL overlapping region, which weakens the screening of surface charges and thus increases the stored electrostatic energy between these two surfaces. However as the particle approaches the nanovoid surface, some ions from the overlapped EDL region are displaced to the free space above, thus increasing the entropy of the system and leading to strong confinement force. In our cases, the entropic energy contributes much

more to the final potential well and dominated the size-selective confinement as is shown in Figure 2.7. And a better geometric fit of the particle and the void will displace larger amount of ions as the gap between the two surfaces closes in, and therefore causes higher increase in entropy, which leads to deeper free energy well. Similar ion depletion process and the appearance of electrostatic energy barrier as well as free energy wells can also be observed in a simpler system of two oppositely charged parallel surfaces. Detailed discussions can be found in Section 2.6.1.

To verify this explanation, we calculate the depth of the free energy potential well experienced by the particles when they are at the lowest positions in the voids for particles of different sizes from 100nm to 1 μm, and we also calculate the areas of overlapping EDLs between the particles and the structures. As is shown in Figure 2.8, the depth of the potential well shows direct correlation with the EDLs overlapping areas and both of these two plots expect that the nanovoid structure with current geometry works best for the 500nm size particles. These numerical results support our explanations: the "best fit" particles have the largest overlapping areas with the nanovoid structures, which release most amount of ions and cause the largest entropy change. As a result, much deeper and sharper energy traps form for the particles of particular size. Since the nanovoid geometry is fixed in our experiment, only particles of particular size can be confined, leading to the observed size-selective confinement and separation of particles. Based on this explanation, the nanovoid pattern design can be optimized in order to better confine and extract desired particles with particular size and geometry, all in a single step process. A more detailed

discussion about the geometry of the nanovoids are conducted in Section 2.6.2. There we compare our DNI sinusoidal nanovoid structure with a better designed hemispherical nanovoid structure, which show a deeper free energy well for the desired particles and a much higher particle size selectivity. Thus a high resolution selective confinement and separation can be achieved with a well-designed geometry of the void structure.

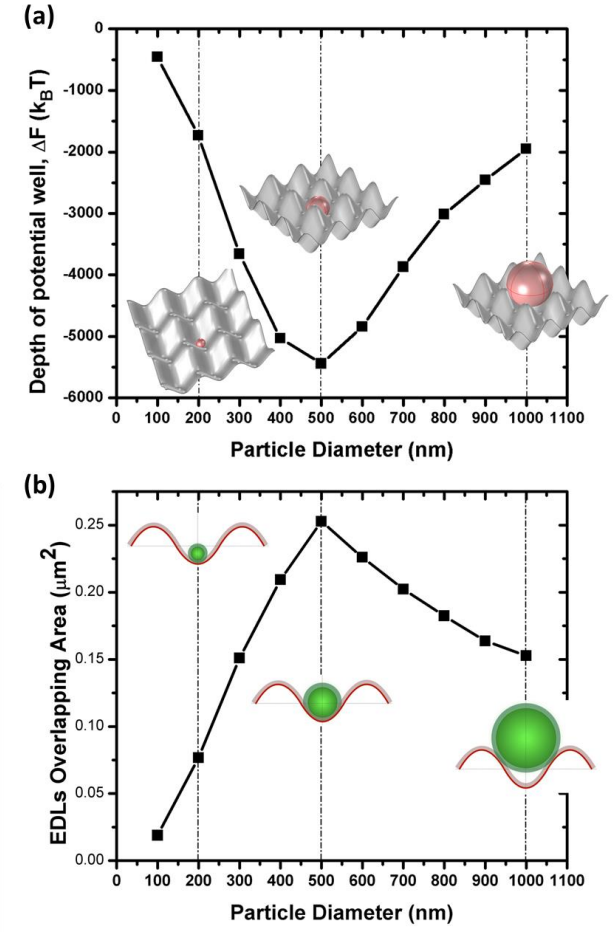


Figure 2.8: Explanation of the size-selectivity. (a) Depth of the free energy potential well for particles in the voids with different sizes. The insets show the geometry of the nanovoids and particles at the lowest positions in the voids. (b) EDLs overlapping areas for particles in the voids with different sizes. The insets show the schematics of EDLs overlapping when particles are located at the lowest positions in the voids for 200nm, 500nm and 1μm particles. Only particles with particular size fit the void geometry well can obtain largest EDLs overlapping areas.

## 2.6 Discussions

### 2.6.1 Electrical double layers (EDLs) overlapping process

In order to explain the energy profiles and associated trapping process in our simulations, we conduct an analytical study on the overlapping process of the EDLs of two oppositely charged planar surfaces. The details of the methods can be found in Section 6 of this Supporting Information. Here we consider two charged planar surfaces with surface charge density of +2.03mC/m$^2$ and -1.6mC/m$^2$ immersed in the KCl solution with the ionic concentration of $10^{-4}$M as the same condition in our experiment.

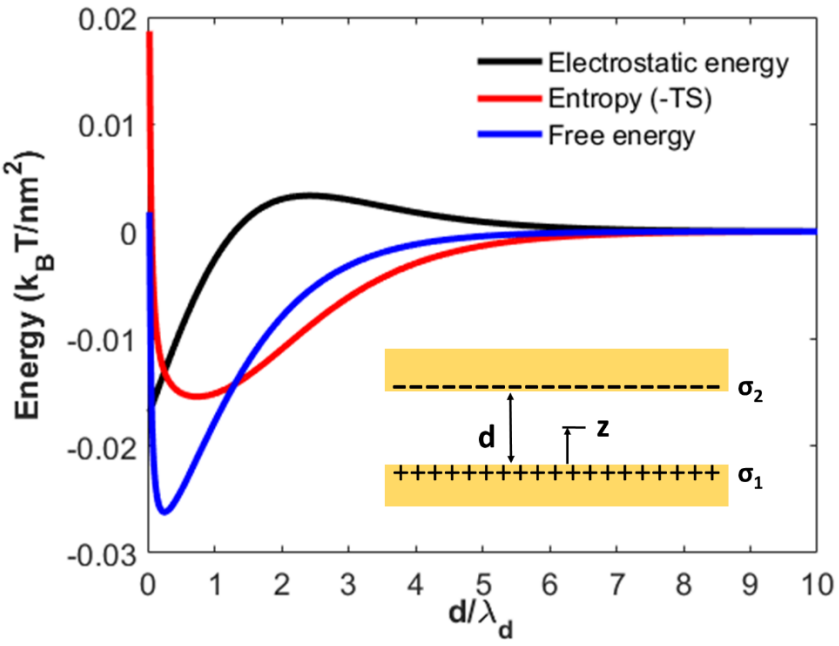


Figure 2.9: Interaction energy of two charged planar surfaces. The surface charge density and ionic concentration are the same as we used in our experiments. A potential barrier has been observed from pure electrostatic energy around 2.5 Debye length.

Figure 2.9 shows the calculated interaction energy profiles for the charged surfaces with different separation distance (d). As we can see here, a potential barrier is also obtained from the electrostatic energy profile around 2.5 Debye length when the two surfaces are getting close, which indicates the electrostatic potential barrier we observed in our particle-nanovoide system is not unique of that system but the intrinsic nature of the overlapping EDLs.

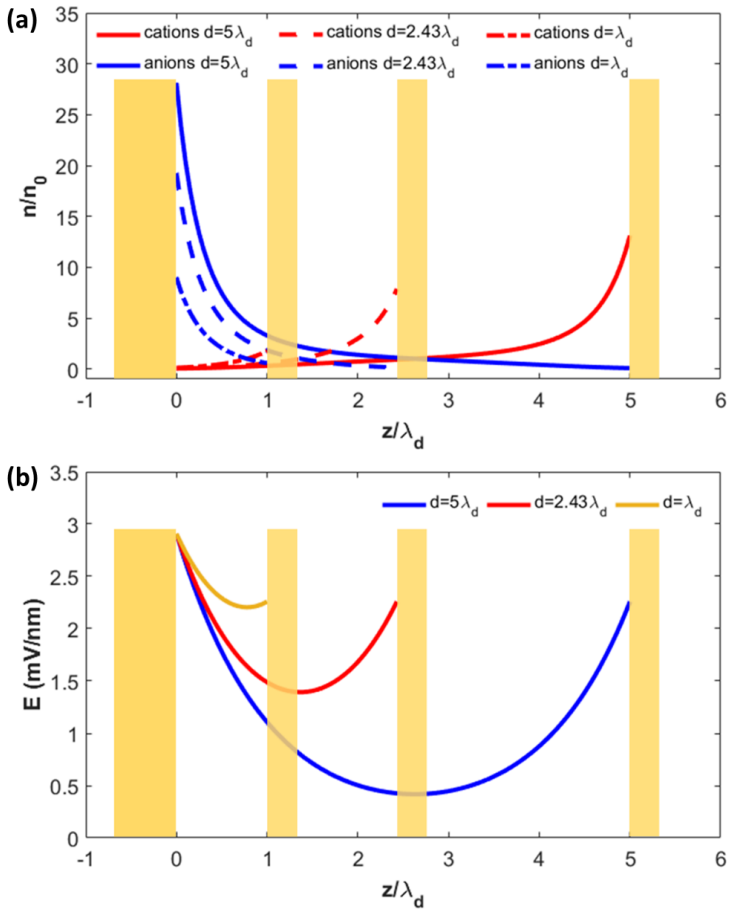


Figure 2.10: Ions distribution (a) and E field distribution (b) between the two charged surfaces with different separation distance. When the two surfaces get closer, both cations and anions initially confined in the EDLs are released, leading to a high average E field between the two surfaces.

Moreover, if we plot the distribution of the screening ions and the E field between these two surfaces (Figure 2.10), it's very clear that both the concentrations of the cations and anions decrease rapidly when the two surfaces are getting closer, which weakens the screening of the surface charges and leads to higher E fields (Figure 2.10b) as well as stored electrostatic energy between the two surfaces. But as we know, the in stored electrostatic energy is an integral across the volume between the surfaces, so the electrostatic energy profile finally drops due to the decrease of the volume when the surfaces get very close to each other. Thus, it's not difficult to understand why we observed electrostatic potential barrier for both particle-nanovoids system and the two planar surfaces. Furthermore, the depletion of the ions in the EDLs overlapping region shown in Figure 2.10a support perfectly about our explanation of the entropy change: ions initially confined in the EDLs are released into the solution, resulting in the increase of the entropy as well as the decrease of the free energy of the ionic system.

### 2.6.2 Effect of geometry: hemispherical vs sinusoidal nanovoids

As we explained in the main context, the size-selective confinement is due to the geometrical match of the particle and the nanovoid structure. Thus we conduct a further study focusing on the influence of the geometry by comparing the DNI sinusoidal nanovoid structure with a hemispherical nanovoid array (void diameter 500nm, period 700nm) as shown in the insert pictures of Figure 2.11a. As we can see in Figure 2.11, both the potential well calculation and the EDLs overlapping areas calculation indicate that the hemispherical nanovoid structure works as a better size-selective trap for 500nm particles with much

deeper potential well out-standing from the other sized particles compare to the DNI nanovoid structure. These results support perfectly of our explanation of the size-selective confinement by using the model of geometry matching and EDLs overlapping. Moreover, these results also indicate the possibility of more controllable and more precisely sorting of desired nanoparticles or bio-objects with method by using particularly designed nanovoid patterns.

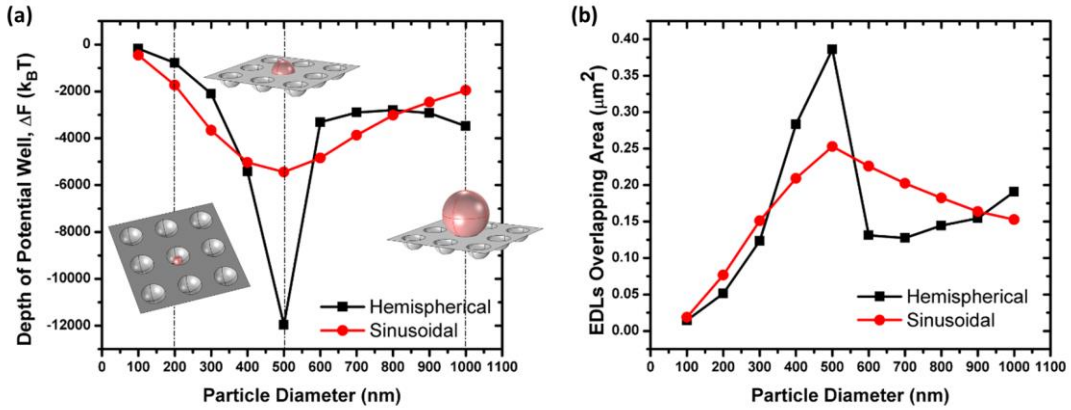


Figure 2.11: Hemispherical nanovoid structure vs. DNI sinusoidal nanovoid structure. (a)Depth of the potential well, (b) EDLs overlapping areas for particles in the voids with different sizes. With better geometry match, a better selectivity can be achieved. The insert pictures in (A) show the geometry of the hemispherical nanovoids and particles at the lowest positions in the voids.

## 2.6.3 Influence of the ionic concentration and ion type

The influence of the ionic concentration and ion type are also studied. Here in Figure 2.11a shows the depth of potential well with different ionic concentration. As we can see from the figure, for high concentration ($10^{-3}$M) case, because the Debye length is very short in this case, a considerable interaction only happens when the geometric matching is very

good as it requires sufficient EDLs overlapping area in much closed separation. Thus for our case, almost particles of all size cannot be confined in the void. While for the case of low concentration ($10^{-5}$M), though shows selectivity, but the strong trapping forces will confine almost all sizes of the particles in our case. Thus choosing an appropriate ionic concentration is also very critical for the size-selective trapping.

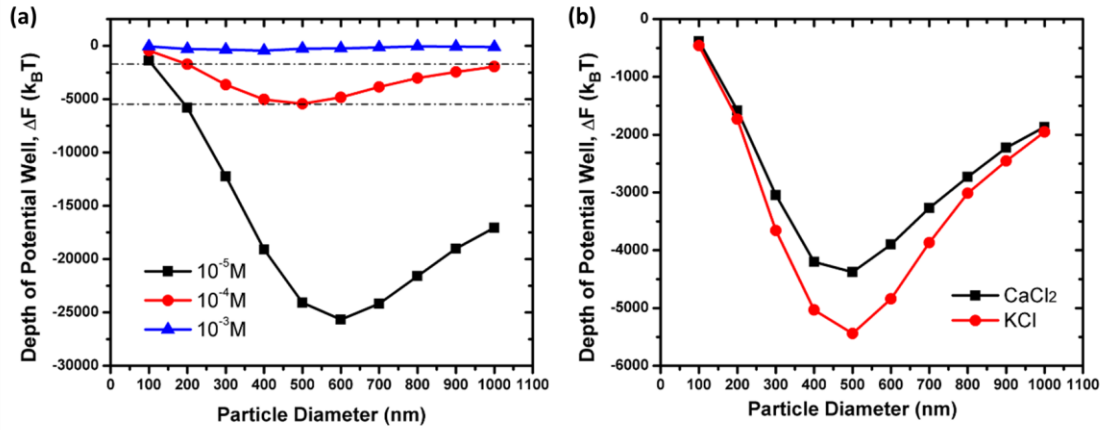


Figure 2.12: Depth of the potential well for (a) different ionic concentration (b) different ion type CaCl2 vs KCl. In (b), the concentration of anions for both CaCl2 and KCl are kept the same as $10^{-4}$M.

Besides, the type of the electrolyte also have influence on the process. Figure 2.12b compares the depth of the potential well for $CaCl_2$ and KCl solutions with keeping the anions concentration (or equally keeping the charge density) the same as for both cases. As is shown in figure, monovalent electrolyte like KCl works better than $CaCl_2$ as providing a deeper well as well as higher selectivity. The reason for that can be attribute to the slightly longer Debye length of KCl (30nm vs. 25nm) and more cations participating in the process, which can contribute to much larger entropy change when filling in the same charge requirement.

## 2.7 Conclusions

Based on DNI patterning technique and directed self-assembly of nanoparticles controlled by the geometric-induced electrostatic and entropic interactions, we experimentally demonstrate a single-step, low-cost methodology to selectively confine, pattern and sort nanoparticles based upon their size on a flexible substrate with nanovoid patterns over a large area. This size-selective confinement is due to the free energy change of the system which arises from EDLs overlapping, ionic redistribution and the associated entropy change. The patterning methodology used here can enable continuous and high speed production of 2D nano-patterns on flexible substrates. Application of this selective nanoparticle confinement method could potentially be extended to scalable localization, sorting and manipulation of charged biological objects such as proteins, lipid vesicles, cancer cells and bacteria.

## 2.8 Theory basics

### 2.8.1 Poisson-Boltzmann (PB) equations calculation in multivalent electrolyte solution

Here we consider the PB equation in a general multivalent electrolyte solution ($AB_m$) with cations of $A^{m+}$ and anions of $B^-$. Thus the electrostatic Poisson equation can be written as:

$$\nabla^2\varphi = -\frac{\rho}{\varepsilon\varepsilon_0} \tag{2. 7}$$

Here $\varphi$ is the electrostatic potential, $\varepsilon$ is the relative dielectric constant of the solvent and $\rho = \sum_i ez_i n_i$ , is the net charge density which determined by the concentration ($n_i$) and valence ($z_i$) of each kind of ions.

By considering the Boltzmann distribution of the ions $n_i = n_{i0} \exp\left( -\frac{ez_i\varphi}{k_B T} \right)$ and defining dimensionless electrostatic potential $\psi = \frac{e\varphi}{k_B T}$ , the Poisson equation can be written as:

$$\nabla^2 \psi = -\frac{e^2}{\varepsilon\varepsilon_0 k_B T} \sum_i z_i n_{i0} \exp\left(-z_i \psi\right) \tag{2. 8}$$

Define the screening strength $\kappa^2 = \frac{e^2}{\varepsilon\varepsilon_0 k_B T} \sum_i z_i^2 n_{i0}$ , thus:

$$\nabla^2 \psi = \kappa^2 \frac{\sum_i z_i n_{i0} \exp\left(-z_i \psi\right)}{-\sum_i z_i^2 n_{i0}} \tag{2. 9}$$

For the case of ABm, $n_0^- = m n_0^+$ or $n_0^+ = n_0^- / m$ , thus:

$$\kappa^2 = \frac{e^2 n_0^- \left(m+1\right)}{\varepsilon\varepsilon_0 k_B T} \tag{2. 10}$$

And the Poisson equation comes to be:

$$\nabla^2 \psi = \kappa^2 \frac{e^{\psi} - e^{-m\psi}}{1+m} \tag{2. 11}$$

Once we solve the PB equation in the system and define the dimensionless potential $\psi$ , then we can define the total electrostatic energy of the system:

$$U_{es} = \frac{\varepsilon\varepsilon_0}{2}\iiint (\boldsymbol{E}\bullet\boldsymbol{E})\,dV \tag{2. 12}$$

Here $\boldsymbol{E} = -\nabla\varphi = -\frac{e}{k_B T}\nabla\psi$ is the electrostatic field. And the entropy can be defined as[36], [37]:

$$\Delta S = -k_B \iiint \sum_i \left[ n_i \ln\left(\frac{n_i}{n_{i0}}\right) - n_i + n_{i0} \right] dV \tag{2. 13}$$

Thus for ABm:

$$\Delta S = k_B \iiint n_0^- \left[ -\psi\left(e^{\psi} - e^{-m\psi}\right) + \left(e^{\psi} + \frac{1}{m}e^{-m\psi}\right) - \left(1 + \frac{1}{m}\right) \right] dV \tag{2. 14}$$

And the free energy:

$$F = U_{es} - T\Delta S \tag{2. 15}$$

Practically for monovalent electrolyte AB, $n_0^+ = n_0^- = n_0$:

$$\nabla^2\psi = \kappa^2 \sinh(\psi) \tag{2. 16}$$

$$\Delta S = k_B \iiint \left\{ \sum_i n_0 \left[ z_i\psi \exp(-z_i\psi) + \exp(-z_i\psi) - 1 \right] \right\} dV \tag{2. 17}$$

$$\Delta S = 2k_B n_0 \iiint \left[ -\psi \sinh(\psi) + \cosh(\psi) - 1 \right] dV \tag{2. 18}$$

$$F = \iiint \left\{ \frac{\varepsilon\varepsilon_0}{2}(\boldsymbol{E}\bullet\boldsymbol{E}) - 2n_0 k_B T\left(-\psi\sinh\psi + \cosh\psi - 1\right) \right\} dV \tag{2. 19}$$

### 2.8.2 Poisson-Boltzmann (PB) equations calculation for two charged planar surfaces

Here we consider two charged planar surfaces as established in Section 2 of this Supporting Information. And to simplify this problem, we calculate the interaction energy only for monovalent electrolyte and in the linear approximation region, which should give qualitatively accurate description of the system[37].

The linear PB equation can be write as[37], [38]:

$$\nabla^2\varphi = \kappa^2\varphi \tag{2. 20}$$

With surface charge boundary conditions: $(\nabla\varphi)\bullet\vec{n} = \frac{\sigma}{\varepsilon\varepsilon_0}$. And here $\kappa = \sqrt{\frac{2e^2 n_0}{\varepsilon\varepsilon_0 k_B T}} = 1/\lambda_d$.

Thus by solving Eq. S14 in this 1D system, we can obtain the potential and E field distribution as:

$$\varphi(z) = \frac{1}{\varepsilon\varepsilon_0\kappa}\frac{1}{\sinh(\kappa d)}\left[\sigma_2\cosh(\kappa z) + \sigma_1\cosh(\kappa d - \kappa z)\right] \tag{2. 21}$$

$$E(z) = \frac{1}{\varepsilon\varepsilon_0}\frac{1}{\sinh(\kappa d)}\left[\sigma_2\sinh(\kappa z) - \sigma_1\sinh(\kappa d - \kappa z)\right] \tag{2. 22}$$

Recall Eq. S6 and Eq. S13, then we can calculate the electrostatic energy and free energy of this system:

$$U_{es} = \frac{1}{2\varepsilon\varepsilon_0\kappa}\frac{1}{2\sinh(\kappa d)}\left[\left(\sigma_1^2 + \sigma_2^2\right)\cosh(\kappa d) + 2\sigma_1\sigma_2 - \frac{\kappa d}{\sinh(\kappa d)}\left(\sigma_1^2 + \sigma_2^2 + 2\sigma_1\sigma_2\cosh(\kappa d)\right)\right] \tag{S1}$$

$$F = \frac{1}{2\varepsilon\varepsilon_0\kappa}\frac{1}{\sinh(\kappa d)}\left[\left(\sigma_1^2+\sigma_2^2\right)\cosh(\kappa d)+2\sigma_1\sigma_2\right] \quad (2.\ 23)$$

And the ion distribution can also be calculated by using Boltzmann distribution:

$$n_{\pm}(z) = n_0 \exp\left(\mp\frac{e\varphi}{k_B T}\right) \quad (2.\ 24)$$

# Chapter 3

# Light Extraction from Flip-chip GaN LEDs based on Dynamic Nano-inscribing (DNI) Patterning Technique

## 3.1 Introduction

GaN-based nitride compound semiconductors are very attractive materials due to their superior material properties and their versatility for use in a variety of optoelectronic applications such as light-emitting diodes (LEDs), solar cells, and laser diodes [39]. In particular, III-nitride based LEDs have been considered as a candidate of next generation solid-state light sources for replacement of general lighting sources such as florescent lamps due to their environmentally friendly properties and long lifetime (~40,000 hrs) [40]. Currently, the internal quantum efficiency of GaN-based LEDs can exceed 90%, but the external quantum efficiency is relatively low due to total internal reflection (TIR) of the generated light at the nitride-air interface resulting from their very different refractive indices [41], [42]. Numerous methods have been explored to solve the problem of inefficient optical extraction and the most well-established one is the Patterned Sapphire Substrate (PSS) technique [43]. Patterning on the substrate scatters a large number of photons emitted outside the TIR escape cone back into the cone, which helps more light to be extracted, creating an effect equivalent to increasing the critical angle of the escape cone. As a result, light extraction efficiency has been found to increase by as much as

30%[43]. Though PSS works very well to break the TIR at the GaN-Sapphire interface, there is still a lot of light trapped in the ITO electrode or the sapphire substrate for the flip-chip LED. These modes are typically called substrate modes and in order to overcome the total internal reflection at the substrate–air interface, many methods such as microlens arrays [44]–[46] and microsphere scattering layers[47] have been used. Though these structures can efficiently extract the substrate mode especially on OLED structure, but all those structures are at micro-scale and utilize geometric optical reflection/refraction induce light extraction.

Here in this work, based on sinusoidal grating structures fabricated by 1D dynamic nano-inscribing (DNI) patterning technique[34], [35], we investigate and present a mask-free, low-cost and highly scalable method of light extraction from flip-chip GaN LED by using such nano-scaled structure with which interference governed scattering and photon dynamics are counted. Significant improvements in light extraction from blue LEDs are achieved. A theoretical analysis is conducted using a mixed-level simulation combining rigorous coupled-wave analysis (RCWA) and Monte Carlo ray-tracing methods in which both the particle and wave nature of photon are considered. Those analysis provide general working and design principles of the nano-grating based light extraction and agree well with the experimental results.

## 3.2 Methods and materials

### 3.2.1 DNI nanograting mold fabrication

The proposed light-extraction is accomplished by using a nanostructured 1D grating pattern with sinusoidal profile on a polymer substrate using the Dynamic Nano-Inscribing (DNI) technique. All polymer substrates (PET and PC from Tekra Corp.) were used as purchased and cleaned using IPA followed by nitrogen drying before the patterning process. For Performing DNI, we prepare a well-cleaved SiO2 nanograting mold containing the desired pattern along the edge; then bring the mold edge in contact with the substrate at a proper angle and force, and then slide the mold edge over the substrate while maintaining a conformal contact. The polymer surface is plastically deformed by the nano-features on the mold edge, leaving behind a well-defined 1D nanograting pattern. For 2D DNI, this process is subsequently repeated in the orthogonal direction, which produces the sinusoidal void pattern as shown in Figure 1. In DNI, the pattern period is dictated by that of the grating mold and voids of various sizes and geometry can be inscribed in a continuous manner at high speed (~ 1 m/min or greater). For instance, we used a SiO2 grating mold with 700 nm-period for 1D/2D nanovoid patterning in this work (unless otherwise noted in our data). Furthermore, the morphologies of the sinusoidal nanograting created by 2D-DNI can be specifically tailored by changing the substrate material, applied force, and processing temperature. More details of DNI processes along with mold preparation and cleaving procedure can be found elsewhere [34], [35].

### 3.2.2 Flip-chip GaN LED fabrication

The flip-chip GaN LED is fabricated from a bare GaN LED wafer. Figure 3.1 shows cross-sectional views and top views of the LED during the fabrication process. Step 1, inductively coupled plasma (ICP) etching based on $BCl_3/Cl_2$ gas chemistry is employed to define three via holes (40 μm in diameter) by etching through the p-GaN layer and MQW layer to expose the n-GaN layer. Step 2, electron-beam evaporated indium-tin oxide (ITO) transparent conductive layer (100-nm-thick) is deposited on top of the p-GaN layer followed by thermal annealing in N2 ambient at 540$^{o}$C for 20 minutes to improve Ohmic contact between the ITO and p-GaN. Step 3, the insulating DBR reflective layer comprising an array of alternating $SiO_2/TiO_2$ dielectric layers are deposited on the top of ITO and filled the via holes obtained in Step 1 to prevent light absorption by the opaque metal electrodes. The DBR layer is patterned by photolithography and then etched down to n-GaN layer to form three n-contact via holes (19 μm in diameter) and to p-GaN layer to form a plenty of p-contact via holes (13 μm in diameter) by ICP etching based on $CHF_3/Ar/O_2$ mixture gas.

P-contact via holes are uniformly arranged around n-contact via holes to enhance current spreading. By forming via holes and filling them with metal, current injection can be achieved.

Step 4, Cr/Pt/Au metal layer (20 nm/50 nm/1.5 μm) is evaporated to form n-type and p-type contacts through n- and p-contact via holes, respectively. Isolation trench is introduced to divide the Cr/Pt/Au metal layer into first n- and p-electrodes. Step 5, 500-nm thick $SiO_2$ insulating layer is deposited by plasma enhanced chemical vapor deposition (PECVD) for

passivation and isolation of the first n- and p-electrodes, followed by forming two n-interconnect holes (46 μm in diameter) and six p-interconnect holes (36 μm in diameter) defined by buffer oxide etchant (BOE) wet etching. Step 6, Cr/Pt/Au metal layer (20 nm/50 nm/1.5 μm) is evaporated to form second n- and p-electrodes, respectively. The AuSn bumps are then formed on the second n- and p- electrodes to serve as the bonding material for the flip-chip process. The first and second n-electrodes are connected through two n-interconnect holes, and the first and second p-electrodes are connected through six p-interconnect holes. The LED wafers are thinned down to be about 100 μm by mechanical grinding and polishing. Finally, the LED wafers are diced into chips with size of 254 × 838 $\mu m^2$.

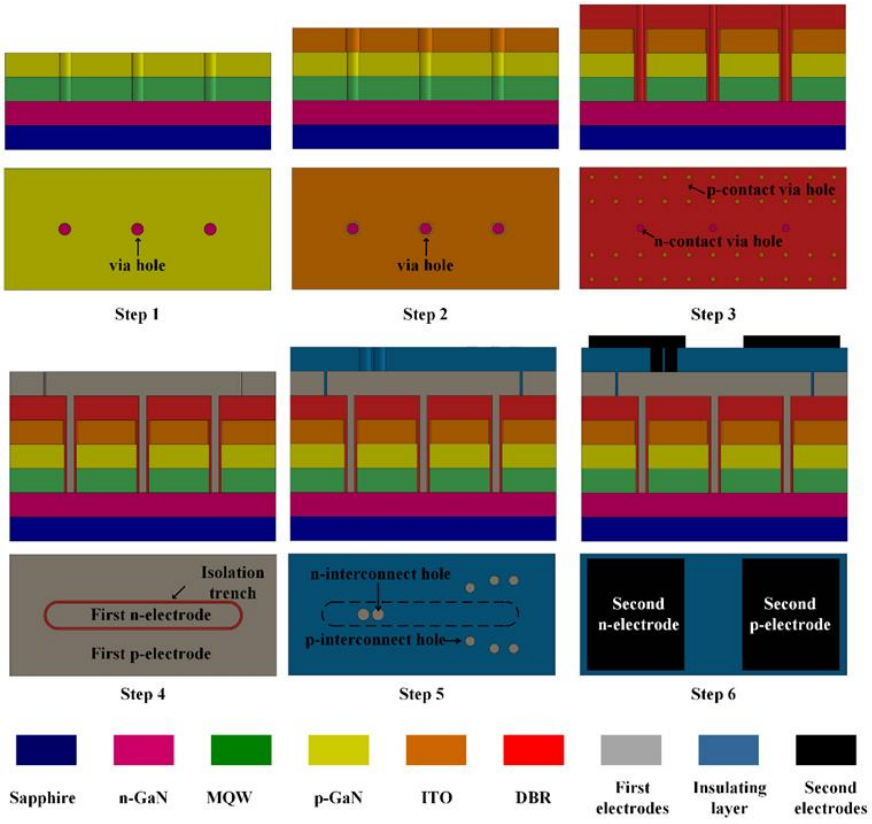


Figure 3.1: Schematic illustration of the process of flip-chip GaN LED fabrication.

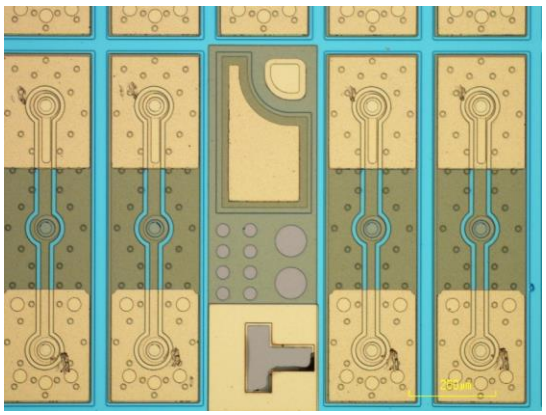

Figure 3.2: Microscope image of the back electrodes.

### 3.2.3 Nanograting integration

After preparing the flip-chip GaN LED, we treated the sapphire surface with oxygen plasma and spin coated with SU-8. Then a prepared PC DNI nanograting mold is placed on the surface of the SU-8 with the grating side facing the SU-8 surface. After the grating channels on the PC mold are fully filled with SU-8 polymer, a curling process is conducted under UV light till the SU-8 polymer is fully curled. Then a demolding process is taken place manually, leaving a stamped sinusoidal nanograting pattern on the SU-8 layer which is between the sapphire substrate and the air. The nanograting patterns are characterized by SEM, and a sinusoidal feature of 750nm in period and 200nm in depth have been confirmed. Figure 3.3 shows the integration process of the gratings to the flip-chip GaN LED. Figure 3.4 shows the SEM images of the gratings after integration.

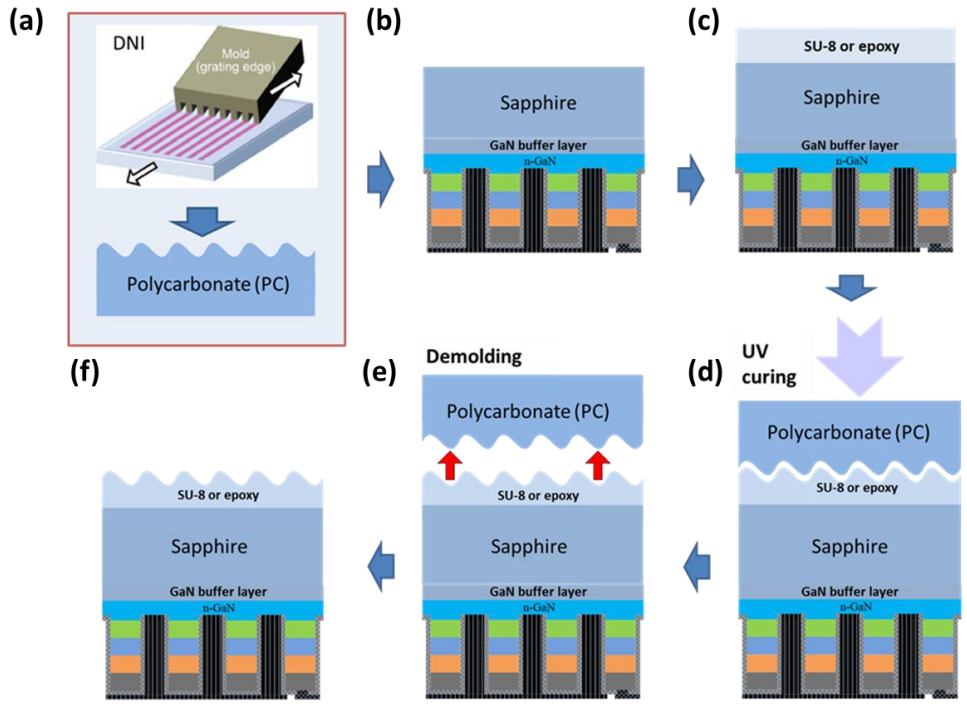


Figure 3.3: Light extraction nano-grating fabricated by a mask-free, stamping process. The figures show process of the nano-grating integrating with flip-chip GaN LED.

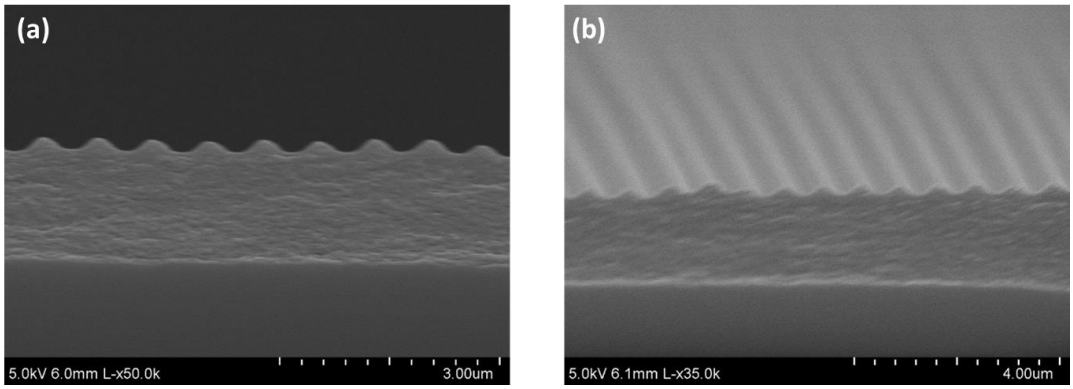


Figure 3.4: SEM images of the 1D DNI nanogratings.

### 3.2.3 Characterization

SEM imaging was performed using a Philips XL30-FEG at the typical operating voltage of 10-25 kV, after sputtering a thin Au film (≈3-5 nm) to avoid electron charging. An integration sphere was used to connecting all the light emitted by the LED and connected to a spectrometer (Ocean Optics HR4000) with optical fiber for the spectra measurement. The photocurrent measurement was done by using a semiconductor parameter analyzer (HP-4156A) and a calibrated Si photodiode.

## 3.3 Enhanced light emission from nanograting integrated LED

After integrating the flip-chip LED with the DNI nanogratings, we conduct experimental measurements to characterize the performance of the LEDs, in order to see the influence of the DNI nanograting on light extraction of the trapped mode in GaN LEDs.

Figure 3.5 shows experimental results for 1D DNI nanograting integrated flip-chip GaN LED. In Figure 3.5a, the measured photocurrent curves clear show the enhancement of factor of around 10% for the LED with the integrated 1D DNI structure. Besides, this enhancement was also verified in the EL spectrum measurement (Figure 3.5b). Here we also show an around 10% enhancement of the peak value of the spectrum. Interestingly, an obvious blue-shift (~3nm) of the spectrum were observed and if we calculate the enhancement as function of the wavelength, we can clearly see that the enhancement of the out-coupling efficiency is very sensitive to the wavelength of the light source. For our SU-8 grating, it can work very well in the short wavelength range (420~450nm) and an

enhancement of over 30% can be expected, while for the long wavelength region, it seems depress the light extraction efficiency.

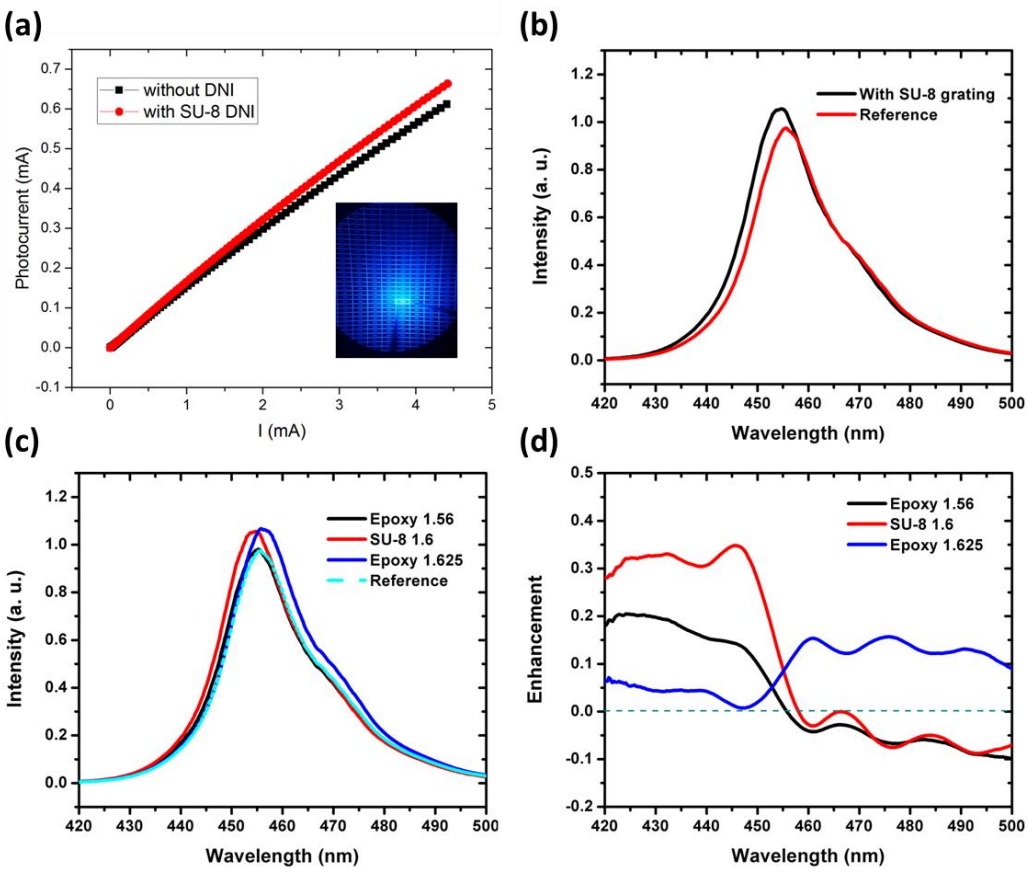


Figure 3.5: Experiment results of filp-chip GaN LED integrated with 1D DNI nanograting with period of 750nm and depth of 200nm. (a) Photocurrent vs. injection current (b) EL spectrum. (c) EL spectrum of 1D DNI nanograting with different materials. (d)Enhancement of the EL signal at different wavelength.

In order to test the index dependence of the grating, we tried different grating materials while keeping the grating features as the same. Figure 3.5c and d show the EL spectrum and enhancement spectrum with grating materials with different index. As is shown, the performance of the grating is also very sensitive to the index of the materials. For low index

materials like (epoxy 1.56), it will enhance the extraction efficiency in short wavelength range but depress it in the long wavelength range similar to SU-8. While for high index materials, the grating will actually work in the long wavelength range and depress the extraction efficiency in the short wavelength range. The wavelength-selectivity of the gratings can be explained by the photon momentum matching mechanism which will be discussed later on.

## 3.3 Simulation and modeling

### 3.3.1 General mechanism of light extraction from trapped mode

The trapped mode of light typically results from the momentum mismatch of photons in different media with different index, e.g. total internal reflection (TIR). Let's consider a planar system with Air as the final out-going media. In Air, only the photon modes with momentum $k_0$ can be supported, thus only photons with the parallel component of the momentum $k_{||}$ smaller than $k_0$ are allowed. As in planar systems, the parallel component of momentum conserves in all the layers, thus photons with parallel momentum initially greater than k0 have no way to come out if nothing is used to break the momentum conservation. Gratings are good candidate to break this momentum conservation as they can adding/subtracting momentum with the value well defined by the grating period. The use of grating is to scatter the incident field in order to reset the parallel momentum ($k_{||}$) of the photons, which give photons beyond the transmitting region a chance to return to the transmitting region ($|k_{||}|<k_0$). But there is a tradeoff here because the photons originally

within the transmitting region may also have the possibility to be scattered out of the transmitting region or absorbed by the grating.

Let's consider a general initial photon population distribution (F) in k (here k represents the k component along the grating axis). So the photons in the region ($-k_0<k<k_0$) can come out directly. If we consider the first order scattering of the grating are dominated over other order, which is applicable in most cases. The new photon population distribution is:

$$F_{new}(k) = F(k)\bullet P(k \to k) + F(k+k_g)\bullet P(k+k_g \to k) + F(k-k_g)\bullet P(k-k_g \to k) \quad (3.1)$$

Here P is the momentum transfer efficiency of the grating. $k_g$ represents the momentum change due to first order scattering. Thus, the new population of photons which can come out is:

$$\begin{aligned} F_{new}(-k_0 \sim k_0) &= \int_{-k_0}^{k_0} F(k)\bullet P(k \to k)\,dk \\ &+ \int_{-k_0+k_g}^{k_0+k_g} F(k)\bullet P(k \to k-k_g)\,dk + \int_{-k_0-k_g}^{k_0-k_g} F(k)\bullet P(k \to k+k_g)\,dk \end{aligned} \quad (3.2)$$

$$\begin{aligned} F_{new}(-k_0 \sim k_0) &= \int_{-k_0}^{k_0} F(k)\bullet P(k \to k)\,dk \\ &+ \int_{-k_0}^{k_0} F(k+k_g)\bullet P(k+k_g \to k)\,dk + \int_{-k_0}^{k_0} F(k-k_g)\bullet P(k-k_g \to k)\,dk \end{aligned} \quad (3.3)$$

Here by considering the fact that: $P(k_1 \to k_2) = P(k_2 \to k_1)$,

$$\begin{aligned} F_{new}(-k_0 \sim k_0) &= \int_{-k_0}^{k_0} F(k)\bullet P(k \to k)\,dk \\ &+ \int_{-k_0}^{k_0} F(k+k_g)\bullet P(k \to k+k_g)\,dk + \int_{-k_0}^{k_0} F(k-k_g)\bullet P(k \to k-k_g)\,dk \end{aligned} \quad (3.4)$$

If we only consider the first order scattering and absorption:

$$P\left(k \to k\right) + P\left(k \to k + k_g\right) + P\left(k \to k - k_g\right) + P_A\left(k\right) = 1 \tag{3. 5}$$

$$F_{new}\left(-k_0 \sim k_0\right) = F\left(-k_0 \sim k_0\right) - \bar{P}_A \bullet F\left(-k_0 \sim k_0\right)$$
$$+ \int_{-k_0}^{k_0} \left[F\left(k + k_g\right) - F\left(k\right)\right] \bullet P\left(k \to k + k_g\right) dk + \int_{-k_0}^{k_0} \left[F\left(k - k_g\right) - F\left(k\right)\right] \bullet P\left(k \to k - k_g\right) dk$$

(3. 6)

Here $\bar{P}_A$ is the average absorption coefficient. Thus the difference can be written as:

$$F_{new}\left(-k_0 \sim k_0\right) - F\left(-k_0 \sim k_0\right)$$
$$= -\bar{P}_A \bullet F\left(-k_0 \sim k_0\right)$$
$$+ \int_{-k_0}^{k_0} \left[F\left(k + k_g\right) - F\left(k\right)\right] \bullet P\left(k \to k + k_g\right) dk + \int_{-k_0}^{k_0} \left[F\left(k - k_g\right) - F\left(k\right)\right] \bullet P\left(k \to k - k_g\right) dk$$

(3. 7)

As we can see from this expression, if we want a great enhancement, we should expect:

(1) The absorption of the grating is low: $\bar{P}_A \to 0$

(2) High momentum transfer efficient: $P\left(k \to k + k_g\right) + P\left(k \to k - k_g\right) \to 1$

(3) $F\left(k \pm k_g\right) > F\left(k\right)$, or roughly:

$F\left(-k_0 + k_g \sim k_0 + k_g\right) + F\left(-k_0 - k_g \sim k_0 - k_g\right) > 2F\left(-k_0 \sim k_0\right)$, which means the regions which are $\pm k_g$ far away from the region $\left[-k_0, k_0\right]$ should have as many photons as possible. That means for a good design of the grating structure, we should channeling the highest photonic density region to the transmission region $\left[-k_0, k_0\right]$.

### 3.3.2 Mixed-level optical simulation

In order to understand the enhancement of the light out-coupling efficiency observed in our experiments, we developed a mixed-level model by combining rigorous coupled-wave analysis (RCWA) and Monte Carlo ray-tracing methods in which both the wave and particle nature of the photon are considered. In conventional LED simulation, Monte-Carlo ray-tracing methods are most commonly used in which light are treading as random beams and only the geometric optics are considered in the light-structure interaction, which is usually valid when the feature size is much larger than the wavelength. While in our case, a full wave treatment of the light-structure interaction is recalled as the grating features size is comparable with the wavelength. However, as the sapphire substrate is very thick (15um) in our LED devices, light transporting inside the sapphire substrate will lose the coherency. Thus in our simulation, the system can be divided into two part as is shown in Figure 3.6. In each part, a full wave treatment of the light-structure interaction are considered by using RCWA methods, while when photons are traveling between these two parts in the sapphire layer, only the energy are recorded and neglecting the phase information as the loose of the coherency.

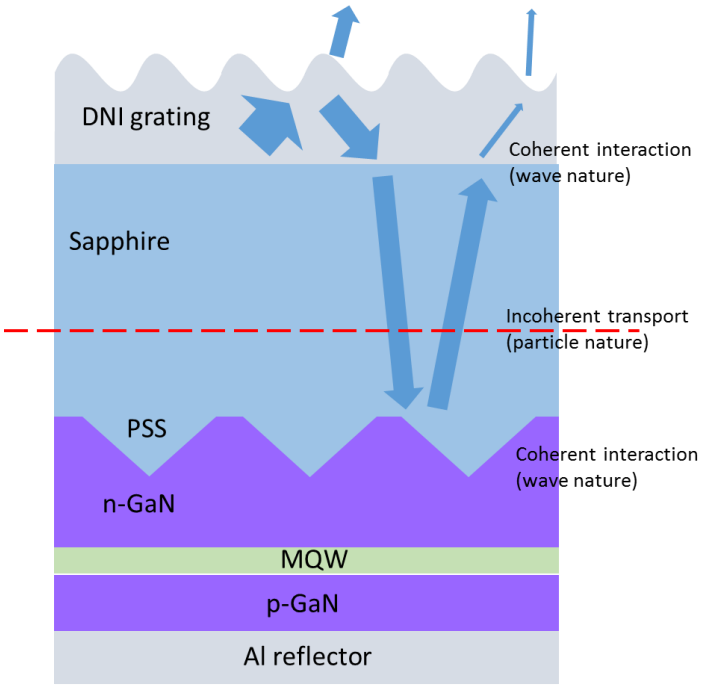


Figure 3.6: Mixed-level simulation system.

We assume that photons are generated randomly in the active MQW layer and the photon dynamics are simulated based on their transmission/scattering/reflection/absorption coefficients with the structures and multilayers. According to our calculation, because of the scattering of the PSS structure, the photon population distribution is also nearly random inside the sapphire layer. Thus, we can assume a randomly distributed photon source inside the sapphire layer and study the extraction efficiency with the DNI nanograting structure. Figure 3.7 shows the transmittance of the 1D DNI SU8 gating structure as we used for experiment. We calculate the transmittance as function of photons with different incident angle ($\theta$), conical angle ($\phi$) and polarization (TE or TM). As we can see here, nanograting actually work to scatter light and help the out-coupling of photons at large incident angle or momentum, while it also sacrifice quite amount of photons at small incident angle or of

small momentum. However, usually this kind of photon states exchange is beneficial as in lot of cases (e.g. random photon distribution), the population of photons at large incident angle/momentum are larger than those at small incident angle/momentum as is established in Figure 3.7. Thus by increasing the scattered transmittance of photons of high population and sacrifice those photons of low population at small incident angle, the overall extracted photon population will increase. According to this picture, the key design principles of a scattering type out-coupling structure are: (1) channeling the regions of highest photonic density of states in both the light-trapping media and the outside, which means transferring the trapped photons population into a highly transmitted channel and decrease the loss of the initially transmitted photons as low as possible; (2) high scattering efficiency as we want this photon states exchanges occurs efficiently; (3) low absorption of the gratings. More details about this theory can be found in the Section 3.3.1. With this model, it's easy to quantitatively explain the EL enhancement observed in our experiment. As is expected from Figure 3.7, the average out-coupling efficiency with the 1D DNI nano-grating is about 16.75% by averaging conical angles, polarizations and photon population, while the average out-coupling efficiency for the reference sample is only 15.15%, leading to a 10.55% enhancement of the out-coupling efficiency, which agree very well with our experiments.

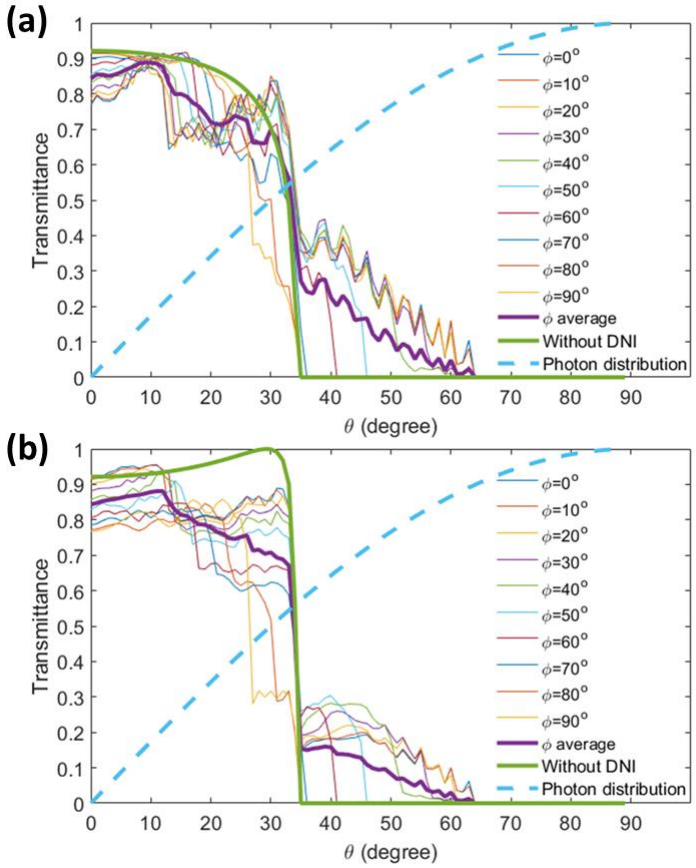


Figure 3.7: Simulated transmittance of the 1D DNI nanograting as function of photon properties: incident angle (θ), conical angle (ϕ) and polarization (TE (a) or TM (b)). The dashed light blue lines show the photon population distribution in the sapphire layer.

## 3.4 Conclusions

Based on DNI patterning technique, we experimentally demonstrate a single-step, low-cost methodology for light extraction from flip-chip GaN LED on a flexible substrate with nanograting patterns over a large area. This nanostructure induced light extraction were explained in the language of photon population exchange and momentum transferring by using a mixed level simulation in which both wave and particle nature of the photons are

considered. The patterning methodology used here can enable continuous and high speed production of 1D nano-patterns on flexible substrates. Application of this light extraction method could be extended to scalable out-coupling of trapped photon modes in other systems like OLED and hyperbolic metamaterials.

# Chapter 4

# Hyperbolic Metamaterials based on Ultra-thin, Low-loss, and Stable Al-doped Ag Films

## 4.1 Introduction

Planar multilayer structures are widely used in various photonic systems such as photonic crystal, color filter, antireflection coating, metamaterials, plamonic interconnects, organic solar cell and OLEDs. More specifically, hyperbolic metamaterials (HMMs), typically realized by alternative metal/dielectric multilayers, which are known to have a hyperbolic dispersion contour due to extreme anisotropy, recently drew much interest because of their unique photonic topology and ultrahigh photonic density of states (PDOS) in broad-band, leading to many applications such as enhancing spontaneous emission[48], thermal radiation[49], subwavelength lithography[50] and multimode resonators[51], [52]. An ideal hyperbolic metamaterial (HMM), which has a perfect hyperbolic dispersion curve, theoretically can support modes with indefinite wavenumbers, leading to infinitely large photon local density of states (LDOS) and ultrahigh light-matter interactions as promised by the effective media theory (EFM). However the promised hyperbolic topology of the iso-frequency surface and the ultrahigh PDOS are limited by the size of the building blocks and loss. Thus a lot of efforts have been taken to pursue high performance HMM by

breaking down the dimension of the building blocks, like using ultrathin metal films and even atomically-thin 2-D materials such as graphene.

Consequently, there is now a significant effort to explore alternative materials and methods to improve the performance of plasmonic metals[53] especially in low dimension. One material of significant interest is silver (Ag), as it has the highest performance ( $\mathrm{Re}\{\varepsilon\}/\mathrm{Im}\{\varepsilon\}$ ) of any plasmonic material in the visible and near infrared. Unfortunately, Ag is well documented to have several fundamental problems, including difficulty to form continuous thin films (< 15 nm), rough surface morphology, poor chemical and thermal stability, and inferior adhesion to popular substrates like silicon and fused silica[54]. In fact, spontaneous de-wetting for a thin Ag film occurs even at room temperatures[55] (such degradation is greatly accelerated even for modest temperatures ~100°C[56], [57]), whilst the entirety of Ag films can removed by ultrasonic vibrations or even Scotch tape[58].

Upon these issues, we developed an effective approach to achieve ultra-thin and smooth Ag film by co-depositing small amount of Al during the film deposition [59], [60]. Al could suppress Ag 3D growth mode and promote thin/smooth film formation. By using this methods, wetting-layer-free thin Ag films can be achieved for a thickness down to 6 nm with a sub-nanometer roughness on various substrates, including silicon, fused silica, and flexible substrates (e.g., PET films). Additionally, Al-doped Ag not only maintains Ag's superior optical properties, but also is shown to have a substantially improved substrate adhesion, and is stable at both room temperatures and elevated temperatures up to 500 °C[59], [60].

The details of the fabrication and characterization of this Al-doped Ag can be found elsewhere [59], [60]. Here in this chapter we are focusing on utilizing Al-doped Ag for building high-performance hyperbolic metamaterials.

## 4.2 Ultra-thin Al-doped Ag Films

The Al-doped Ag films were co-sputtered on fused silica substrates by a DC magnetron sputter tool (Lab18, Kurt J. Lesker Co.) with Argon (Ar) gas at room temperatures. The chamber base pressure was pumped down to about 1×10-6 Torr before the film deposition. During deposition, the Argon gas pressure was 4.5 mTorr and the substrate holder was rotated at a rate of 10 rpm. Two pure Ag and Al targets were co-sputtered to create Al-doped Ag films. By varying the source powers for Al and Ag targets, the composition of sputtered films was adjusted. The sputtering rates of Ag at 0.9 nm/s and Al at 0.06 nm/s produced Al-doped Ag films with optimized optical properties.

The scanning electron microscopy (SEM) and atomic force microscope (AFM) characterization have been used to check the morphology of the films. And the Al-doped Ag film has a smooth surface morphology with a significantly reduced root-mean-square (RMS) roughness less than 1 nm. The SEM characterization shows drastically different film morphologies between a 9 nm (nominal thickness) pure Ag film by sputtering (Figure 4.1a) and a 9 nm Al doped Ag film (Figure 4.1b). The grain or island-like morphology in Figure 4.1a is very typical for a pure thin Ag film. However, the 9 nm Al-doped Ag film is

very uniform and smooth. Besides, AFM images (insets in Figure 4.1a and b) confirm these results as the RMS roughness of 9 nm pure Ag film is 10.8 nm while the Al-doped Ag films has an over one order lower RMS value of 0.86 nm.

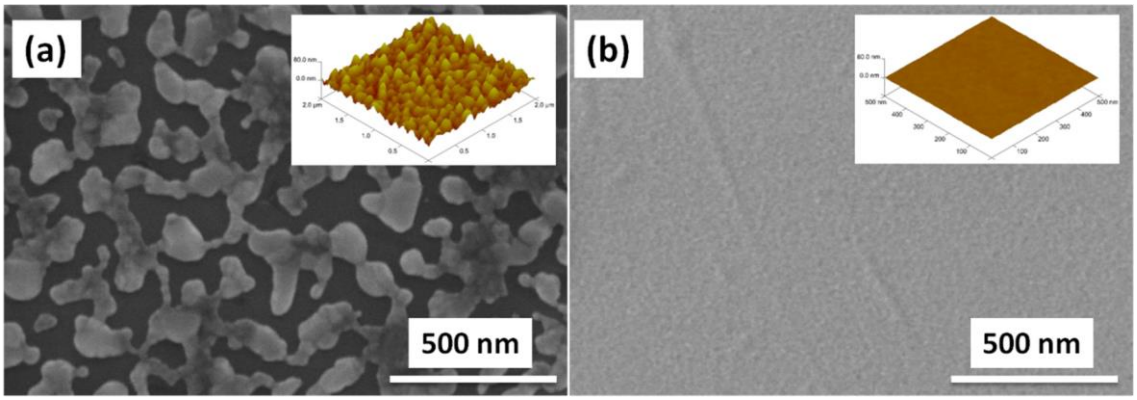


Figure 4.1: SEM and AFM images of pure Ag and Al-doped Ag film. SEM images of (a) 9 nm pure Ag film, (b) 9 nm Al-doped Ag film. The insets in each figure are their corresponding tapping mode AFM images. All films are deposited on fused silica substrates. The scale bar for AFM images in (a) and (b) is 80 nm. The scale bar for SEM images is 500 nm. The 9 nm pure Ag film has an RMS roughness of 10.8 nm, 12 times higher than 9 nm Al-doped Ag film (0.86 nm).

Thickness of these Al-doped Ag ultra-thin films and their corresponding optical properties were characterized by spectroscopic ellipsometry using the reflection plus transmission method[61]. In general ellipsometry measurement, there is a correlation between the thickness and the optical constants in thin absorbing films, as the reflection and absorption depend on both the film thickness and its optical coefficients. To break this correlation and precisely determine both the film thickness and its optical constants, "interference enhancement" method was used by depositing the metal film on the silicon substrate with a 300 nm thermal oxide layer on top[62].

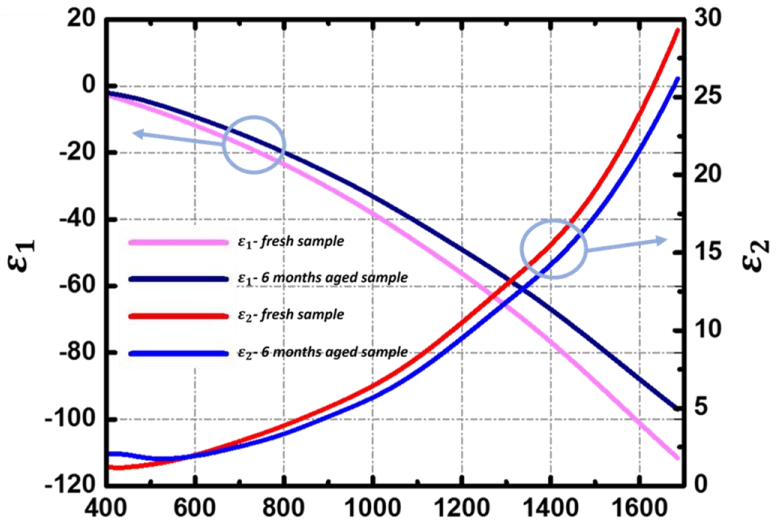


Figure 4.2: Measured permittvities of a freshly deposited 7nm Al-doped Ag film on fused silica substrate and a sample deposited 6 months ago, which show close values.

As is shown in Figure 4.2, the measured permittivites of these Al-doped Ag films are very close to the value of pure Ag. And the samples show pretty good long-term stability.

## 4.3 Hyperbolic metamaterials

HMMs are highly anisotropic structures which exhibit a metallic response (i.e., $\mathrm{Re}\{\varepsilon\} < 0$) in one (two) directions and a dielectric response (i.e., $\mathrm{Re}\{\varepsilon\} > 0$) in the other two (one) directions. Such a high anisotropy endows HMMs with a theoretically unbounded hyperbolic dispersion and thus, an ultra-high photonic density of states (PDOS)[63].

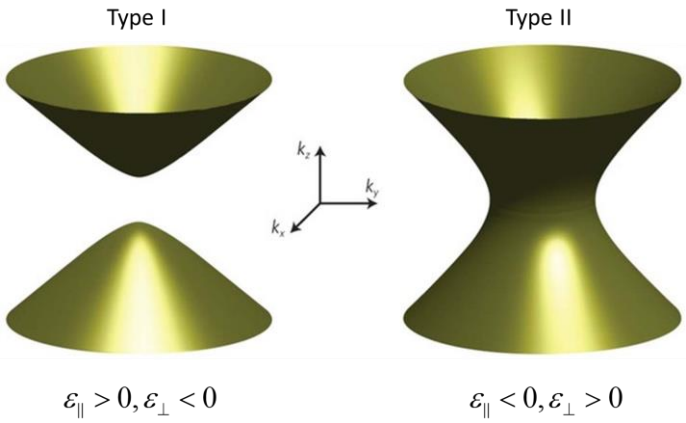


Figure 4.3: Iso-frequency surface of type I and type II hyperbolic metamaterials.

One way to fabricate HMMs is by depositing alternating layers of thin metal and dielectric films (inset of Figure 4.4a), leading to a dielectric response (i.e., $\mathrm{Re}\{\varepsilon_{\perp}\} > 0$) in the direction normal to the layers and a metallic response (i.e., $\mathrm{Re}\{\varepsilon_{\parallel}\} < 0$) in-plane. The electromagnetic response of such HMMs is described by an effective magnetic permeability equal to the value of the free-space, and an effective electric permittivitity in the tensor form: $\varepsilon_{eff} = \begin{pmatrix} \varepsilon_{\parallel} & 0 & 0 \\ 0 & \varepsilon_{\parallel} & 0 \\ 0 & 0 & \varepsilon_{\perp} \end{pmatrix}$, where $\varepsilon_{\parallel}$ and $\varepsilon_{\perp}$ are complex values ($\varepsilon_{\parallel} = \varepsilon'_{\parallel} + i\varepsilon''_{\parallel}$ and $\varepsilon_{\perp} = \varepsilon'_{\perp} + i\varepsilon''_{\perp}$).

The dispersion relation of HMMs is given by: $k_x^2/\varepsilon_{\perp} + k_z^2/\varepsilon_{\parallel} = k_0^2$, where $k_x$ and $k_z$ are the complex amplitudes of the transverse and normal components of the complex wave-vector, and $k_0$ the free-space wave-vector (with respect to the coordinate system in figure 4.4a). Since $\varepsilon'_{\parallel} < 0$ and $\varepsilon'_{\perp} > 0$, HMMs are governed by hyperbolic iso-frequency curves. For example, in the case of the HMM shown in Figure 4.4a (four periods of 7nm

Al-doped Ag and 20 nm $Ta_2O_5$ films), the measured $\varepsilon'_{\parallel}$ and $\varepsilon'_{\perp}$ at 700 nm are -1.41529 and 7.86797, respectively. This leads to a dispersion curve plotted in Figure 4.4b. There is a cut-off band defined by $|k_x| < k_c$, where $k_c = \sqrt{\varepsilon_{\perp}} * k_0$. Electromagnetic waves with transverse wave-vector $k_x$ located within this band decay evanescently in the z direction. In contrast, for electromagnetic waves with transverse wave-vectors $|k_x| > k_c$, they are propagation modes in the HMM (high-k modes)

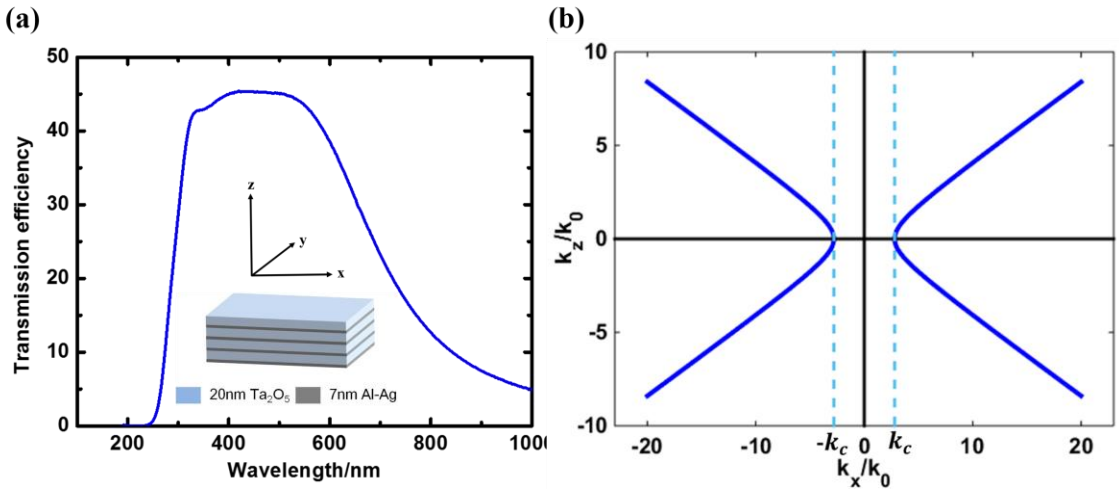


Figure 4.4: (a) Measured transmission efficiency of the fabricated HMM consisting of 4 period of 7 nm Al-doped Ag and 20 nm $Ta_2O_5$. The inset is its schematic drawing. (b) Dispersion curve of HMM at 700 nm. The HMM supports the propagation of modes with transverse wave-vectors larger than $k_c$.

However, there is a limit of the maximal allowed high-k modes, which is determined by the inverse of the HMM unit cell size, *i.e.*, $\Lambda = t_{metal} + t_{dielectric}$. This is because that at a large value of $k_x$, the normal component of wave-vector $k_z$ is also large (consistent with the hyperbolic dispersion). Consequently, the effective wavelength ($\lambda_z = \frac{2\pi}{k_z}$) along the normal direction is getting comparable with the unit size cell and therefore, the effective

medium theory approximation breaks down. Instead, the photonic band structures originating from the multi-layer configurations of HMMs should be considered, which seriously compromises the ultra-high PDOS predicted by the theoretical hyperbolic dispersion of HMMs. Therefore, it is desirable to have thin constituent layers in HMMs. Also, maintaining thin constituent layers increases the transmission per period and enabling light to propagate farther into the material. However, since it is challenging to obtain thin and smooth Ag films, most reported HMMs use relatively thick (and rough) Ag films, and suffer from a lossy and non-homogeneous response (e.g., oscillating transmission spectra which deviates from effective medium theory). In contrast, the ultra-thin and smooth Al-doped Ag films greatly improve upon these limitations, facilitating the fabrication of low-loss and homogeneous HMMs with a high transmission, small unit cell size, and optical properties which are well approximated by effective medium theory.

## 4.4 High performance hyperbolic metamaterials based on ultrathin Al-doped Ag films

The fabricated HMM consists of four periods, alternating layers of 7 nm Al-doped Ag and 20 nm $Ta_2O_5$, starting with the Al-doped Ag film on the fused silica substrate (inset of Figure 4.4a). The measured transmission at normal incidence is plotted in Figure 4.4a. It has both a high and smooth transmittance across the visible range, which benefits from the ultrathin, smooth and low-loss metallic layer.

The structure's optical properties were characterized using spectroscopic ellipsometry (M2000, J. A. Woollam Co.), where the HMM was modelled as a uniaxial anisotropic medium with different in-plane (parallel) and out-of-plane (perpendicular) optical constants. The simulated and measured permittivities are plotted in Figures 6.5a and b (real and imaginary part, respectively), which corresponds closely with each other. In the parallel direction, the epsilon near zero (ENZ) point is around 610 nm, and beyond this wavelength, the HMM's dispersion transits from an ellipsoidal to hyperbolic behavior.

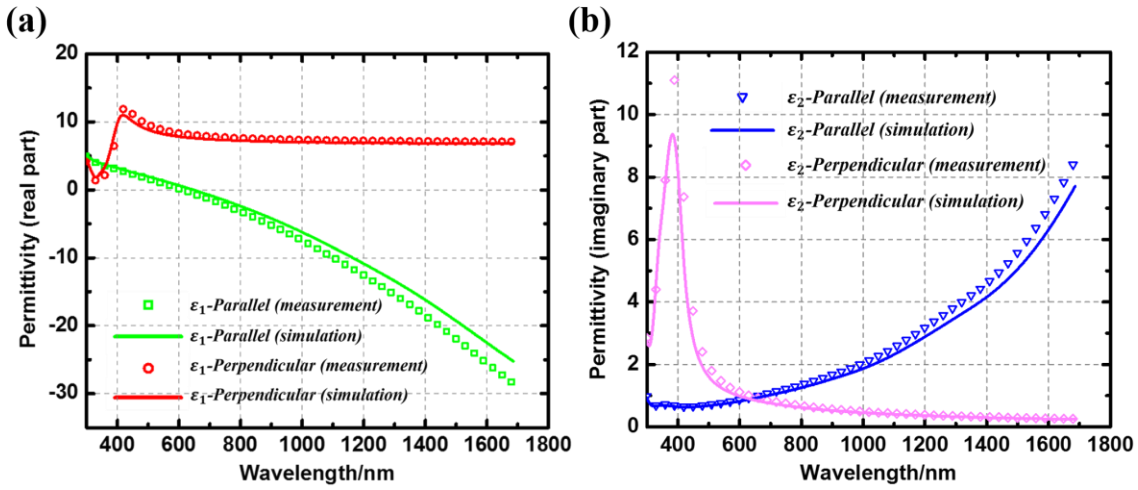


Figure 4.5: Measured permittivities of the fabricated HMM. (a) Simulated (solid curve) and measured (dotted curve) of the real part of the permittivity of the fabricated HMM. The permittivity along the parallel direction turns into negative beyond 610 nm and therefore, the HMM has a hyperbolic dispersion. (b) Simulated (solid curve) and measured (dotted curve) of the imaginary part of the permittivity of the fabricated HMM.

As noted previously, the maximal allowed high spatial wave-vectors (high-k modes) in HMMs are determined by the inverse of HMM unit cell sizes. One way to demonstrate this is by examining the transmission amplitude of an electromagnetic wave with a large-value $k_x$ through the HMM[64]. Figures 4.6a and b show the local photonic density states

distribution vs $k_x$ values in HMM, which have an identical thickness and ratio of metal-dielectric layers, but a different unit cell size. The HMM considered in Figure 4.6a consists of 8 periods of 7 nm Al-doped Ag and 20 nm $Ta_2O_5$, while the HMM in Figure 4.6b consists of 4 periods of 14 nm Al-doped Ag and 40 nm $Ta_2O_5$. Although these HMMs have an identical ratio and total thickness of metal and dielectric layers (thus an identical behavior predicted by the effective media theory), the HMM with thinner constituent layers supports a much broader transmission band for high-k modes, which contributes to a larger photonic density of states (PDOS)[65]. A high PDOS is essential to many extraordinary phenomena enabled by HMMs (broadband absorption, enhanced spontaneous/stimulated emission, engineered thermal radiation, etc). As an example, for a dipole emitter located 10 nm above the HMM, the Purcell enhancement factor of the emitter on top of HMM with thinner layers is much larger than that of the emitter on top of HMM with thicker layers (Figure 4.7).

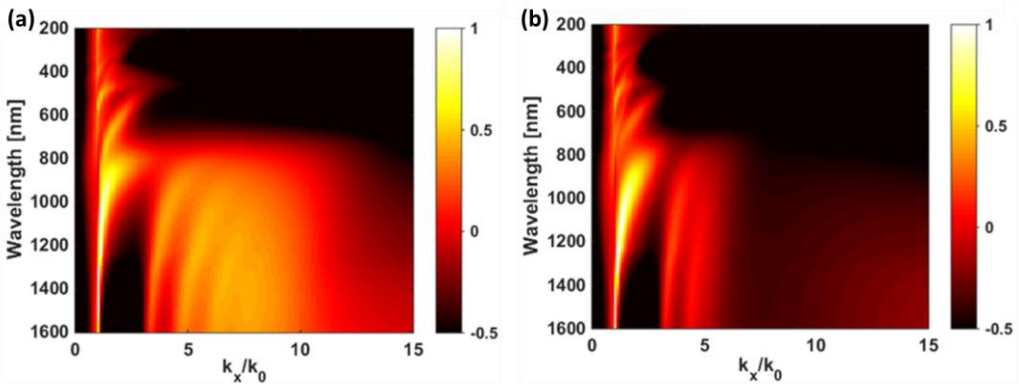


Figure 4.6: (a) Calculated transmission amplitude of an electromagnetic wave with different transverse wave-vectors ($k_x$) through a HMM made of 8 periods of 7 nm Al-doped Ag and 20 nm $Ta_2O_5$. (b) Calculated transmission amplitude of an electromagnetic wave with different transverse wave-vectors ($k_x$) through a HMM made of 4 periods of 14 nm Al-doped Ag and 40 nm $Ta_2O_5$. HMM consisting of thinner constituent layers supports a broader bandwidth of high-k modes.

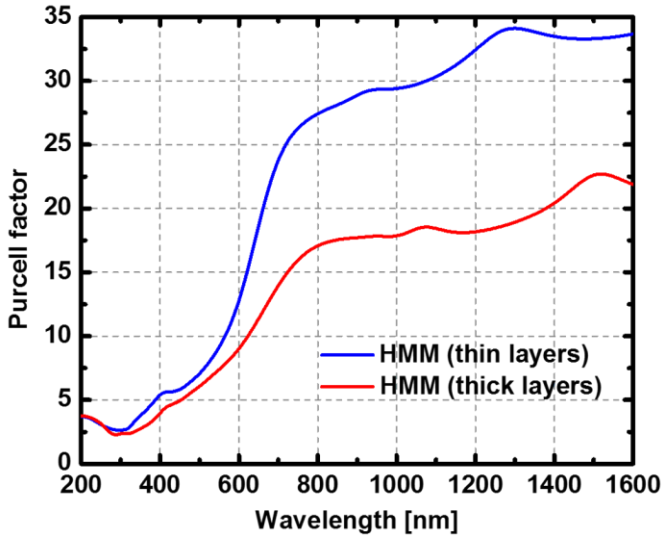


Figure 4.7: Calculated Purcell factor of a dipole emitter located 10 nm above two HMMs studied in Figure 4.6a and 4.6b. The Purcell factor is averaged over different dipole orientations (2/3 contribution from parallel dipoles and 1/3 contribution from vertical dipoles). HMM with thinner constituent layers provides a larger Purcell factor.

In a planar system, when a dipole is placed at a distance d above a single or multilayer films with a perpendicular (⊥) or parallel (∥) orientation to the interfaces, the corresponding Purcell factors F can be written as the following:[66], [67]

$$F_{\perp} = 1 - \eta_0 + \frac{3}{2}\eta_0 \mathrm{Re}\left[\int_0^{\infty} dk_x \frac{1}{k_z}\left(\frac{k_x}{\sqrt{\varepsilon_1}k_0}\right)^3 \left(1 + r_p e^{2ik_z d}\right)\right] \quad (4.1)$$

$$F_{\parallel} = 1 - \eta_0 + \frac{3}{4}\eta_0 \mathrm{Re}\left[\int_0^{\infty} dk_x \frac{1}{k_z}\frac{k_x}{\sqrt{\varepsilon_1}k_0}\left(1 + r_s e^{2ik_z d} + \frac{k_z^2}{\varepsilon_1 k_0^2}\left(1 - r_p e^{2ik_z d}\right)\right)\right] \quad (4.2)$$

Here, $\eta_0$ is the internal quantum efficiency of the emitter in free space and is assumed to be unity in this calculation. $k_x$ and $k_z$ are the components of the wave-vector along the x and z axis, respectively. $k_0$ is the free-space wave-vector. $r_s$ and $r_p$ are the reflection

coefficients of the structure at the interface for an s and p polarized light, and are calculated using the transfer matrix method. $\varepsilon_1$ is the relative permittivity of the host media of the emitter and is unity in this calculation. The integrands in the above two equations refer to the normalized dissipated power spectra, which represents the energy emitted into different dissipation channels. In the case of isotropic orientated emitters (2/3 contribution from parallel dipoles and 1/3 contribution from vertical dipoles), the average Purcell factor can be calculated as: $F = \frac{1}{3}F_{\perp} + \frac{2}{3}F_{\parallel}$.

## 4.5 Conclusions

This chapter presents one specific application of planar metal/dielectric multilayer structures: hyperbolic metamaterials (HMM). And indeed the performance of HMMs can be improved by using ultrathin and low loss building layers such as the ultrathin and smooth Al-doped Ag films as we established here. HMMs consisting of these thin constituent layers of Al-doped Ag films have both a low-loss and homogenous response. Moreover, they support a broader bandwidth of high-k modes as well as higher photonic density of states (PDOS) compared to HMMs made of thicker layers, which are highly desired for systems require ultra-strong and ultrafast light-matter interactions.

# Chapter 5

# Hyperbolic Metamaterial based on Ultrathin Building Blocks: Nonlocality Induced Topological Transitions

## 5.1 Introduction

As we mentioned in last Chapter, an ideal hyperbolic metamaterial (HMM), which has a perfect hyperbolic dispersion curve, theoretically can support modes with indefinite wavenumbers, leading to infinitely large photon local density of states (LDOS) and ultrahigh light-matter interactions as promised by the effective media theory (EFM). But in practice, one of the main factors that limits the performance of HMM is the finite size of the unit-cell. When the thickness of the unit-cell becomes large as compared with wavelength, the EFM theory starts to break down. Instead, photonic crystal like band structures will appear[68] in the dispersion, and the high k modes as well as the ultrahigh LDOS as promised by effective media theory will be seriously limited[63]. The topology of the iso-frequency surface will be changed and even spit into different branches[69], which dramatically change the way of wave propagation and the optical properties of the metamaterials for both high k and low k regions. On the other hand, with recent interest in atomically-thin 2-D materials[70] (e.g. graphene) and the ability to fabricate ultrathin and low-loss metal films[71], [72], the optical properties of the HMMs will improve

dramatically due to the reduction of unit-cell thickness. Thus it's natural to raise the question whether the ideal HMM and ultrahigh LDOS can be realized as promised by the effective media theory if we can make the building layers thinner and thinner, even down to atomic level e.g. by using some 2D materials?

In this work, based on the hydrodynamic model[73], [74] of the nonlocal response of electrons and a transfer-matrix method considering both the transverse and longitudinal modes, we investigate the effect of nonlocality on the performance (such as dispersion relation, ray refraction, local density of states and spontaneous emission) of HMMs based on ultrathin metal-dielectric multilayers. We find that nonlocality will induce topological transitions of the iso-frequency surfaces of both type I and type II HMMs and intrinsically limit the wavenumber as well as photon local density of states. Those effects give an alternatively explanation to the plasmonics behaviors of monolayer and multilayers graphene materials. We also discuss the influence of electron diffusion kinetics and electron spill-out effects based on the newly developed generalized nonlocal optical response model (GNOR) [75] and self-consistent hydrodynamic model (SC-HDM)[76] respectively. The underling physics will be illustrated as well.

In order to probe the ultrathin limit of the building layers, we should be careful to re-examine the assumptions used in conventional E&M theory. Under conventional E&M, the electron response in a metal are described by the local theory in which the response only depends on the local field and the induced charges are confined in a surface. But in

reality, the induced charge densities cannot be perfectly localized at the surface but spread over a thickness described by the Tomas-Fermi screening length as shown in Figure. 5.1a due to the electron-electron interactions from Coulomb repulsion and degeneracy pressure[74], [77]. Thus in this case, nonlocal treatment of the electron response is required. Actually, this effect have been widely investigated in many plasmonic systems both theoretically and experimentally, and showing that it has significant influence on systems with near-atomic length scale, such as diminishing the impact of geometric singularities[78], blue-shifting plasmonic resonance[79]18, limiting light concentration and plasmonic enhancement due to the nonlocality [73].

One of the most popular models to describe the nonlocal response of electrons in plasmonic nanostructures is the hydrodynamic Drude model (HDM). As compared to conventional Drude model, HDM introduces one term related to the electron-electron interaction induced pressure to the equation of motion of the electron gas[74]. According to the Tomas-Fermi theory, this pressure term can be expressed in the form of electron density by taking into account the fermion statistics of the electrons. As conclusion of this model, the induced charges are no longer perfectly confined in the metal surface but spread over a thickness inside the metal. Moreover, by solving the equation of electron response together with the Maxwell's equations, one can find that apart from the normal transverse mode in the local theory and the permittivity described by a local Drude model, there is another longitudinal mode characterized by a spatially dispersive permittivity according to the

hydrodynamic model, which only exists under the nonlocal response. Details about the HDM can be found in the Methods section.

Moreover, some recent works have shown that not only the electron-electron interactions, but also some other quantum effects can add new features to this nonlocality when dealing with near atomic level plasmonic systems[75], [76],[79]–[81]. Mortensen et al.[75] developed a semi-classical generalized non-local optical response theory (GNOR) considering both quantum pressure convection effects and the induced charge diffusion kinetics, which successfully explained not only the frequency shifts, but also size dependent damping as well as broadening in plasmonic metallic nanoparticle systems which cannot be explained by the standard HDM. In a recent work, David et al.[82] showed that a better agreement between the HDM results and experimental data can be obtained if the spill-out of conduction band electrons into dielectric region is considered and an equilibrium electron density from density functional theory (DFT) calculations is employed. They found that this electron density profile at the metal surface (both inside metal and spill-out in the dielectric region) as well as induced tunneling effect are of critical importance for quantitatively predicting the surface optical response. More recently, Toscano et al.[76] introduced a semi-classical self-consistent hydrodynamic model (SC-HDM) in which both the ground state and induced inhomogeneous electron gas can be determined self-consistently instead of using quantum-mechanical ab initio approach but are in good agreement with experiments and more advanced quantum methods. In that work, redshift instead of blueshift of surface plasmon resonance and a Bennett resonance

have been observed in the systems of sub-2nm nanowires and particles of alkali metals where the electron density spill-out effect shows much stronger influence on the plasmonic response.

Based on these facts, it is of great importance and interest to study the influence of the nonlocal effects on the performance of hyperbolic metamaterials when the size of unit-cell is approaching the ultrathin limit or atomic level. Some pioneering works conducted by Yan et al.[83], [84] on hyperbolic metamaterials with nonlocal response based on standard hydrodynamic model showed that the nonlocal effect regularize broadband super-singularity and limits the PDOS of a multilayer type II HMM. Upon the application for hyperlens, the nonlocal response can blueshift the optimal imaging frequency with respect to that based on the local response theory. However, these works have focused on type II HMM at low frequency range and its optical performance in certain specific applications. However there have been lack of studies on the photonic topology and the underlying physical origin of these effects. Moreover, the contemporary theories on this topic are based on typical hydrodynamic model that only considers the electron-electron interaction induced nonlocal correction, which presents opportunity to study the other quantum effects such as electron diffusion kinetics and electron spill-out effect as well as tunneling which have been proved of equal importance in most recent papers[75], [76], [82].

## 5.2 Methods

### 5.2.1 Hydrodynamic model (HDM)

The hydrodynamic Drude model (HDM)[74], [85], [80] of the electron gas is one of the most commonly used methods to describe the nonlocal response of electrons. In this model, The motion of free electrons can be described in terms of hydrodynamic variables: the charge density n(r,t), the electron fluid velocity v(r,t), and the electron pressure p(r,t). Thus the equation of motion for the electron fluid under an applied E&M field can be written as[74]:

$$n\frac{\partial \mathbf{v}}{\partial t}+n\left(\mathbf{v}\cdot\nabla\right)\mathbf{v}+\gamma n\mathbf{v}=-\frac{ne}{m_e}\left(\mathbf{E}+\mathbf{v}\times\mathbf{B}\right)-\frac{\nabla p}{m_e} \tag{5. 1}$$

Here $\gamma$ is the damping of the electrons, $m_e$ is the electron effective mass. By defining the current density $\mathbf{J}=-en\mathbf{v}$ , and using the equation of continuity:

$$\dot{n}=\frac{1}{e}\nabla\bullet\mathbf{J} \tag{5. 2}$$

we get:

$$\frac{\partial \mathbf{J}}{\partial t}-\frac{\mathbf{J}}{en}\nabla\bullet\mathbf{J}-\mathbf{J}\bullet\nabla\left(\frac{\mathbf{J}}{en}\right)-\gamma\mathbf{J}=\frac{ne^2}{m_e}\mathbf{E}-\frac{e}{m_e}\mathbf{J}\times\mathbf{B}+e\frac{\nabla p}{m_e} \tag{5. 3}$$

By neglecting the high order terms and defining the electric polarization vector $\boldsymbol{P}=\dot{\boldsymbol{J}}$ , then we can get the equation of the electron response related to the electron pressure:

$$\ddot{\boldsymbol{P}}+\gamma\dot{\boldsymbol{P}}=\frac{ne^2}{m_e}\boldsymbol{E}+\frac{e}{m_e}\nabla p \tag{5. 4}$$

We can see clearly that the only difference compared to conventional Drude model is to add one term related to the electron-electron interactions induced pressure, which can be expressed in form of electron density based on Thomas-Fermi theory:

$$p(\boldsymbol{r},t)=\xi n(\boldsymbol{r},t)^{5/3} \tag{5. 5}$$

Here $\xi=\left(3\pi^2\right)^{2/3}h^2/\left(5m_e\right)$ and h is the Plank constant. Based on this model, we can write the new equation for electron response as:

$$\beta^2\nabla\left(\nabla\bullet\boldsymbol{P}\right)+\left(\omega^2+i\gamma\omega\right)\boldsymbol{P}=-\varepsilon_0\omega_p^2\boldsymbol{E} \tag{5. 6}$$

Here $\beta^2=\frac{3}{5}v_F^2$ [80], [81], [86]is a measure of the strength of the nonlocality and only depends on the Fermi velocity of the metal $v_F$. And here $\omega_p$ is the plasma frequency. By solving this equation of electron response together with the E&M wave equation:

$$\nabla\times\nabla\times\mathbf{E}-\frac{\omega^2}{c^2}\mathbf{E}=\omega^2\mu_0\mathbf{P} \tag{5. 7}$$

we can find out that for nonlocal response, there are actually two modes in the metal: one is the conventional transverse mode as in the local theory and its permittivity is described by a local Drude model (eqs 8); and the other is the longitudinal mode characterized by a spatially dispersive permittivity according to the hydrodynamic model, which only exists under nonlocal response (eqs 9):

$$\varepsilon_T\left(\omega\right)=\varepsilon_\infty-\omega_p^2/\left[\omega\left(\omega+i\gamma\right)\right] \tag{5. 8}$$

$$\varepsilon_L\left(\mathbf{k},\omega\right)=\varepsilon_\infty-\omega_p^2/\left[\omega\left(\omega+i\gamma\right)-\beta^2\left|\mathbf{k}\right|^2\right] \tag{5. 9}$$

And the propagating *k* values for the transverse and longitudinal modes are:

$$k_T^2=\varepsilon_T k_0^2 \tag{5. 10}$$

$$k_L^2 = \frac{\omega(\omega + i\gamma) - \omega_p^2 / \varepsilon_\infty}{\beta^2} \tag{5. 11}$$

We should notice that when the frequency is higher than the plasma frequency, the longitudinal mode will become a propagating mode and at high frequency region, the *k* value becomes:

$$k_L \approx \frac{\omega}{\beta} = k_0 \frac{c}{\beta} \tag{5. 12}$$

which defines the upper limit of the allowed longitudinal mode in the metal and also defines the cutoff *k* value we observed for the allowed modes in multilayer metamaterials. By combing the hydrodynamic model and a transfer-matrix method considering both transverse and longitudinal modes in the metal, we studied the optical properties of HMMs as the unit cell changes from finite thickness to atomically thin.

### 5.2.2 Generalized nonlocal optical response model (GNOR)

In GNOR[81], [86], [75], not only the quantum pressure due to electron-electron interactions but also the diffusion due to density gradient has been considered. In conventional hydrodynamic model (HDM), the response of the induced current is governed by:

$$\frac{\beta^2}{\omega(\omega + i\gamma)} \nabla\left(\nabla \bullet \boldsymbol{J}_{conv}\right) + \boldsymbol{J}_{conv} = \sigma_D \mathbf{E} \tag{5. 13}$$

Here $\boldsymbol{J}_{conv} = (-e) n_0 \boldsymbol{v}$ is the convection current, and $n_0$ is the background electron density and $\sigma_D$ is the usual Drude conductivity. In GNOR model, by considering the electron diffusion, the new induced current is given by Fick's law:

$$\boldsymbol{J} = (-e) n_0 \boldsymbol{v} - D\nabla(-e) n_1 \tag{5. 14}$$

Here $D$ is the diffusion constant and $n_1$ is the induced electron density. After solving the equation-of-motion, finally we can get the new response equation[75]:

$$\xi^2 \nabla(\nabla \bullet \boldsymbol{J}) + \boldsymbol{J} = \sigma_D \mathbf{E} \tag{5. 15}$$

$$\xi^2 = \frac{\beta^2}{\omega(\omega + i\gamma)} + \frac{D}{i\omega} = \frac{\beta^2 + D(\gamma - i\omega)}{\omega(\omega + i\gamma)} \tag{5. 16}$$

Compared with the conventional HDM, we can see clearly that the only difference is that the nonlocal parameter modified into a complexed value: $\beta^2 \to \beta^2 + D(\gamma - i\omega)$. Thus implementation of this model is straightforward as we can keep the framework of the HDM and just replace the nonlocal parameter with this complexed value. More details about this model can be found in ref 1.

### 5.2.3 Self-consistent hydrodynamic model (SC-HDM)

Both the HDM and the GNOR are not considering the electron spill-out effect as well as the associated quantum-tunnelling, in which as a consequence, the hard-wall boundary conditions ($\boldsymbol{n} \bullet \boldsymbol{J} = 0$) are used on the metal surfaces as no electrons can escape from the metal. However, in SC-HDM [76] the electron spill-out effect is intrinsically considered. In SC-HDM, the calculation consists of two steps: the first step is the calculation of the

equilibrium (background) electron density with abrupt jellium distribution, while the second step deals with the calculation of the induced electron response as well as the optical filed.

The equation-of-motion of the electron gas can be written as:

$$mn\left(\frac{\partial \boldsymbol{v}}{\partial t}+\boldsymbol{v}\bullet\nabla\boldsymbol{v}\right)=-n\nabla\frac{\delta G}{\delta n}+ne\left(\boldsymbol{E}+\boldsymbol{v}\times\boldsymbol{B}\right) \tag{5. 17}$$

Where G is the internal energy of the electron gas, and it's assumed to be a function of the electron density. Here the density n satisfies the charge continuity equation:

$$\frac{\partial n}{\partial t}=-\nabla\bullet\left(n\boldsymbol{v}\right) \tag{5. 18}$$

In the linear response of the electrons gas region, we assume the induced electron density $n_1(\boldsymbol{r},t)$ is a small perturbation to the equilibrium density $n_0(\boldsymbol{r})$ as $n(\boldsymbol{r},t)=n_0(\boldsymbol{r})+n_1(\boldsymbol{r},t)$. Then we can get:

$$\left(\frac{\delta G}{\delta n}\right)_0+e\left(\phi_0+V_{back}\right)=\mu \tag{5. 19}$$

Here $\mu$ is the chemical potential, $\phi_0$ is the potential generated by the equilibrium electrons:

$$\nabla^2\phi_0=-\frac{en_0}{\varepsilon_0} \tag{5. 20}$$

$V_{back}$ is the potential generated by the jellium background with density $n^+$:

$$\nabla^2V_{back}=\frac{en^+}{\varepsilon_0} \tag{5. 21}$$

Finally we can get the equation that determines the equilibrium electron density.

$$\nabla^2\left(\frac{\delta G}{\delta n}\right)_0-\frac{e^2}{\varepsilon_0}n_0+\frac{e^2}{\varepsilon_0}n^+=0 \tag{5. 22}$$

The induced charge density can be written as:

$$i\omega\rho_1 = \frac{1}{\gamma - i\omega}\left[-\nabla\bullet\frac{\rho_0}{m}\nabla\left(\frac{\delta G}{\delta n}\right)_1 + \varepsilon_0 E_1\bullet\nabla\omega_p^2 + \omega_p^2\frac{\rho_1}{\varepsilon_r}\right] \quad (5.\ 23)$$

and the equation for the E&M field:

$$\nabla\times\nabla\times\boldsymbol{E}_1 = k_0^2\varepsilon_r\boldsymbol{E}_1 + \frac{i\omega\mu_0}{\gamma - i\omega}\left[-\frac{\rho_0}{m}\nabla\left(\frac{\delta G}{\delta n}\right)_1 + \omega_p^2\varepsilon_0\boldsymbol{E}_1\right] \quad (5.\ 24)$$

In our calculation, we solved eqs 20 in COMSOL Multiphysics to get the equilibrium electron density and for our planar system a homemade code with transfer matrix method was used to calculate the E&M field as well as the induced charges. In the transfer matrix calculation associated with electron spill-out, we divided our planar system into layers as thin as 0.001nm and solved E&M equation and the nonlocal response equation layer by layer using the equilibrium electron density profile obtained from the COMSOL simulation. The details of this transfer matrix method can be find in ref [82]. The internal energy function ($G$) of the electron gas typically has a very complicated expression with the contributions from various origins such as the Thomas-Fermi functional, von Weizsacker functional, exchange-correlation energy functional and so on[76]. But here in our calculation, only the Thomas-Fermi energy have been considered. Though the calculation cannot obtain the accurate electron profiles but it is sufficient to catch the main feature of the electron spill-out effect as well as the associated quantum tunneling. More details of the SC-HDM and the functional for the electron internal energy can be found in ref [76].

In our calculations, we applied a simple Drude model to describe the local permittivity of gold,

$$\varepsilon_m = \varepsilon_\infty - \frac{\omega_p^2}{\omega^2 + i\gamma\omega} \tag{5. 25}$$

with the parameters of: $\varepsilon_\infty = 1$, $\omega_p = 9.02eV$, $\gamma = 0.071eV$ [81], [86]. And for the nonlocal response, $v_F = 1.39\times10^6 ms^{-1}$ [81], [86], [84] with $\beta = \frac{3}{5}v_F$ has been used. For the GNOR model, $D = 1.90\times10^{-4} m^2 s^{-1}$ [81], [86] has been used.

## 5.3 Topological transitions

Based on the nonlocal Hydrodynamic model, we first study the hyperbolic metamaterial based on 1:1 $SiO_2$/Au multilayer with different size of unit-cell. When the thickness of both Au and $SiO_2$ layers are reduced and approaching zero while keeping the ratio of these two components, we can show clearly that there are topological transitions of the iso-frequency surfaces for both type I and type II HMMs regarding to those under local theory. For type II HMM, the iso-frequency surface transforms from a hyperbola to a bullet shape (Figure. 5.1c). While for type I HMM, more interestingly, the surface splits into two branches: a cylindrical-like branch at high k region and an elliptical branch at the low k region as shown in Figure. 5.1b. In both cases, high k states are restricted as compared with the dispersion relationship predicted by the ideal effective HMM medium.

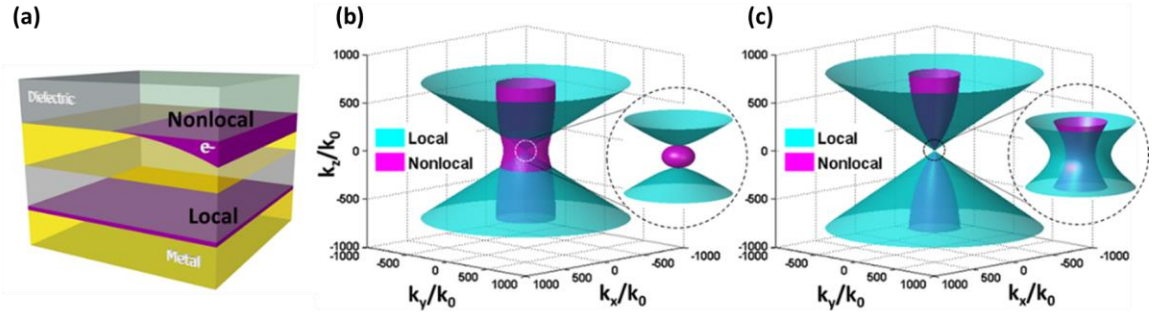


Figure 5.1: (a) Sketch of the HMM based on 1:1 Au/SiO2 bilayers. For a local response, the induced charge density reduces to a Dirac delta function at the metal surface. For nonlocal response, the induced charge density spreads out in the bulk region of the metal. Iso-frequency surfaces of type I (b) and type II (c) HMMs under the ultra-thin limit of the unit cell.

In order to see more clearly of the nonlocality induced topological transition process, we calculate the dispersion curves of type I HMM with the unit cell thickness changing from tens of nanometer to the ultrathin limit (Figure 5.2b). The local response theory (Figure 5.2a) predicts that the iso-frequency curve will infinitely approach a perfect hyperbola with decreasing unit cell thickness. While under nonlocal treatment the curve first evolves from a bounded hyperbolic-like shape to an unbounded hyperbola, but then pass through the local limit and finally degenerates to an elliptical-like shape as shown in Figure 5.2b. This hyperbola to ellipse transition of the iso-frequency surface indicate that the type I HMM will behave like a normal media when the building layers are approaching ultrathin limit instead of a perfect HMM as promised by conventional local theory.

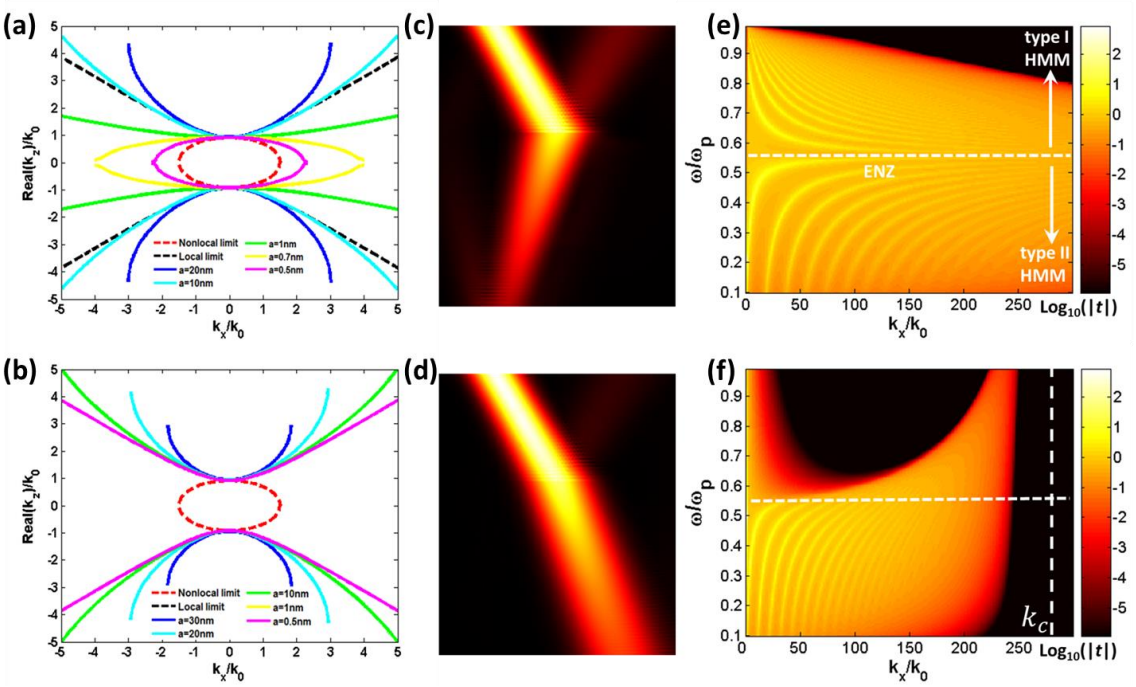


Figure 5.2: (a) and (b): Evolution of the iso-frequency curves of a type I HMM from thicker unit cells to ultrathin limit under (a) local and (b) nonlocal considerations. (c) and (d): Gaussian beam refraction at Air/HMM interface with type I HMM under ultrathin limit with (c) local and (d) nonlocal theory. The beam incidents at 30o. (e) and (f): Calculated magnitude (logarithmic scale) of the electromagnetic field transmission coefficient |t|, for a free-standing HMM stack composed of 6 bilayers of Au (0.1 nm) and SiO2 (0.1 nm), for (e) local (f) nonlocal case with TM mode.

As an example of the result of this topological transition, we show that the way of wave propagation inside this metamaterial is very different compared to the local theory's expectation. Here in the Figure 5.2c-d show the refraction phenomena at the Air/HMM interface with the incidence of Gaussian beams at 30 degree: negative refraction (Figure 5.2c); and normal refraction (Figure 5.2d) due to the different directions of group velocities determined by their iso-frequency surfaces of the metamaterial.

In order to verify these topological transitions, we also study a finite-size HMM based on 60 pairs of metal/dielectric multilayers with each layer 0.1nm thickness, where the metal is assumed to be Au and the dielectric assumed to be $SiO_2$. We plot the field transmission coefficient as the function of tangential *k* as shown in Figure. 5.2e and f. Such field transmission plot are widely used to demonstrate the photonic band information, plasmonic features and allowed normal modes in metamaterials[87], [88]. As according to the local theory, the allowed modes form a single band which can extend to ultrahigh *k* region for both type I (Figure. 5.2e upper space) and type II (Figure. 5.2e lower space) HMM. However when the non-local responses are taken into account, we can see clearly that for type I HMM the allowed modes form two bands: one at low k region and the other at high k region, which correspond to the two branches of the iso-frequency surface as shown in Figure. 5.1a. For type II HMM there is only one continuous band start from the low *k* region and extends to the high *k* region, which is also consistent with our finding. As an important feature, we can observe that both of them experience a cut off *k* value, which indicates that under nonlocal theory the allowed modes cannot extend to high *k* states indefinitely. Instead they will be limited by a cut-off *k* value that is determined by the Fermi velocity of the metal as we will show in the Methods section. These results clearly establish that the nonlocality induced topological transitions of the iso-frequency surface intrinsically and significantly change the optical properties of HMM for both low *k* and high *k* regions.

## 5.4 Local density of states and spontaneous emission

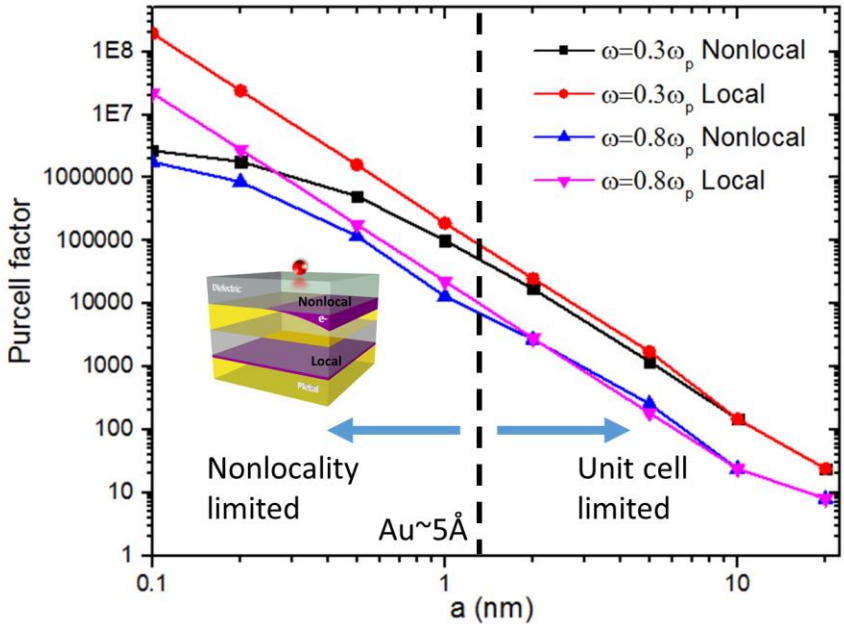


Figure 5.3: Purcell factor of a spontaneous emitter just above the HMM. The HMM is built with 1:1 SiO2/Au multilayers with fixed total thickness of 20nm and different unit-cell thickness from 20nm to 0.1nm.

As a direct result from the limitation of the allowed modes in *k* space, we also studied the spontaneous emission rate enhancement and local density of states of the HMM in the ultra-thin limit. Figure. 5.3 shows the Purcell factor of a spontaneous emitter placed just above a 1:1 $SiO_2$/Au multilayer HMM with the total thickness fixed as 20nm but with different unit-cell thickness from 20nm to 0.1nm under both local and nonlocal treatment. As is shown, under local theory the Purcell factor can approach infinity with decreasing unit cell thickness while for nonlocal case a finite saturation value exists. This saturation phenomena is a direct result of the limited LDOS due to the bounded high k modes. It is

yet another good example of limiting light concentration and plasmonic enhancement due to the nonlocality.

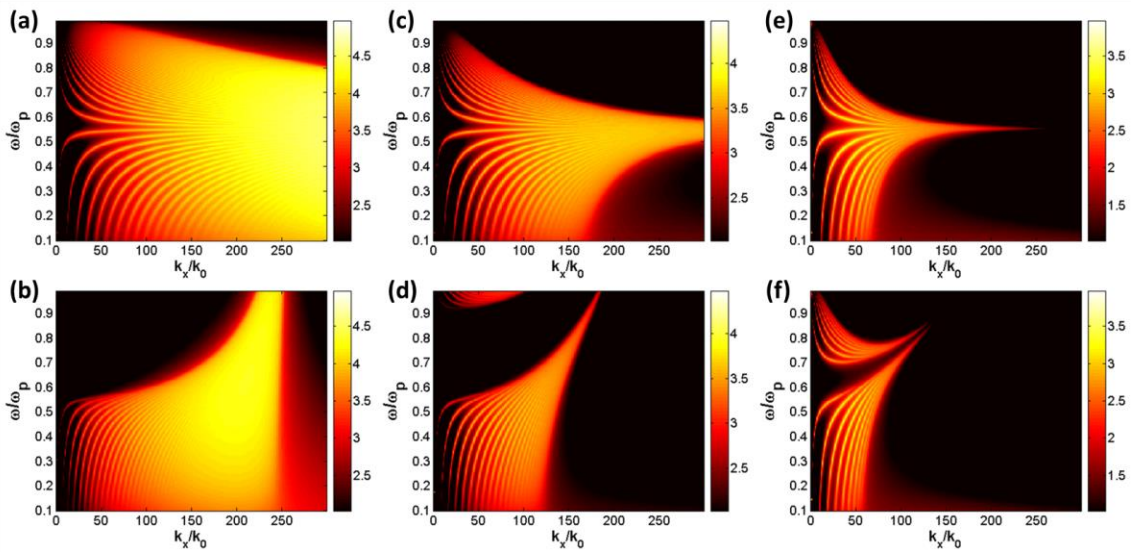


Figure 5.4: LDOS distribution for different HMM under local ((a), (c), (e)) and nonlocal ((b), (d), (f)) treatment. In (a) and (b), the unit-cell size is 0.2nm. In (c) and (d), the unit-cell size is 0.8nm. In (e) and (f), the unit-cell size is 2nm.

While we show the great diverge between the results expected by local and nonlocal theory but we should also notice that the nonlocal effect can make a considerable difference only when the metal layers are thinner than 5Å. For thicker metal layers the LDOS is still determined by the unit-cell thickness. For example when the Au film thickness is 1nm, though the LDOS distribution features show some difference (Figure. 5.4), but the "bright" areas are almost the same for the local and nonlocal cases. However for atomic layered structures (e.g. graphene) and naturally occurring HMMs such as graphite, the nonlocal effect should be considered, which will be discussed later.

## 5.5 Optical properties and electron response of a monolayer metal film

In order to get a better understanding of the underlying physics of these particular phenomena induced by nonlocality, we conduct further study on the optical behavior and electron response of a monolayer metal film. Figure. 5.5a and b show the reflectance of a 0.1nm and 1nm free standing Au film with incident light at different angle.

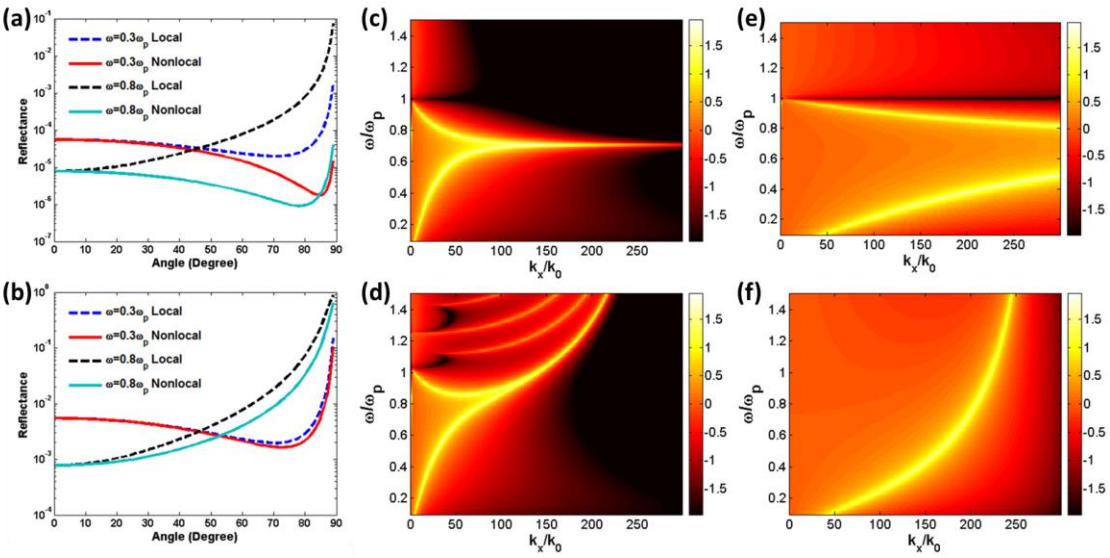


Figure 5.5: (a) and (b): Reflectance of a monolayer Au films with the thickness of (a) 0.1nm and (b) 1nm. (c) and (d): transmitted field coefficient of 1nm Au film under (c) local and (d) nonlocal treatment. (e) and (f): transmitted field coefficient of 0.1nm Au film under (e) local and (f) nonlocal treatment.

As is shown in the figures, the reflectance under nonlocal treatment drops significantly for ultrathin film compared to the local case, while for the thicker one (1nm), only tiny difference exists. However, for the plasmonic behaviors as shown in the transmitted field diagrams (Figure 5.5c-f), the difference at high *k* region is very obvious even for 1nm metal

film. More interestingly, the limitation to the wavenumber *k* are also observed even for monolayer film, which indicates that the observed limit of the high *k* mode as well as LDOS for HMM should be attributed to the intrinsic plasmonic limitation of a single film.

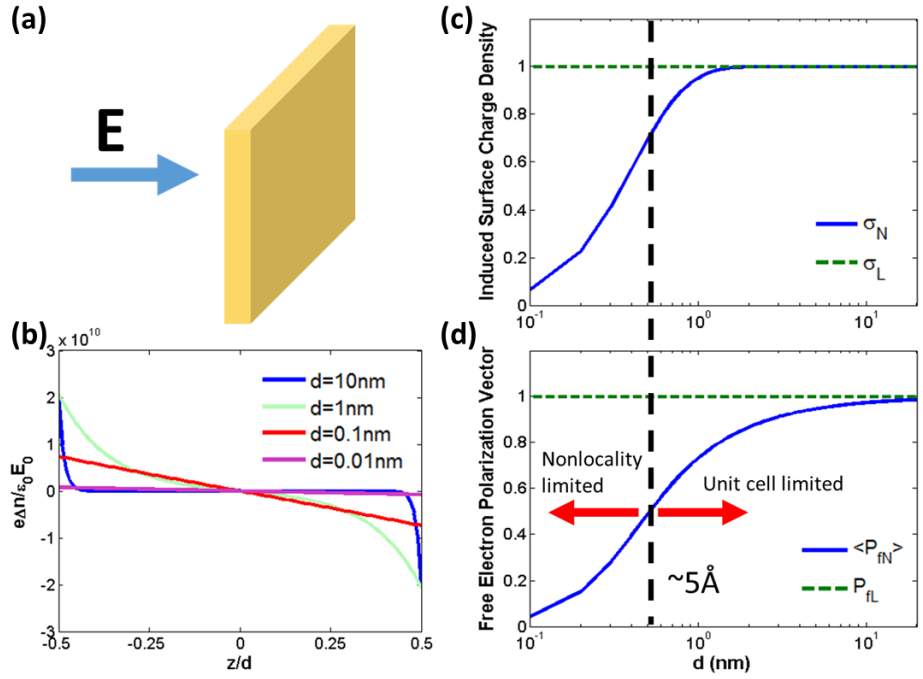


Figure 5.6: (a) Sketch of a free standing Au film put in an oscillating E field. (b) induced charge distribution inside the metal film. The induced charge density is normalized with the applied field. (c and d) induced surface charge density (c) and average free electron polarization vector (d) of gold films with different thickness. Blue solid lines: nonlocal case. Green dash lines: local case.

A further study relates these phenomena and results to the electron response in metal film under nonlocal consideration. Here we consider the case of a gold monolayer in an oscillation E field with the field vector perpendicular to the film surface. As we know, according to the local theory, the induced electron density distribution should exhibit a delta function at the surface. While under nonlocal response framework, the induced charge will spread over a distance inside the metal as established by the Hydrodynamic model,

due to the consideration of the electron pressure. Figure 5.6b shows the induced charge distribution inside the metal film normalized to the applied field. As the metal film gets thinner, the induced charge density becomes lower as well. Because of this decrease of the induced charge, the total induced surface charge density and the average free electron polarization vector becomes weaker and weaker when decreasing the metal film, while under local theory these values will maintain the same regardless of the thickness change. This means that less electrons can response to the applied field and at ultrathin limit, the metal films will eventually behave more like a dielectric layer without any free electron response. Based on these observations, it is easy to understand why the topological transition under ultrathin limit takes place, and why the HMM will transform to a normal media in low k region. All those findings are the consequence of the reduced electron response in an ultrathin metal film.

## 5.6 Surface plasmon and bulk plasmon in nonlocal metal

Another interesting result of the nonlocal electron response is that not only for thin metal film but even for a bulk metal, there is a limit to the wavenumber *k* of the plasmonic mode. Figure 5.7a shows the dispersion of the surface plasmon polaritons at Au/Air and Au/$SiO_2$ interface under local and nonlocal theory respectively. Unlike the SPP mode expected by the local theory which can be supported only in the low frequency region below $\omega_p / \sqrt{1+\varepsilon_d}$ and can be extended to ultrahigh *k* region at resonance frequency, in the nonlocal case the SPP mode can extend to ultrahigh frequency region even beyond plasma frequency in which the metal's dielectric permittivity becomes positive ( $\varepsilon_m > 0$ ).

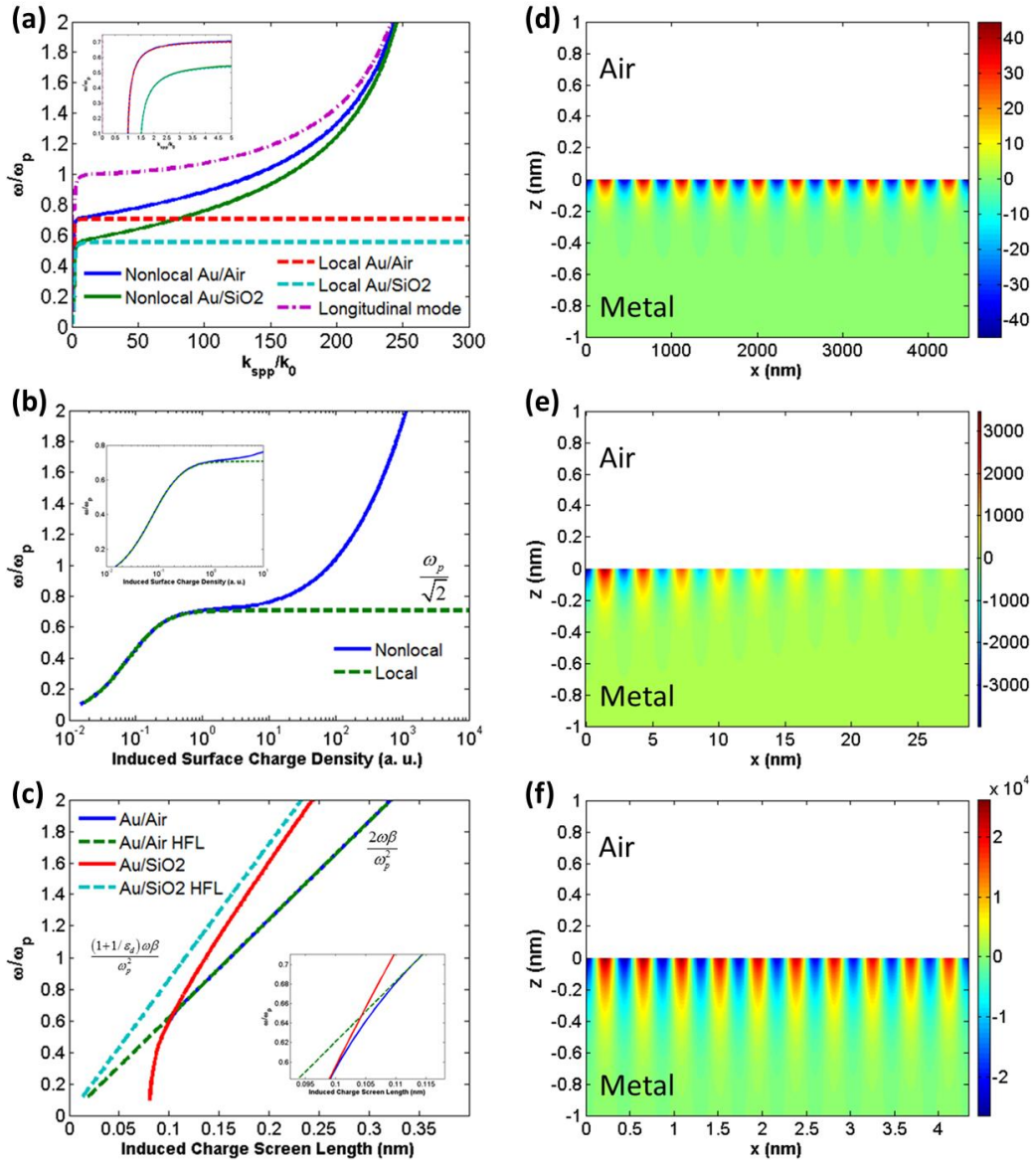


Figure 5.7: Surface plasmon response at gold-dielectrics interface. (a) Dispersion of surface plasmon polaritons at Au/Air and Au/$SiO_2$ interface under local or nonlocal treatment. (b) Induced surface charge density. Here the charges are not located in an ideal surface, so the induced surface charge density here represents the total induced charges per area. (c) Induced charge screen length. HFL stands for high frequency limit and the screen length increase linearly with the frequency $\sim (1+1/\varepsilon_d)\omega\beta/\omega_p^2$. For (a)~(c), the insert charts show the zoom in view of the low frequency region. (d)~(f): Induced oscillating charge distribution inside Au under 0.3, 0.8 and 1.5 $\omega_p$ with nonlocal effect. The color bars have different scale for these three cases.

Moreover, in the high frequency and high *k* region, both the dispersions of SPP at Au/Air interface and Au/$SiO_2$ interface converge to the dispersion curve of the longitudinal mode (bulk plasmon mode) in the bulk metal and experience the same limitation of the *k* value. These results indicate that at high frequency and high *k* region the SPP modes at metal/dielectric interface are gradually coupled into the longitudinal mode of the metal itself which is independent of the dielectric properties. Figure 5.7a-c show the transition process in views of polaritons dispersion, the total amount of induced charges per area and the distribution screen length of the charges. As we can see, in the low frequency region below $\omega_p / \sqrt{1+\varepsilon_d}$ , the dispersion curve or the total induced charges are almost identical in both local and nonlocal cases. The only difference is that the charges distribute in a very thin layer thinner than 1Å instead of perfectly confined in the metal surface. While when the frequency is increasing even exceeding the SPP resonance frequency defined in the local case, when considering the nonlocal response, both the total induced charges or the distribution screen length increase rapidly, which indicates more free electrons deeper from the bulk region are involved in the plasmon oscillation (Figure 5.7d-f). These results clearly explained the topological transitions and LDOS limitations in the high *k* region by attributing them to the intrinsic properties of the bulk plasmon in the metal and the frequency related transition from highly confined surface plasmon to the bulk plasmon.

## 5.7 Effects of electron diffusion kinetics

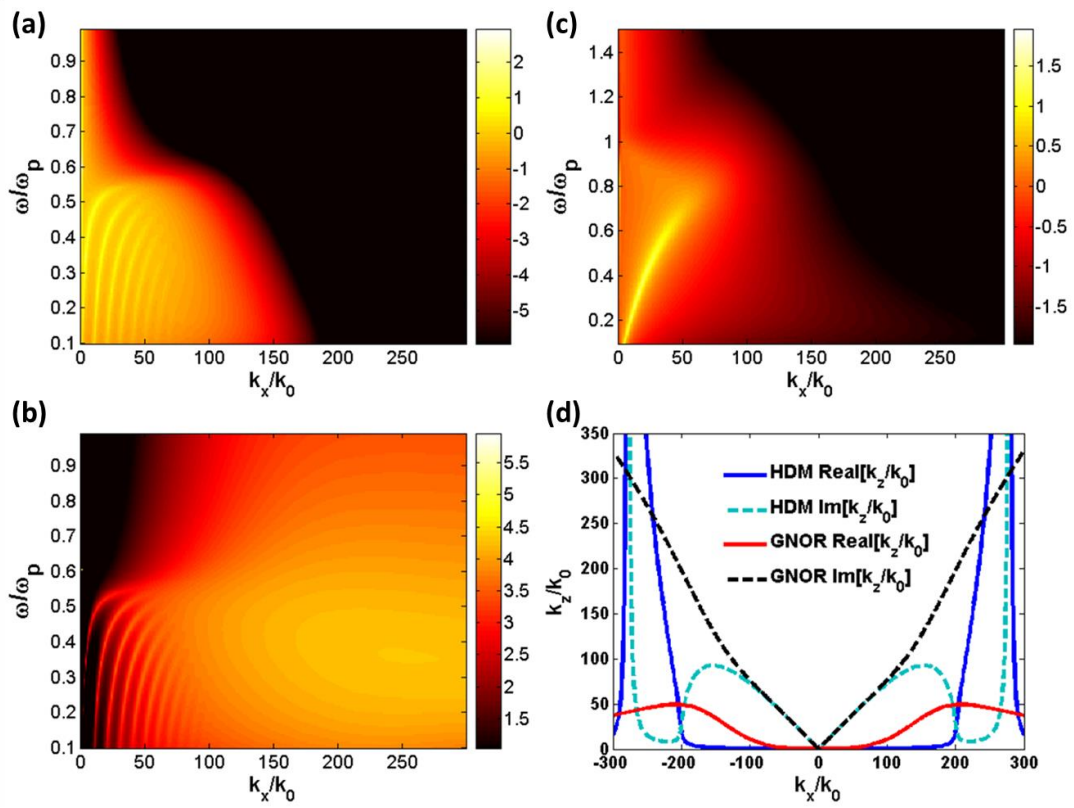


Figure 5.8: GNOR results for HMM based on 60 period 0.2nm 1:1 SiO2/Au multilayers for (a) transmitted field (b) LDOS distribution (d) dispersion. (c) transmitted field for a 1nm Au free standing film. For (d), the frequency is 0.8ωp for this case.

All the results discussed above are based on the traditional Hydrodynamic model in which only the electron-electron interaction induced nonlocal correction were considered. Actually other factors such as electron diffusion and electron spill-out effects as well as tunneling may have equal significance in these processes and have been studied in some very resent works[75], [76], [82]. Though in this work we mainly focus on the traditional HDM, we also investigate the influences of these factors on the performance of HMM.

Here we use the newly developed general nonlocal optical response model (GNOR)[75] to investigate the influence of electron diffusion effects; and later we will show the discussion about the spill-out effect studied by using recently developed self-consistent hydrodynamic model (SC-HDM)[76]. The general formulism of these models are described in the Methods section.

Figure. 5.8 shows the results based on the GNOR model. In general the electron diffusion effect create more loss to the material which eliminates the high *k* modes even allowed in HDM according to the transmitted field diagrams for both HMM based on multilayers (Figure 5.8a) and monolayer film (Figure 5.8c). We can see clearly it eliminates the high k branches of type I HMM and set a more aggressive limit to the wavenumber *k*. While if we look at the LDOS distribution of an emitter on this HMM, more interestingly, it seems that the emitter can emit photons into ultrahigh *k* modes even beyond the cut-off *k* as demonstrated in HDM. A further study on the dispersion of this HMM uncovers this puzzle by showing that the electron diffusion kinetics indeed help to extend the modes to a higher *k* region however these modes have high losses as shown in Figure 5.8d. These high loss modes can indeed make contribution to the LDOS and enhance the spontaneous rate, but photon emitted into those modes will have ultrashort life time and be dissipated very quickly. So in general, the effect of electron diffusion kinetics can change the topology of the iso-frequceny surface by creating high loss modes which can extend to much higher *k* region.

## 5.8 Effects of electron spill-out and tunneling

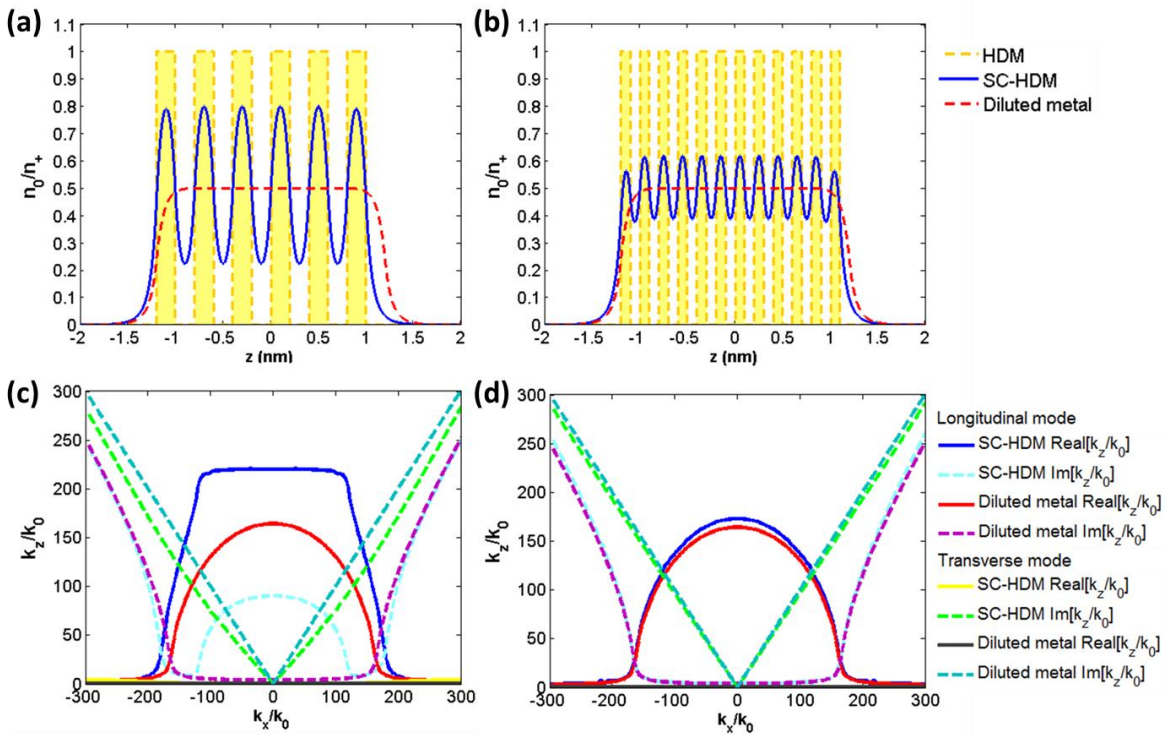


Figure 5.9: (a) and (b): equilibrium electron density profile for HMM based on 6 period 0.2nmAu/0.2nmAir multilayers and 12 period 0.1nmAu/0.1nmAir multilayers respectively. The electron density profiles are normalized by the jellium density in the metal. (c) and (d): optical eigen modes inside the HMM based on 6 period 0.2nmAu/0.2nmAir multilayers and 12 period 0.1nmAu/0.1nmAir multilayers respectively. The frequency is $0.8\omega_p$ for this case.

In line with the local-response Drude model, the standard implementation of the HDM usually considers the so-called hard-wall boundary condition that implies that the electrons are strictly confined in the metallic structure, with a uniform equilibrium density and without spill-out in free space. In SC-HDM however, the spill-out effects as well as tunneling effects are taken into consideration. In SC-HDM, the calculation consists of two steps: the first step is the calculation of the equilibrium (background) electron density with abrupt jellium distribution, while the second step deals with the calculation of the induced

electron response as well as the optical filed. Details of the method can be found in the Methods section. Here we study two 1:1 Au/Air multilayered metamaterials with the same total thickness of 2.4nm but with different unit-cell thickness as shown in Figure 5.9a: 6 pairs of 0.2nmAu/0.2nmAir and Figure 5.9b: 12 pairs of 0.1nmAu/0.1nmAir. As we can see from Figure 5.9a and b, under SC-HDM the equilibrium electron density profiles are smooth and continuous throughout the whole systems, quite different from those sharp and abrupt features obtained in the traditional HDM case. In order to investigate the optical performance of these metamaterils, we calculate the eigen modes inside these metamaterials at the frequency of $0.8\omega_p$ which typically correspond to type I HMM. However, as shown in Figure 5.9c and d the iso-frequency curves show neither hyperbolic nor two-brunches features as expected by local theory or traditional HDM, especially for the case of 12 pairs of 0.1nmAu/0.1nmAir multilayers. More interestingly, if we plot the eigen modes of a diluted metal with the jellium density 1/2 of that in the metal, the 12 pairs of 0.1nmAu/0.1nmAir multilayers case fits very well with the diluted metal case for both transverse mode and longitudinal mode (Figure 5.9d). For the case of 6 pairs of 0.2nmAu/0.2nmAir multilayers, the eigen modes also show similar features as the those in diluted metal case but it is also very obvious that it has not fully degenerated to the diluted metal case, especially for the low loss brunch around $100k_0$ to $150k_0$ which may correspond to the residue of the high $k$ brunch observed in HDM case. These results are not difficult to understand because when the unit-cell gets thinner and thinner, the equilibrium electron density levels between the metal regions and the air regions get closer and closer and at ultrathin limit, the material will just behave like a diluted metal with uniformly distributed

electron density. In that case, neither the high k mode promised in local theory nor the high k brunch observed in HDM will exist, which indicates the electron spill-out or tunneling effect can change the picture drastically as the boundary between the metal and dielectric becomes blurred and the material behaves more like a diluted metal. This may explain why graphite cannot be considered as a naturally occurring HMM in most of the frequency range, despite of atomically thin layers (graphene) separated by very thin (~0.335nm) dielectric layers (vacuum).

## 5.9 Connection to real materials

All the results discussed above are focusing on ultrathin ideal Drude metal with the consideration of the quantum effects of the free electrons. As we showed that the nonlocality induced effects can be considerable only when the thickness of the metal is below 5Å, which is not real concern for deposited metals in current experimental conditions. However, those effects should be important factors to consider for some naturally materials with atomic level thickness such as graphene and naturally occurring HMMs made of 2D materials. Here in this section, we will connect our findings to such materials such as graphene.

Figure 5.10a and b show the plasmon polaritons dispersion of graphene on glass calculated by the random phase approximation method (RPA) [89]–[91] and a simple 2D free electron gas model based on local theory[89]. We can see clearly that the RPA model and the classical local theory expect very different pictures of the plasmon behaviors: under local theory the plamonic mode can extended to ultrahigh $k$ while under RPA, the dispersion

experiences the same limited *k* value as we observed for the nonlocal metal thin film. The reason for that is the RPA method intrinsically involves the Fermi statistics of the electrons as well as the electron-electron interactions. And this high *k* limitation is an intrinsic result from the plasmon property of graphene. Very recently, an around $300k_0$ wavenumber cut-off was also expected for graphene ribbon based hyperbolic metasurfaces[92], [93].

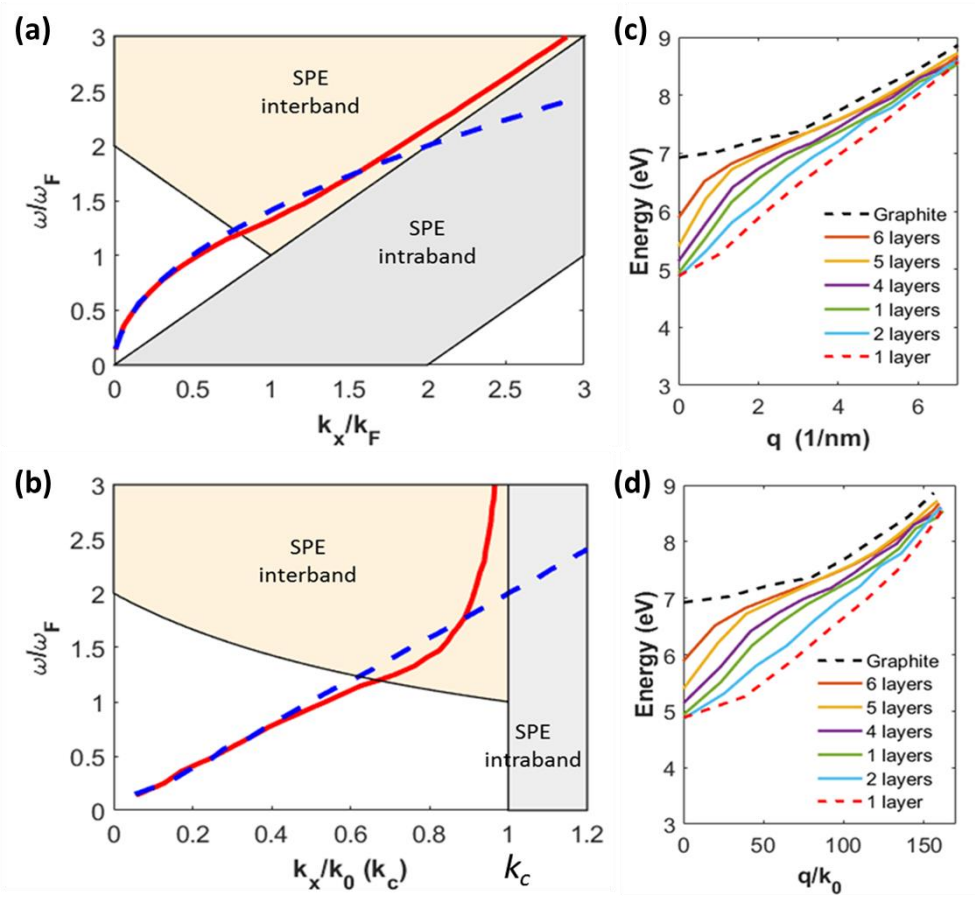


Figure 5.10: (a) and (b) Plasmon mode dispersion in 2D graphene (solid red line) calculated within RPA. The dashed blue line indicates the local long-wavelength plasmon dispersion based on classical local method. The black solid lines represent the boundaries of the single-particle excitation (SPE) Landau damping regime for intra- and interband electron-hole excitations. (a) the k value is normalized as $k_F$, (b) the k value is normalized as k0 in unit of . Here . (c) and (d): Experimental measured dispersion of the π plasmon for one to six graphene layers based on momentum-resolved electron energy-loss spectroscopy (EELS) compared and graphite. In (d), the momentum q is normalized to k0. The data of (a) and (b) are adapted from ref [89] and (c) and (d) are from ref [94].

Another interesting thing we should notice is that though the dispersion curve showed the allowed high $k$ mode can be extended to ultrahigh frequency approaching the cut-off $k$ value, the single-particle excitation (SPE) Landau damping from intra- and interband electron-hole excitations will dramatically increase the loss of those modes and thus make them very hard to be observed in experiments[95], [96]. This result shares the same conclusion we obtained from the GNOR model by considering the electron diffusion kinetics as these effects will turn the allowed high $k$ modes into high loss modes. Though the Landau damping and the electron diffusion kinetics have very different physical nature, the GNOR model itself is far more powerful by boiling down the underlying complex physics of all kind of interactions into a phenomenological parameter - the diffusion constant $D$. In this case, the damping from other origins can also be applied in the GNOR model. Actually, a recent work [97] already studied the Landau damping near the surface of plasmonic nanoparticles by using this method. Thus it is not very difficult to understand why we also observed very similar damping phenomena, and also very similar cutoff line of the high $k$ and high frequency modes in our system as compared to the graphene plasmon by comparing Figure 5.8a, c with Figure 5.10b. These results show that these semi-classical models can indeed provide fruitful physics insight and shed light on the behavior of these low-dimensional materials.

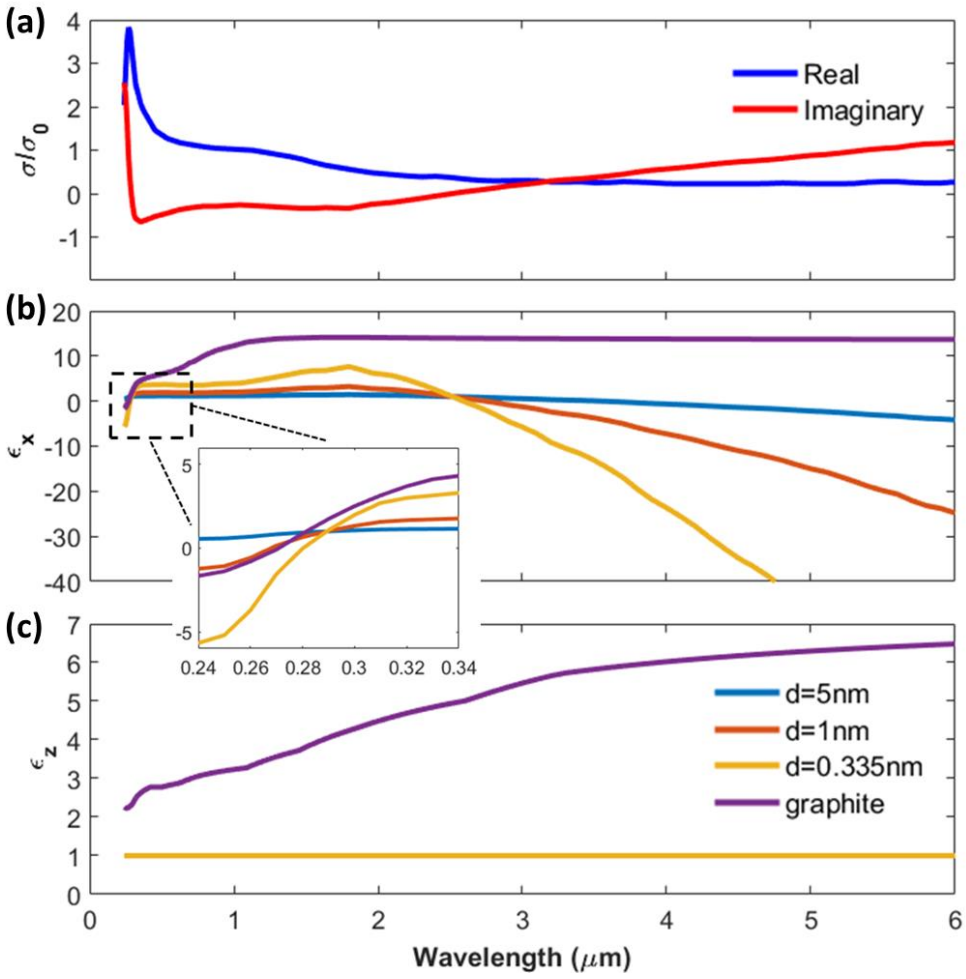


Figure 5.11: Metamaterials based on graphene/Air multilayers compare to graphite. (a) measured conductivity of monolayer graphene from ellipsometry[98]. (b) and (c): permittivity of the graphene/air metamaterials compared to graphite with different separation distance (d). d=0.335nm case represents a "fake" graphite. The graphite permittivity are adapted from ref [99]. The insert chart shows zoom in view of the permittivity at high frequency region (240nm-340nm).

Besides monolayer graphene, it's also of great interest to check HMM based on graphene multilayers and some natural HMM like graphite. When increasing the number of layers of graphene, multiple plamonic modes will exist and finally form a continuous band instead of a single plasmonic mode in monolayer graphene[100], [101], [94]. Figure. 5.10c and d

show the measured dispersion of the π plasmon for graphene multilayers based on momentum-resolved electron energy-loss spectroscopy (EELS) from ref [94]. As we can see clearly here, not only for the monolayer graphene, but also for the other multilayers graphene as well as graphite, their plasmon dispersion curves converse to an almost linear dispersion in the high *k* and high frequency region (Figure. 5.10c). That means they all will experience a same cutoff *k* value when normalized to $k_0$ (Figure. 5.10d). These experimental results agree very well with our predictions in typical nonlocal metal system, which provide strong evidence that the intrinsic bulk plasmon of the material itself will dominate the plamonic properties in high *k* region no matter the thickness of the film.

Here we also compared the permittivity of a "fake" graphite by considering a graphene/Air multilayer metamaterial with the real graphite in Figure. 10. The conductivity of monolayer graphene was adapted from ref [98], in which a CVD graphene was measured by ellipsometry. The effective permittivity of the graphene HMM are obtained by following the methods based on transfer matrix as established in ref [102]–[104]. For the "fake" graphite case, we just set the separation between graphene layers as 0.335nm, mimicking a real graphite structure. The graphite permittivity is adapted from ref [99]. As shown in Figure 5.11b and c, both the graphene metamaterials and the graphite show one band of hyperbolic type ( $\varepsilon_x \bullet \varepsilon_z < 0$ ) in UV range (~below 280nm). However the graphene metamaterials show another hyperbolic band starting from mid-IR (~2.5um), while the graphite is always a dielectrics in this region. Actually three hyperbolic bands of graphite are reported: two narrow bands in UV range[99], [105], [106], and a broad band in far

inferred (20um~60um)[107]. It's interesting to notice that when the separation thickness between graphene layers decrease, in principle the tangential permittivity should be more negative as increasing the metal filling ratio, but actually in the extreme case of a real graphene, the permittivity turns out to be positive and only be negative again at much larger wavelength. One possible reason for that may be the effect of electron spill-out. As we demonstrated above, once the metal films get close the electrons will spill out and fill all the regions. In this case, the electron density is much diluted compared with that in the metal film itself, which leads to a much lower plasma frequency and shifting the hyperbolic band to much longer wavelength range. This may be one possible explanation, and a more comprehensive understanding may require the analysis of the electron band structures.

## 5.10 Conclusions

Based on hydrodynamic model of electron response, we have shown that the nonlocal effect originated from the electron-electron interactions will induce the topological transitions of the iso-frequency surface and intrinsically limits the wavenumber as well as LDOS for both type I and type II HMMs. They are due to the reduced electron response induced by electron-electron interactions. At ultrathin limit, the ability of finite density of electrons to screen the electric field is significantly reduced, as a result the metals behave more like a dielectrics. These results indicate that in the aim of achieving high performance HMMs, merely thinning the constituent films according to the local theories is no longer valid. However, we also showed that the nonlocality induced effects can be considerable

only when the thickness of the metal is below 5Å, which is not real concern for deposited metals but should be an important factor to consider for graphene and naturally occurring HMMs made of 2D materials. In addition, by taking into account other effects beyond HDM, we found that the effect of electron diffusion kinetics can definitely change the topology of the iso-frequceny surface by rendering the high *k* brunch into high loss modes, while the spill-out effect can also change the iso-frequency surface and finally turn the HMM into a diluted metal under the ultrathin limit. Thus we show clearly that these effects can also provide significant influence upon the performance of HMM and a more sophisticated model with consideration of all these factors are highly desired.

# Chapter 6

# Surface Plasmon-Coupled Light Emission Based on Metal/Dielectrics Multilayer

## 6.1 Introduction

Two-dimensional (2D) materials, especially monolayers of transition metal dichalcogenides (TMDCs) are crystalline materials comprising only a single layer of atoms. They are direct bandgap two-dimensional (2D) material semiconductors and show dramatically properties different from the bulk materials, making them promising light active materials for optoelectronic applications[108]. Recently, TMDCs have shown great potential in ultrafast and ultrasensitive photodetectors and as ultrathin light absorbers and emitters[109], [110]. However, their application in photonic devices is limited by their low absolute photoluminescence (PL) caused by low quantum efficiency and weak absorption[111]. Thus, a lot of effort have been made towards achieving enhanced light emission from TMDCs[112]–[117].

Plasmonic systems are widely used to enhance light emission from active materials. And significant enhancement is also reported by integrating 2D materials with noble metal nanostructures such as nanoparticles, nanowires and nanotrenches[112] supporting localized surface plasmons[113]–[115] and propagating surface plasmon polaritons

(SPPs)[116], [117]. However, several intrinsic issues may arise when integrating 2D materials with these plasmonic nanostructures. First, the direct deposition of metallic nanostructures on 2D materials often results in unavoidable damage[118]. In addition, direct contact between metal and a 2D materials may induce charge transfer as well as associated exciton loss and extra electron/hole doping[119]. Furthermore, because the strong EM resonance exists only in the tiny gaps between adjacent metallic nanostructures, only a small area of 2D materials would experience strong light–matter interactions, which intrinsically limits the efficiency of utilizing the whole light active layer. Thus a novel system avoiding these issues are highly desired.

In addition, a simple system integrating 2D materials and plasmonic structures provide a perfect platform to study the fundamental physics of the exciton relaxation kinetics in a light-emitting system. For example, surface plasmon can active manipulate the exciton relation kinetics by providing new photonic states (SP states) as new relaxation pathways. That's how surface plasmon associated Purcell effects come into being. As 2D materials are just one atomic thick, it's a perfect probe to investigate the local E&M filed, photonic local density of states and local exciton energy transfer rate in the spatial accuracy which is hard to achieve by other light active materials. Thus the understanding of the underlying physics of the 2D materials-surface plasmon interacting systems may shed light on other similar light-emitting systems with other active materials such as OLED and photodetectors.

Here in this work, we report our finding of enhanced light emission from TMDC (WeS2) by using simple, deep subwavelength, 3 layers dielectics/metal/dielectrics (DMD) structures. The enhancement is extremely sensitive to the dielectrics layer separating the 2D materials and the metal film in the level of several nanometer. Distinct from previous plasmon-enhanced structures[112]–[117] our system is purely planar, much simpler but provide more powerful platform to study the fundamental physics of exciton dynamics when interacting with surface plasmon.

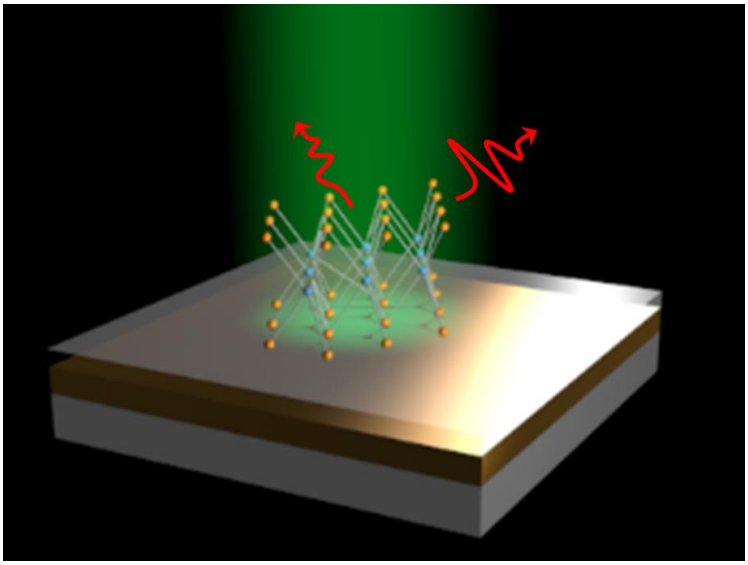

Figure 6.1: Schematic drawing of the system.

## 6.2 Methods and materials

Our planar dielectrics/metal/dielectrics (DMD) structure consist with glass substrate, 40nm Au film and one SiO2 spacer (5nm-25nm) layer separating the metal film and the WSe2 monolayer as in shown in Figure 6.1. The glass substrates were cleaned by acetone cleaning

and piranha cleaning (H2O2: H2SO4 = 1:1) for 30 mins, and then DI water cleaning before deposition. The Au films (40nm) were deposited via evaporation with a rate of 1.31~1.38 A/s. In order to investigate the separation dependence, SiO2 spacer layer with different thickness were deposited on to the Au films via PECVD with rate of 6.4~6.7 A/s. The thickness and deposition rate were calibrated on cleaned Si samples via ellipsometer. WSe2 (2D Semiconductors) samples were exfoliated mechanically using adhesive Scotch tape and then transferred onto PDMS substrates first and then transfer to the DMD samples.

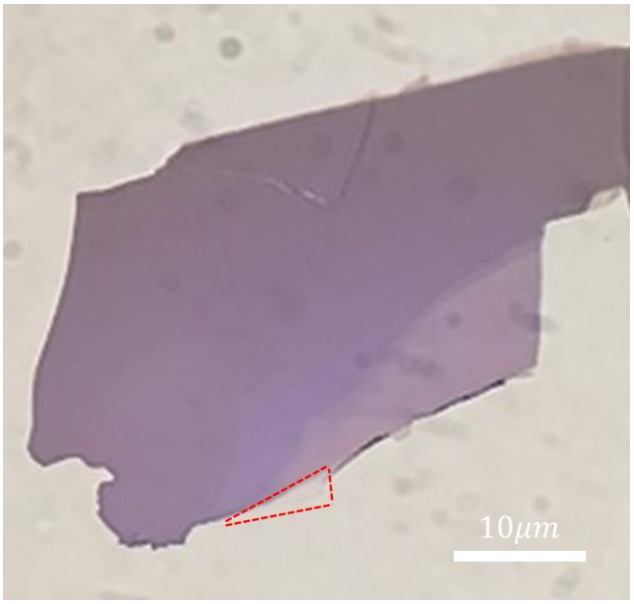


Figure 6.2: Optical microscopy image of exfoliated WSe2 flakes. The red triangle marks the region of monolayer WSe2.

PL measurements were performed using a home-made micro-PL system by modifying florescent microscope () equipped with an excitation laser operated at a wavelength of 532 nm. A laser power of 30uW with a focus spot of 10um (focused by a 40X objective lens) on the sample. A spectrometer (Andor 550i) were used to detect the PL signal with

integration time of 20s. All the measurement conditions were kept same for all the samples except special noticing.

## 6.3 PL Enhancement

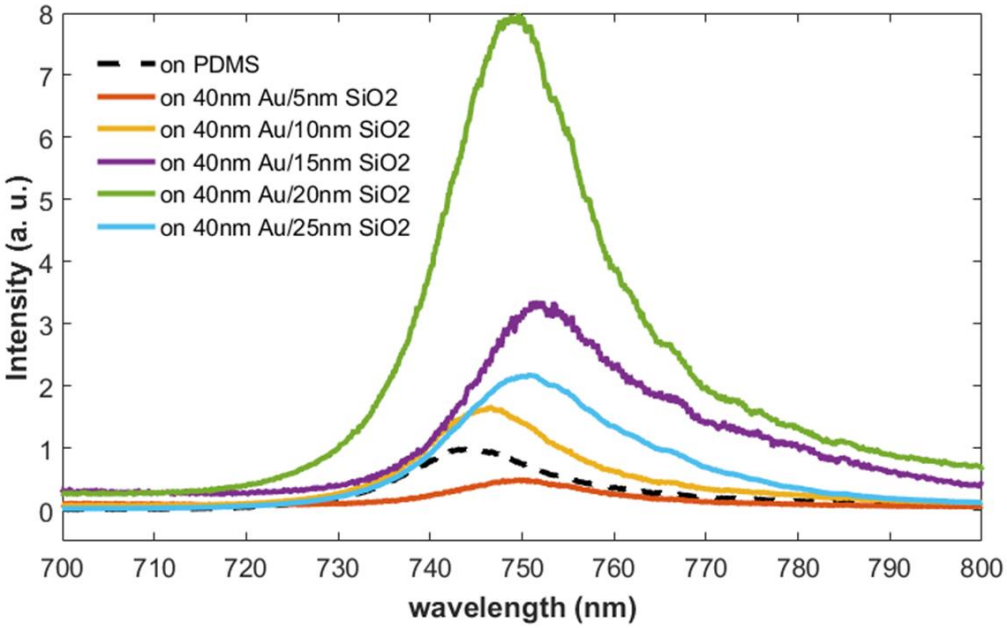


Figure 6.3: Measured PL spectra of exfoliated monolayer WSe2 flakes on SiO2/Au/Glass DMD structures with the SiO2 spacer layer range from 5nm to 25nm. The spectra are normalized to the peak value of the case of WSe2 directly on PDMS.

In order to investigate the separation dependence, DMD structures with SiO2 spacers of different thickness were tested. Here Figure 6.3 shows the measured PL spectra of WSe2 monolayers on SiO2/Au/Glass DMD structures with the SiO2 spacer layers ranging from 5nm to 25nm. As we can see from the plot, either enhancement or inhibition have been observed when the 2D materials are interacting with the DMD structures. And considerable

shifts of the spectra peak were also observed. Both of the enhancement and shift show dramatically sensitive dependency on the thickness of the spacer layer even changing in step of only 5nm.

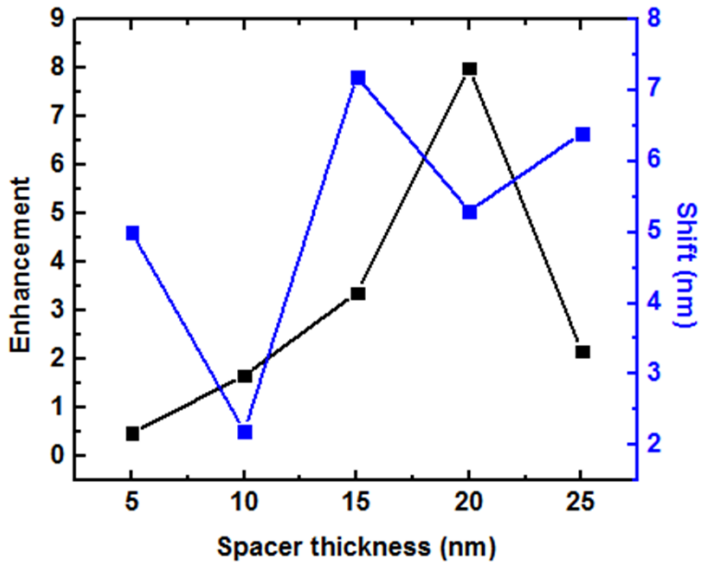


Figure 6.4: Enhancement factor and spectrum shift of the PL peak of monolayer WSe2 flakes on SiO2/Au/Glass DMD structures with the SiO2 spacer layer range from 5nm to 25nm. All the enhancement and shift are compared with WSe2 on PDMS.

Figure 6.4 summarizes the enhancement and shift of the spectra peaks compared to the case of WSe2 monolayers on pure PDMS substrate. Only the sample with 5nm spacer layer shows a inhibition of the PL signal, which can be easily understood with optical quenching of a metal surface when emitters are too close to it. For all of the others, obvious enhancement have been observed and an optimized case have been obtained when the spacer layer is 20nm in which the enhancement is as high as 8 times compared with the case on pure PDMS substrate. More interestingly, very rapid increase (from 3.5 to 8 for

thickness changing from 15nm to 20nm) and decrease (from 8 to 2.5 for thickness changing from 20nm to 25nm) near the optimized thickness have been observed, which makes the optimized case looks like the outcome of matching some kind of resonance conditions. This rapid distance dependence cannot be explained with conventional interference theory or considering any resonance relay on wave interference as the change is so tiny and subwavelength, which leads to very trivial change of the phase or optical path. As the structures are purely planar without out any scattering and the pumping laser beam incident from air, there is no obvious reason of exciting localized or propagating surface plasmon from the pumping laser as widely used and established in some previous works[112]–[117]. More detailed discussions about the mechanism will be conducted in the Discussions section.

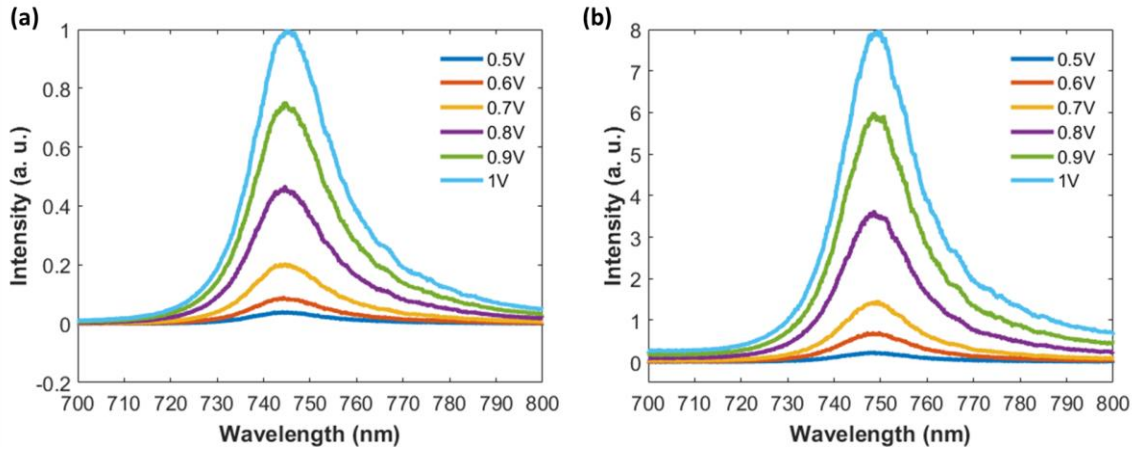


Figure 6.5: Laser power dependence of the measured PL signal of monolayer $WSe_2$ PDMS compared with that on DMD structure with 20nm $SiO_2$ spacer and 40nm Au film. (a) $WSe_2$ on PDMS. (b) $WSe_2$ on DMD structure.

Table 6.1: Calibrated laser power and enhancement factor for monolayer WSe2 on DMD structure with 20nm SiO2 spacer and 40nm Au film under different laser power. All the peak intensities are normalized to the case of WSe2 on PDMS with laser voltage of 1V.

| Laser Voltage [V] | 0.5 | 0.6 | 0.7 | 0.8 | 0.9 | 1.0 |
|---|---|---|---|---|---|---|
| Laser Power [μW] | 0.83 | 2.50 | 5.62 | 14.02 | 22.40 | 30.44 |
| Peak Intensity on PDMS | 0.034 | 0.088 | 0.201 | 0.46 | 0.752 | 1.0 |
| Peak Intensity on DMD | 0.216 | 0.676 | 1.47 | 3.61 | 5.91 | 7.92 |
| Enhancement Factor | 6.35 | 7.68 | 7.31 | 7.85 | 7.86 | 7.92 |

We also tested the laser power dependence of these enhancement and shift. Figure 6.5 and Table 6.1 summarized the measured PL spectra and enhancement of the optimized sample with 20nm SiO2 spacer and 40nm Au film with different pumping power. As we can see from Table 6.1, both the peak intensity of WSe2 monolayers on PDMS and on optimized DMD structures show linear dependence with laser power. And the enhancement factors at different laser power are close to each other regardless the acceptable small variations. (The big variation of the case of 0.5V may result from the weak signal of WSe2 on PDMS under such low pumping power). These results indicate that this enhancement is a linear process with power and may not due to any nonlinear or many-body coherency (e.g. super-radiance [120]) effect in which typically a nonlinear power dependency are usually observed.

## 6.4 Distance dependent light-emission in OLED devices

More interestingly, we also observed similar separation distance dependent light-emission phenomena in multilayer based OLED systems even with electroluminescence (EL) measurement. Figure 6.6 shows the EL characterization of OLED devices with structure of

ITO (130 nm)/ZnO(15 nm)/PEIE(20 nm)/Super yellow(70nm)/MoO3 (0,1,5,10,15 nm)/Ag (100 nm). As we can imaging here, the MoO3 layer which separates the light-emission layer (Super yellow) and the metal layer (Ag reflector) might work as the spacer like the SiO2 spacer in our previous 2D materials-DMD system.

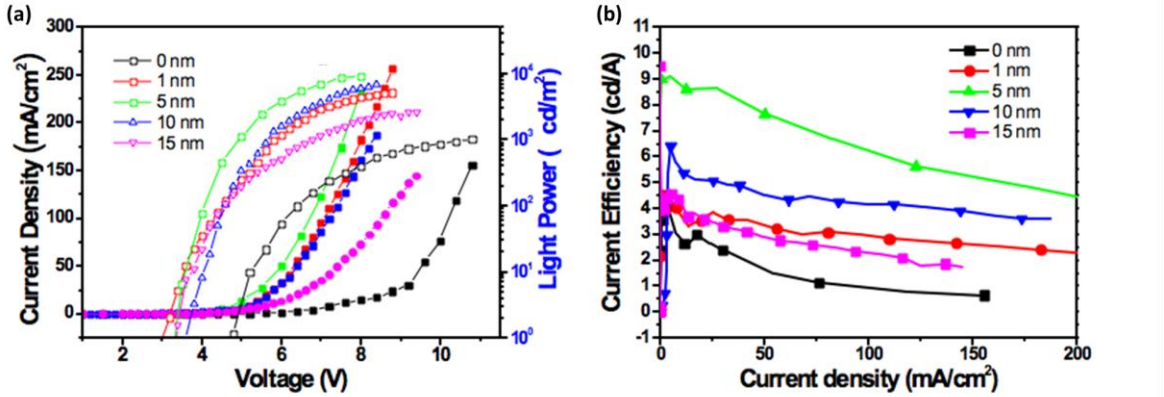


Figure 6.6: EL characterization of OLED devices with structure of ITO (130 nm)/ZnO(15 nm)/PEIE(20 nm)/Super yellow(70nm)/ MoO3 (0,1,5,10,15 nm)/Ag (100 nm). (a) Current density and light output power as the functions of applied voltage. (b) Current efficiency as the function of current density.

As we can see from Figure 6.6b, the performance of the OLED with 5nm MoO3 layer is obvious outstanding compared to others even for the 1nm and 10nm OLED which have just few nanometer difference of the spacer layer. These results indicate that the rapid distance dependent light-emission are not unique in our 2D material-DMD systems, and it may be a very fundamental and general process in plasmon-coupled light-matter interaction system which may benefit wide range of applications. In order to test the universality of this effect, we designed another OLED with simpler structure of ITO (130 nm)/PEDOT (40 nm)/Super yellow (70nm)/ BCP (10, 15, 20 nm)/Ag (100 nm) and did both EL and PL measurement for them (Figure 6.7). Here in this design, obviously the BCP layer is supposed to be spacer layer. As is shown is Figure 6.7b, it's obvious that the OLED with

15nm BCP spacer layer stands out compared to others with electrical pumping. Surprisingly, the measurement from PL signal also show similar results (Figure 6.7c) that there were more light coming out from the OLED structure with 15nm BCP spacer layer no matter the active layer were pumped electrically or optically. Though indeed the OLED system with electrical driving is a much more complex system as a lot of non-optical process should be taken into consideration like charge transfer/balancing, band structure, defect and interface issues, but the coherency from PL and EL results provide the evidence of their internal shared fundamental process, which indicates this optical-induced enhancement may play a dominated role in practical devices.

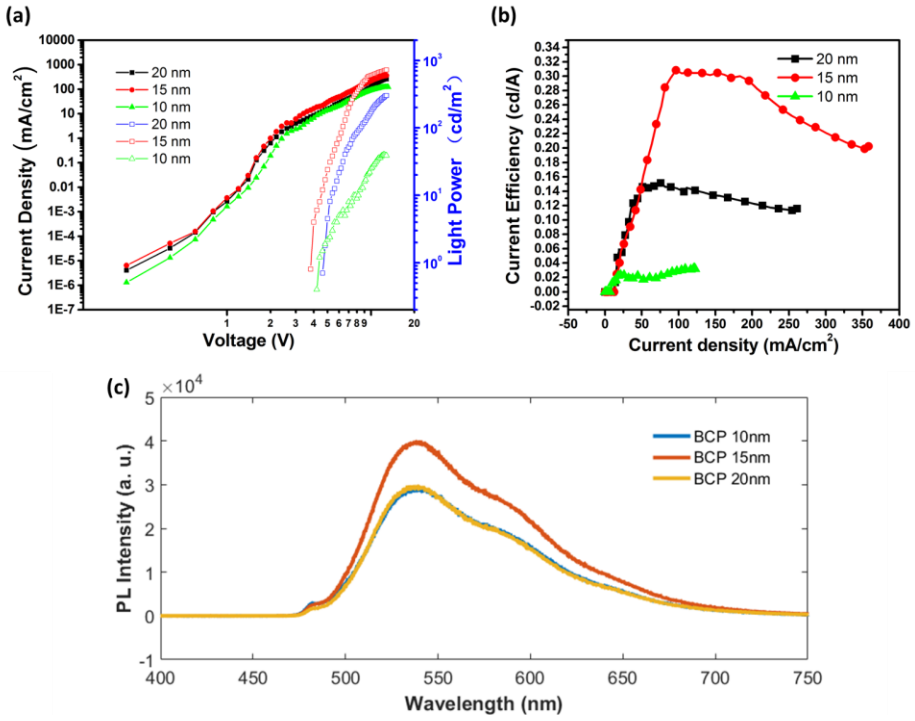


Figure 6.7: EL and PL characterization of OLED devices with structure of ITO (130 nm)/PEDOT (40 nm)/Super yellow (70nm)/ BCP (10, 15, 20 nm)/Ag (100 nm). (a) Current density and light output power as the functions of applied voltage. (b) Current efficiency as the function of current density. (c) Measured PL spectra.

## 6.5 Discussion: possible mechanism

As we discussed above, the most attractive finding of this chapter is the rapid separation distance dependence of the light emission. In order to find the explanation of this phenomena, an analysis based on semi-classical dipole radiation method [66], [67] have been used to study the exciton relaxation kinetics and light emission from the dipoles.

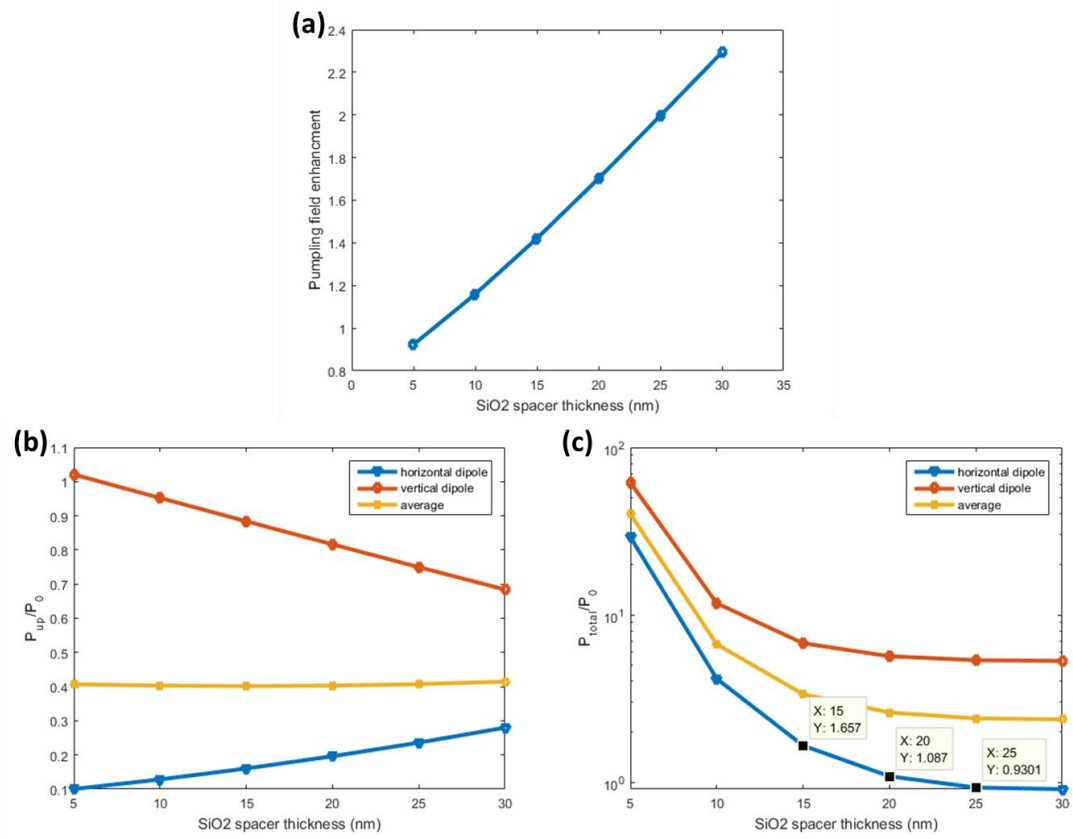


Figure 6.8: Calculated (a) Pumping field enhancement; (b) free photon emission; (c) total Purcell factor (local density of states) of emitting dipoles on the DMD structures of SiO2(5-30nm)/ Au(40nm)/ Glass.

Here Figure 6.8a shows the calculated enhancement due to pumping light by considering the local $|E|^2$ enhancement at the spacer/air interface where the emitters are located when a 532nm laser beam incident normally. The enhancement is comparing the case of DMD structure and the case on PDMS. As we can see here, the pumping field enhancement factor (EF) monotonically increases with the spacer thickness and by changing 5nm there is only very slightly change on the EF.

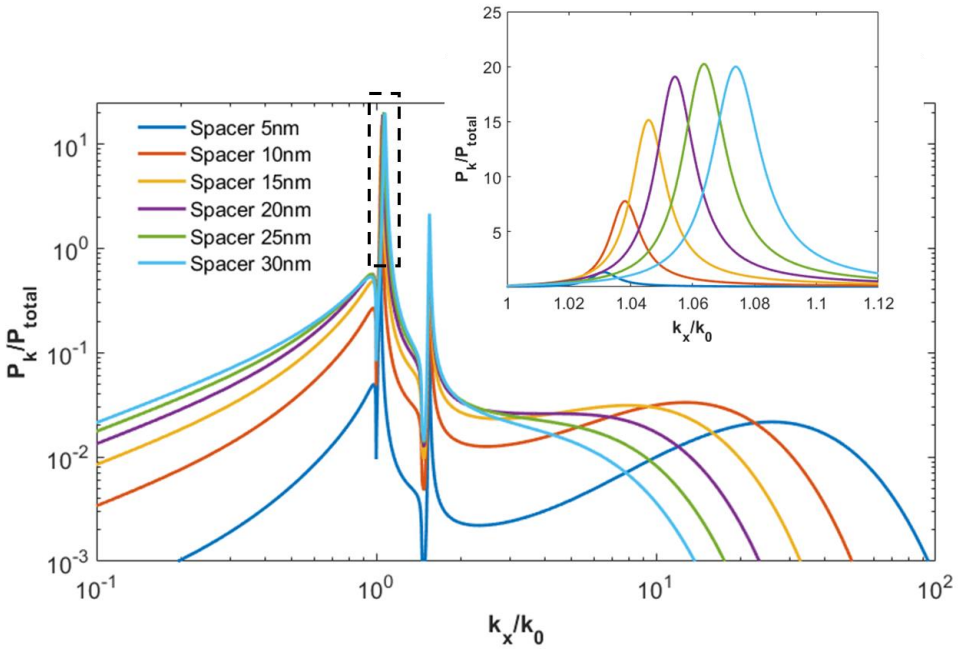


Figure 6.9: Calculated optical exciton relaxation channels in k space. The insert figure shows the zoom in plot of the SPP peaks.

Figure 6.9 shows the emitted energy from the emitter to different relaxation channels in k space. The method of the calculation has been already introduced in Chapter 4 and elsewhere [66], [67]. As different channels are competing with each other, the figure shows the results normalized to the total photonic density of states (Purcell factor). The region of 0 to k0 represent the emitted free photon contribution. The peaks around 1.06k0 and 1.55k0

represent the SPP modes on upper Au film/SiO2 spacer interface and on lower Au film/glass substrate interface respectively. The mode in the high k region (>2k0) are the so called high k lossy surface modes[67], which are considered as the main factor corresponding for the optically quenching near metal surface.

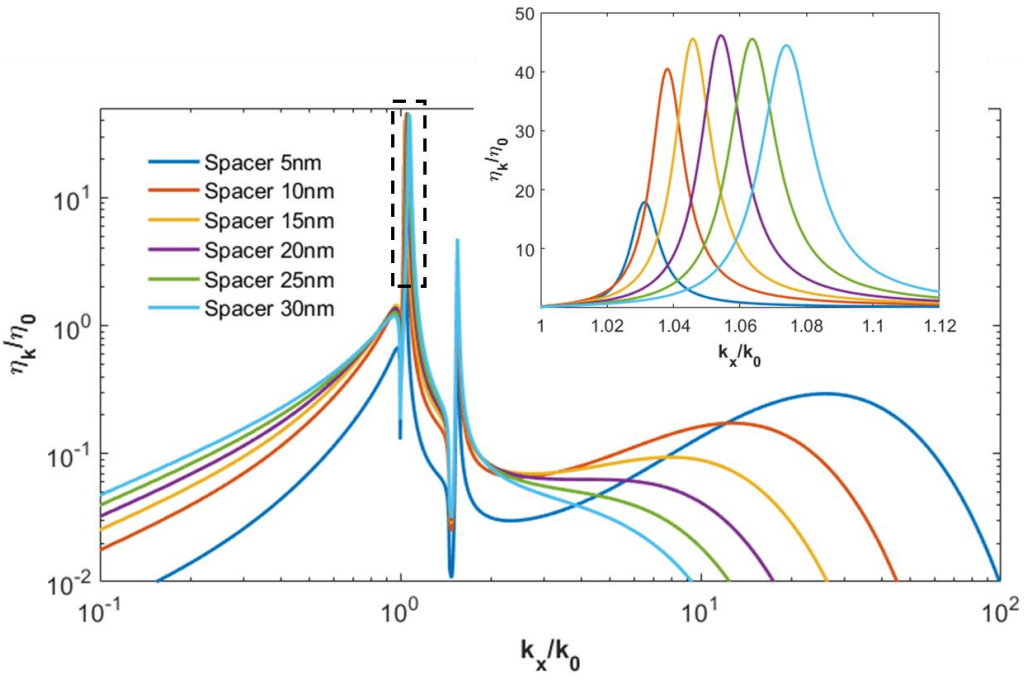


Figure 6.10: Calculated enhancement contribution due to optical exciton relaxation channels in k space. The insert figure shows the zoom in plot of the SPP peaks. An internal quantum yield of 5% is considered for WSe2.

However for a real case, not only the optical induced relaxation channels but also the internal non-radiative energy decay should be taken into consideration. Thus for emitter with total optical dissipation power of $P_0$ in vacuum and $P_{nonr}$ as the non-radiative decay power. The quantum yield defines as:

$$\eta_0 = \frac{P_0}{P_0 + P_{nonr}} \tag{6. 1}$$

So the contributions from each mode to the new quantum yield for the emitter at new environment can be written as:

$$\eta_{new} = \frac{P_k}{P_{total} + P_{nonr}} \tag{6. 2}$$

Thus, the contributions from each mode to the new quantum yield enhancement are:

$$\frac{\eta_k}{\eta_0} = \frac{P_k}{\eta_0 P_{total} + (1-\eta_0) P_0} \tag{6. 3}$$

Figure 6.10 shows the calculated quantum yield enhancement distribution in k space by taking the 5% QY of WSe2 monolayer[121], [122] into consideration. As we can see here, the SPP mode at the metal/spacer interface plays a key role defining the exciton relaxation channels. And more surprisingly, a maximal SPP peak were observed for the case of 20nm spacer, which indicates the possible correlation between the SPP mode and the separation dependent PL enhancement. Furthermore, we calculate the final enhancement based on this model by considering both the pumping field enhancement and the competing among different exciton relaxation channels (Figure 6.11). And only the free photons emitted to the upper space are considered as the contribution to the measured PL signal. The total QY enhancement for DMD structures:

$$\frac{\eta_{DMD}}{\eta_0} = \frac{P_{free\_\mathrm{DMD}}}{\eta_0 P_{total\_DMD} + (1-\eta_0) P_0} \tag{6. 4}$$

The total QY enhancement for PDMS:

$$\frac{\eta_{PDMS}}{\eta_0} = \frac{P_{free\_PDMS}}{\eta_0 P_{total\_\mathrm{PDMS}} + (1-\eta_0) P_0} \tag{6. 5}$$

So the total enhancement factor should be the product of QY enhancement and pumping field enhancement:

$$EF = \frac{\eta_{DMD}}{\eta_{PDMS}} \bullet \frac{|E|^2_{DMD}}{|E|^2_{PDMS}} \quad (6.6)$$

Figure 6.11 shows the calculated final EF and the comparison with experimental data. Though the case of 5nm, 10nm and 15nm match very well with the calculated cure for horizontal dipole, but the rapid enhancement drop after 20nm doesn't agree with the calculation. Thus new methods or new exciton relaxation process should be considered for understanding this phenomena.

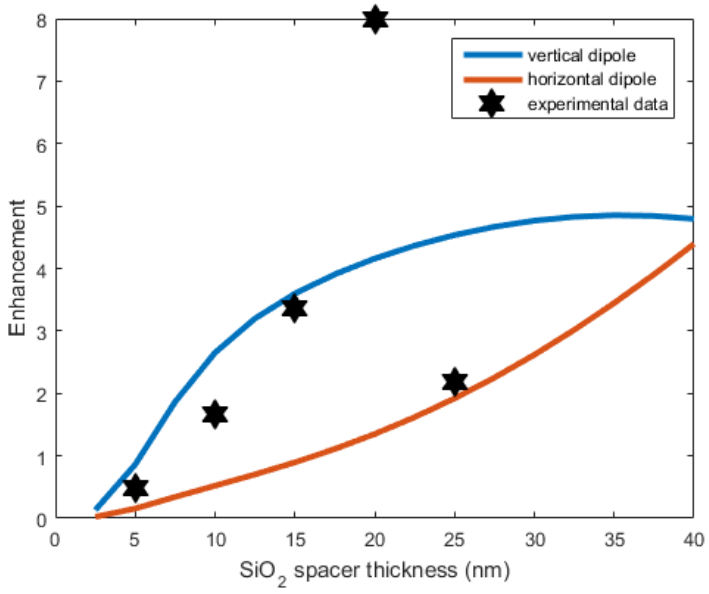


Figure 6.11: Calculated enhancement factor by using the classical conventional dipole emission method by considering both the pumping field enhancement and the competing among different exciton relaxation channels. Here only the free photons emitted to the upper space are considered as the contribution to the measured PL signal. The calculated curves are compared with the enhancement data from experiment.

Recently, a Forster resonance energy transfer (FRET) like non-radiative exciton-plasmon energy transfer process origin from the exciton-plasmon dipole-dipole electrostatic interaction have been demonstrated and widely discussed, which provides new possible

relaxation channels for excitons[123]–[126]. More interestingly, unlike conventional FRET process, this energy transfer process is revisable and even been used for solar energy conversion [124], which also provide the possibility of reuse the energy initially transferred to surface plasmon mode. Moreover, as this energy transfer origin from dipole-dipole interaction, it's also very sensitive to the separation distance with the law of ~$d^{-6}$ and can be written as[126]:

$$k_{SP} = \frac{k_{SP}^{0}}{1+\left(\frac{d}{d_{SP}}\right)^{6}} \tag{6. 7}$$

Here $k_{SP}$ is the rate of this exciton-SP transition and $k_{SP}^{0}$ is the limit of this rate when the separation distance is 0. And $d_{SP}$ is a length to measure the effective scale of this interaction, and it could be as long as up to 40nm as demonstrated in some previous works[125]. More recently, similar distance dependent light-emission phenomena have also been observed in quantum dots (QD)/Si3N4/Ag system [126]. In that work, rapid distance dependence was attribute to the competing of non-radiative exciton-SP energy transition and the charge transfer/tunneling crossing that thin spacer layer. As we discussed above, the energy coupled to SP mode is re-useable and can contribute to the final free photon. While the charge transfer process is purely non-radiative loss which can kill the exciton directly. The charge transfer rate can be write as:

$$k_{CT} = k_{CT}^{0} \exp\left(-\frac{d}{d_{CT}}\right) \tag{6. 8}$$

Here $k_{CT}$ is the rate of this charge transfer and $k_{CT}^{0}$ is the limit of this rate when the separation distance is 0. And $d_{CT}$ is a length to measure the effective scale of this process,

and it is usually in the scale of several nanometers. By using these assumptions, and setting several fitting parameters in their model such as $k_{SP}^{0}$, $d_{SP}$, $k_{CT}^{0}$ and $d_{CT}$, the author can fit their experimental very well based on this model [126].

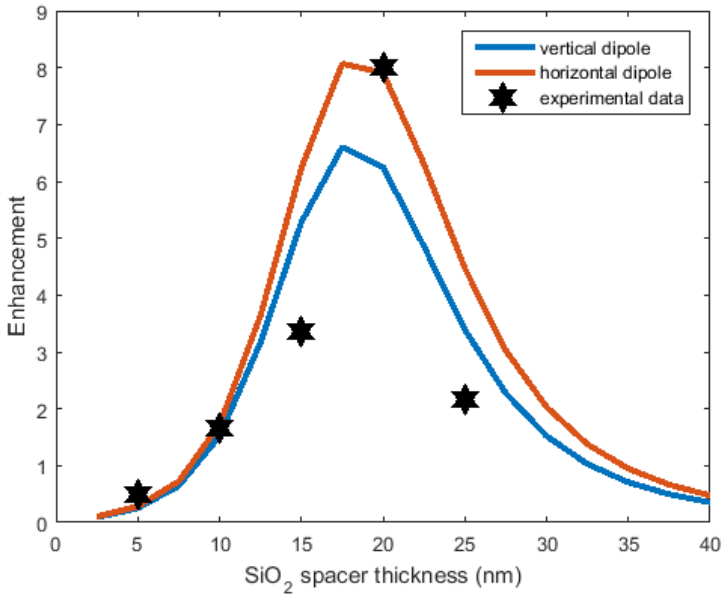


Figure 6.12: Calculated enhancement factor by considering the non-radiative exciton-SP energy transfer and charge transfer. Pumping field enhancement and the competing among different exciton relaxation channels are also considered. Here free photons emitted to the upper space and 20% of the SP energy are considered as the contribution to the measured PL signal. The calculated curves are compared with the enhancement data from experiment.

Here by considering the non-radiative exciton-SP energy transfer and charge transfer as new exciton relaxation channels and 20% of the SP energy as re-useable for the coming out light signal, we also obtain good fit with our experimental data with the fitting parameters as $k_{SP}^{0} = 1/0.8ns$, $d_{SP} = 18nm$, $k_{CT}^{0} = 1/12ps$ and $d_{CT} = 3nm$ (Figure 6.12). However, for a comprehensive explanation of the observed phenomena, more verification and experiments should be conduct to check the validity of these fitting parameters as well as the assumed physical process. For example, we could do a lifetime measurement of the

PL signal with pulse laser to study the distance dependence of the lifetime as did in some previous work about exciton-SP energy transfer. A $d^6$ ruler are supposed to be observed for the lifetime as the energy transfer rate should obey a $d^{-6}$ law.

## 6.6 Conclusions

This chapter presents a simple, planar, 3 layer DMD structure which dramatically enhances the light-emission from 2D materials. By changing the thickness of the spacer layer separating the 2D materials and the metal film, a very sensitive separation dependent PL signal enhancement as well as spectrum shift have been observed compared to the case of 2D materials on pure PDMS substrate. With an optimized structure of 20nm SiO2 spacer and 40nm Au film, an 8 times enhancement of the PL signal have been observed. When applied these structures to Supper Yellow based OLED system, similar separation dependent light-emission have been observed for both PL and EL measurements, which indicates the established phenomena is pretty general and applicable to other light-emission systems. Possible physics process and mechanism were also discussed, but it's still far to have a closed conclusion. Further investigation of the underlying physics such as non-radiative exciton-plasmon energy transfer and group coherency should be conducted. This planar, 3 layers, deep subwavelength DMD structure not only provide a general method to enhance light emission from active materials but also offer a good platform to study the fundamental physics of plasmon interacted exciton dynamics.

# Chapter 7

# Summary

The thesis is categorized into two parts: Periodic 1D/2D DNI nanopatterned surfaces and their applications for nanoparticle assembly/sorting and light-extraction; Planar metal/dielectrics multilayer structures and their applications for hyperbolic metamaterials and surface-plasmon-coupled light emission. These parts are closely correlated with each other, and represent some of the recent developments in the constituent materials and device designs for future optical/optoelectronic, microfluidic/biomedical device platforms.

In terms of the developments of new materials and new material fabrication, this thesis introduces two novel fundamental materials: (1) Dynamic Nanoinscribting pattering technique and the 1D/2D sinusoidal nanopatterned surface. (2) Ultrathin, low loss, Al-doped Ag films. This pattering technique enabled the single step, large area, scalable, low coast nanostructure pattering on flexible substrate, which itself is very promising in nanofabrication area. Compared to pure Ag films, doped Ag films are ultra-thin and smooth. They maintain the good optical and electrical properties of pure Ag films, while at the same time, have a significantly improved long-term and thermal stability, as well as a good adhesion to various substrates.

Novel materials and fabrication technique for sure is important, however this thesis mainly focus on how these fundamental materials and structures can be utilized in a smart way, leading to multidisciplinary applications. Based on 2D DNI patterned nanovoid structures and directed self-assembly of nanoparticles controlled by the geometric-induced electrostatic and entropic interactions, we experimentally demonstrate a single-step, low-cost methodology to selectively confine, pattern and sort nanoparticles based upon their size. This size-selective confinement is due to the free energy change of the system which arises from EDLs overlapping, ionic redistribution and the associated entropy change. This method could potentially be extended to scalable localization, sorting and manipulation of charged biological objects such as proteins, lipid vesicles, cancer cells and bacteria. We also introduce 1D DNI patterned nanogratings. Based on that, we experimentally demonstrate a single-step, low-cost methodology for light extraction from flip-chip GaN LED. This nanostructure induced light extraction were explained in the language of photon population exchange and momentum transferring by using a mixed level simulation in which both wave and particle nature of the photons are considered. Application of this light extraction method could be extended to scalable out-coupling of trapped photon modes in other systems like OLED and hyperbolic metamaterials.

Moreover, we discuss the applications of planar metal/dielectrics multilayers. Based on the low loss, ultrathin Al-doped Ag films, we experimentally demonstrated a high performance hyperbolic metamaterials (HMM). These HMMs show both a low-loss and homogenous

optical response. More important, they support much broader band of allowed high-k modes and higher photonic density of states (PDOS), which usually means a stronger light-matter interaction and is desired in many active photonic systems. HMMs based on even thinner building blocks (sub-nanometer metal films or 2D materials) are discussed theoretically. And we show the intrinsic limitation of these metamaterials: nonlocality origin from the quantum response of electrons (degeneracy pressure, diffusion kinetics and tunneling) will induce transition of the photonic topology of the HMM, making it not a HMM anymore. And this theory also explains the optical/plasmonic properties of some natural HMMs like graphite. Besides studying these passive metamaterials, we also study active system by integrating dielectrics/metal/dielectrics (DMD) structures with 2D semiconductor and OLED systems. For both 2D material-DMD system and SY based OLED system, a very sensitive separation dependent light emission enhancement as well as spectrum shift have been observed. Especially for OLED system, this separation dependent light-emission have been observed with both optical and electric pumping, which indicates the established phenomena is pretty general and applicable to other light-emission systems. Possible physics process and mechanism such as non-radiative exciton-plasmon energy transfer were also discussed, but it's still far to have a closed conclusion. Besides the light-enhancement applications, this planar, 3 layers, deep subwavelength DMD structure provides a good platform to study the fundamental physics of plasmon interacted exciton dynamics.

# Bibliography


[1] S. Zeng, D. Baillargeat, H.-P. Ho, and K.-T. Yong, "Nanomaterials enhanced surface plasmon resonance for biological and chemical sensing applications.," *Chem. Soc. Rev.*, vol. 43, no. 10, pp. 3426–52, 2014.

[2] M. R. Gonçalves, "Plasmonic nanoparticles: fabrication, simulation and experiments," *J. Phys. D. Appl. Phys.*, vol. 47, no. 21, p. 213001, 2014.

[3] X. Fan, W. Zheng, and D. J. Singh, "Light scattering and surface plasmons on small spherical particles," *Light Sci. Appl.*, vol. 3, no. 6, p. e179, 2014.

[4] A. Verma and F. Stellacci, "Effect of surface properties on nanoparticle-cell interactions," *Small*, vol. 6, no. 1. pp. 12–21, 2010.

[5] M. Lundqvist, J. Stigler, G. Elia, I. Lynch, T. Cedervall, and K. a Dawson, "Nanoparticle size and surface properties determine the protein corona with possible implications for biological impacts.," *Proc. Natl. Acad. Sci. U. S. A.*, vol. 105, no. 38, pp. 14265–14270, 2008.

[6] Y. Xia, H. Yang, and C. T. Campbell, "Nanoparticles for Catalysis," *Acc. Chem. Res.*, vol. 46, no. 8, pp. 1671–1672, 2013.

[7] D. T. Thompson, "Using gold nanoparticles for catalysis," *Nano Today*, vol. 2, no. 4, pp. 40–43, 2007.

[8] W. L. Wilson, P. F. Szajowski, and L. E. Brus, "Quantum confinement in size-selected, surface-oxidized silicon nanocrystals.," *Science*, vol. 262, no. 5137, pp. 1242–1244, 1993.

[9] R. Rosetti and L. Brus, "Electron-Hole Recombination Emission as a Probe of Surface Chemistry in Aqueous CdS Colloids," *J. Phys. Chem.*, vol. 86, no. 11, pp. 4470–4472, 1982.

[10] S. Colodrero, M. Ocaña, and H. Míguez, "Nanoparticle-based one-dimensional photonic crystals.," *Langmuir*, vol. 24, no. 9, pp. 4430–4, 2008.

[11] S.-H. Kim, S. Y. Lee, S.-M. Yang, and G.-R. Yi, "Self-assembled colloidal structures for photonics," *NPG Asia Mater.*, vol. 3, no. 1, pp. 25–33, 2011.

[12] D. Xia, J. Zhang, X. He, and S. R. J. Brueck, "Fabrication of three-dimensional photonic crystal structures by interferometric lithography and nanoparticle self-assembly," *Appl. Phys. Lett.*, vol. 93, no. 7, 2008.

[13] X. Chen, X. Yang, W. Fu, M. Xu, and H. Chen, "Enhanced performance of polymer solar cells with a monolayer of assembled gold nanoparticle films fabricated by Langmuir–Blodgett technique," *Mater. Sci. Eng. B*, vol. 178, no. 1, pp. 53–59, 2013.

[14] C. Farcau, H. Moreira, B. Viallet, J. Grisolia, and L. Ressier, "Tunable conductive nanoparticle wire arrays fabricated by convective self-assembly on nonpatterned substrates," *ACS Nano*, vol. 4, no. 12, pp. 7275–7282, 2010.

[15] H. Yan and N. Melosh, “Electronic devices: Nanoparticles make salty circuits,” *Nat Nano*, vol. advance on, Mar. 2016.
[16] B. Born, J. D. Krupa, S. Geoffroy-Gagnon, and J. F. Holzman, “Integration of photonic nanojets and semiconductor nanoparticles for enhanced all-optical switching,” *Nat Commun*, vol. 6, p. 8097, 2015.
[17] Y. Viero, G. Copie, D. Guérin, C. Krzeminski, D. Vuillaume, S. Lenfant, and F. Cleri, “High Conductance Ratio in Molecular Optical Switching of Functionalized Nanoparticle Self-Assembled Nanodevices,” *J. Phys. Chem. C*, vol. 119, no. 36, pp. 21173–21183, 2015.
[18] G. Si, Y. Zhao, J. Lv, M. Lu, F. Wang, H. Liu, N. Xiang, T. J. Huang, A. J. Danner, J. Teng, and Y. J. Liu, “Reflective plasmonic color filters based on lithographically patterned silver nanorod arrays.,” *Nanoscale*, vol. 5, no. 14, pp. 6243–8, 2013.
[19] C. Saeidi and D. van der Weide, “Bandwidth-tunable optical spatial filters with nanoparticle arrays,” *Opt Express*, vol. 22, no. 10, pp. 12499–12504, 2014.
[20] M. U. Sankar, S. Aigal, S. M. Maliyekkal, A. Chaudhary, Anshup, A. A. Kumar, K. Chaudhari, and T. Pradeep, “Biopolymer-reinforced synthetic granular nanocomposites for affordable point-of-use water purification.,” *Proc. Natl. Acad. Sci. U. S. A.*, vol. 110, no. 21, pp. 8459–64, 2013.
[21] J. He, M. Boegli, I. Bruzas, W. Lum, and L. Sagle, “Patterned Plasmonic Nanoparticle Arrays for Microfluidic and Multiplexed Biological Assays,” *Anal. Chem.*, vol. 87, no. 22, pp. 11407–11414, 2015.
[22] W. Tan, K. Wang, X. He, X. J. Zhao, T. Drake, L. Wang, and R. P. Bagwe, “Bionanotechnology based on silica nanoparticles,” *Medicinal Research Reviews*, vol. 24, no. 5. pp. 621–638, 2004.
[23] X. Zhao, L. R. Hilliard, S. J. Mechery, Y. Wang, R. P. Bagwe, S. Jin, and W. Tan, “A rapid bioassay for single bacterial cell quantitation using bioconjugated nanoparticles.,” *Proc. Natl. Acad. Sci. U. S. A.*, vol. 101, no. 42, pp. 15027–32, 2004.
[24] T. Kraus, L. Malaquin, H. Schmid, W. Riess, N. D. Spencer, and H. Wolf, “Nanoparticle printing with single-particle resolution.,” *Nat. Nanotechnol.*, vol. 2, no. 9, pp. 570–6, 2007.
[25] A. S. Urban, A. A. Lutich, F. D. Stefani, and J. Feldmann, “Laser printing single gold nanoparticles,” *Nano Lett.*, vol. 10, no. 12, pp. 4794–4798, 2010.
[26] P. Sajeesh and A. K. Sen, “Particle separation and sorting in microfluidic devices: A review,” *Microfluidics and Nanofluidics*, vol. 17, no. 1. pp. 1–52, 2014.
[27] M. Yamada, M. Nakashima, and M. Seki, “Pinched flow fractionation: Continuous size separation of particles utilizing a laminar flow profile in a pinched microchannel,” *Anal. Chem.*, vol. 76, no. 18, pp. 5465–5471, 2004.
[28] J. McGrath, M. Jimenez, and H. Bridle, “Deterministic lateral displacement for particle separation: a review.,” *Lab Chip*, vol. 14, no. 21, pp. 4139–58, 2014.
[29] M. T. Blom, E. Chmela, R. E. Oosterbroek, R. Tijssen, and A. Van Den Berg, “On-Chip Hydrodynamic Chromatography Separation and Detection of Nanoparticles and Biomolecules,” *Anal. Chem.*, vol. 75, no. 24, pp. 6761–6768,

2003.
[30] N. Surugau and P. L. Urban, “Electrophoretic methods for separation of nanoparticles,” *Journal of Separation Science*, vol. 32, no. 11. pp. 1889–1906, 2009.
[31] P. R. C. Gascoyne and J. Vykoukal, “Particle separation by dielectrophoresis,” *Electrophoresis*, vol. 23, no. 13. pp. 1973–1983, 2002.
[32] S. Ibsen, A. Sonnenberg, C. Schutt, R. Mukthavaram, Y. Yeh, I. Ortac, S. Manouchehri, S. Kesari, S. Esener, and M. J. Heller, “Recovery of Drug Delivery Nanoparticles from Human Plasma Using an Electrokinetic Platform Technology,” *Small*, vol. 11, no. 38, pp. 5088–5096, 2015.
[33] M. Krishnan, N. Mojarad, P. Kukura, and V. Sandoghdar, “Geometry-induced electrostatic trapping of nanometric objects in a fluid.,” *Nature*, vol. 467, no. 7316, pp. 692–695, 2010.
[34] J. G. Ok, A. Panday, T. Lee, and L. Jay Guo, “Continuous fabrication of scalable 2-dimensional (2D) micro- and nanostructures by sequential 1D mechanical patterning processes.,” *Nanoscale*, vol. 6, no. 24, pp. 14636–42, 2014.
[35] S. H. Ahn and L. Jay Guo, “Dynamic nanoinscribing for continuous and seamless metal and polymer nanogratings,” *Nano Lett.*, vol. 9, no. 12, pp. 4392–4397, 2009.
[36] M. Krishnan, “Electrostatic free energy for a confined nanoscale object in a fluid,” *J. Chem. Phys.*, vol. 138, no. 11, 2013.
[37] D. a Walker, B. Kowalczyk, M. O. de la Cruz, and B. a Grzybowski, “Electrostatics at the nanoscale.,” *Nanoscale*, vol. 3, no. 4, pp. 1316–1344, 2011.
[38] V. A. Parsegian and D. Gingell, “On the electrostatic interaction across a salt solution between two bodies bearing unequal charges.,” *Biophys. J.*, vol. 12, no. 9, pp. 1192–204, 1972.
[39] S. Nakamura, M. Senoh, and T. Mukai, “P-gan/n-ingan/n-gan double-heterostructure blue-light-emitting diodes,” *Jpn. J. Appl. Phys.*, vol. 32, no. 1 A, pp. L8–L11, 1993.
[40] S. N. Mohammad, A. A. Salvador, and H. Morkoc, “Emerging gallium nitride based devices,” *Proc. IEEE*, vol. 83, no. 10, pp. 1306–1355, 1995.
[41] Q. Zhang, K. H. Li, and H. W. Choi, “InGaN light-emitting diodes with indium-tin-oxide sub-micron lenses patterned by nanosphere lithography,” *Appl. Phys. Lett.*, vol. 100, no. 6, 2012.
[42] Y. K. Ee, P. Kumnorkaew, R. A. Arif, H. Tong, H. Zhao, J. F. Gilchrist, and N. Tansu, “Optimization of light extraction efficiency of III-nitride LEDs with self-assembled colloidal-based microlenses,” *IEEE J. Sel. Top. Quantum Electron.*, vol. 15, no. 4, pp. 1218–1225, 2009.
[43] G. Li, W. Wang, W. Yang, Y. Lin, H. Wang, Z. Lin, and S. Zhou, “GaN-based light-emitting diodes on various substrates: a critical review,” *Reports Prog. Phys.*, vol. 79, no. 5, p. 56501, 2016.
[44] H.-Y. Lin, Y.-H. Ho, J.-H. Lee, K.-Y. Chen, J.-H. Fang, S.-C. Hsu, M.-K. Wei, H.-Y. Lin, J.-H. Tsai, and T.-C. Wu, “Patterned microlens array for efficiency improvement of small-pixelated organic light-emitting devices.,” *Opt. Express*, vol. 16, no. 15, pp. 11044–51, 2008.

[45] S. Möller and S. R. Forrest, “Improved light out-coupling in organic light emitting diodes employing ordered microlens arrays,” *J. Appl. Phys.*, vol. 91, no. 5, pp. 3324–3327, 2002.
[46] Y. Sun and S. R. Forrest, “Organic light emitting devices with enhanced outcoupling via microlenses fabricated by imprint lithography,” *J. Appl. Phys.*, vol. 100, no. 7, 2006.
[47] T. Yamasaki, K. Sumioka, and T. Tsutsui, “Organic light-emitting device with an ordered monolayer of silica microspheres as a scattering medium,” *Appl. Phys. Lett.*, vol. 76, no. 10, p. 1243, 2000.
[48] H. N. S. Krishnamoorthy, Z. Jacob, E. Narimanov, I. Kretzschmar, and V. M. Menon, “Topological transitions in metamaterials.,” *Science*, vol. 336, no. 6078, pp. 205–209, 2012.
[49] Y. Guo, C. L. Cortes, S. Molesky, and Z. Jacob, “Broadband super-Planckian thermal emission from hyperbolic metamaterials,” *Appl. Phys. Lett.*, vol. 101, no. 13, p. 131106, 2012.
[50] S. Ishii, A. V Kildishev, E. Narimanov, V. M. Shalaev, and V. P. Drachev, “Sub-wavelength interference pattern from volume plasmon polaritons in a hyperbolic medium,” *Laser Photon. Rev.*, vol. 7, no. 2, pp. 265–271, 2013.
[51] X. Yang, J. Yao, J. Rho, X. Yin, and X. Zhang, “Experimental realization of three-dimensional indefinite cavities at the nanoscale with anomalous scaling laws,” *Nat. Photonics*, vol. 6, no. 7, pp. 450–454, 2012.
[52] J. Zhou, A. F. Kaplan, L. Chen, and L. J. Guo, “Experiment and Theory of the Broadband Absorption by a Tapered Hyperbolic Metamaterial Array,” *ACS Photonics*, vol. 1, no. 7, pp. 618–624, Jul. 2014.
[53] P. R. West, S. Ishii, G. V. Naik, N. K. Emani, V. M. Shalaev, and A. Boltasseva, “Searching for better plasmonic materials,” *Laser and Photonics Reviews*, vol. 4, no. 6. pp. 795–808, 2010.
[54] V. J. Logeeswaran, N. P. Kobayashi, M. S. Islam, W. Wu, P. Chaturvedi, N. X. Fang, S. Y. Wang, and R. S. Williams, “Ultrasmooth silver thin films deposited with a germanium nucleation layer,” *Nano Lett.*, vol. 9, no. 1, pp. 178–182, 2009.
[55] K. Thürmer, E. Williams, and J. Reutt-Robey, “Dewetting dynamics of ultrathin silver films on Si(111),” *Phys. Rev. B*, vol. 68, no. 15, pp. 1–7, 2003.
[56] H. Krishna, R. Sachan, J. Strader, C. Favazza, M. Khenner, and R. Kalyanaraman, “Thickness-dependent spontaneous dewetting morphology of ultrathin Ag films.,” *Nanotechnology*, vol. 21, no. 15, p. 155601, 2010.
[57] H. C. Kim, T. L. Alford, and D. R. Allee, “Thickness dependence on the thermal stability of silver thin films,” *Appl. Phys. Lett.*, vol. 81, no. 22, pp. 4287–4289, 2002.
[58] P. Nagpal, N. C. Lindquist, S.-H. Oh, and D. J. Norris, “Ultrasmooth patterned metals for plasmonics and metamaterials.,” *Science*, vol. 325, no. 5940, pp. 594–7, 2009.
[59] C. Zhang, D. Zhao, D. Gu, H. Kim, T. Ling, Y. K. R. Wu, and L. J. Guo, “An ultrathin, smooth, and low-loss Al-doped Ag film and its application as a transparent electrode in organic photovoltaics,” *Adv. Mater.*, vol. 26, no. 32, pp.

5696–5701, 2014.
[60] D. Gu, C. Zhang, Y. K. Wu, and L. J. Guo, “Ultrasmooth and thermally stable silver-based thin films with subnanometer roughness by aluminum doping,” *ACS Nano*, vol. 8, no. 10, pp. 10343–10351, 2014.
[61] J. N. Hilfiker, N. Singh, T. Tiwald, D. Convey, S. M. Smith, J. H. Baker, and H. G. Tompkins, “Survey of methods to characterize thin absorbing films with Spectroscopic Ellipsometry,” *Thin Solid Films*, vol. 516, no. 22, pp. 7979–7989, 2008.
[62] W. A. McGahan, B. Johs, and J. A. Woollam, “Techniques for ellipsometric measurement of the thickness and optical constants of thin absorbing films,” *Thin Solid Films*, vol. 234, no. 1–2, pp. 443–446, 1993.
[63] A. Poddubny, I. Iorsh, P. Belov, and Y. Kivshar, “Hyperbolic metamaterials,” *Nat. Photonics*, vol. 7, no. 12, pp. 948–957, 2013.
[64] T. Xu and H. J. Lezec, “Visible-frequency asymmetric transmission devices incorporating a hyperbolic metamaterial,” *Nat Commun*, vol. 5, no. May, p. 4141, 2014.
[65] L. Gu, T. U. Tumkur, G. Zhu, and M. a Noginov, “Blue shift of spontaneous emission in hyperbolic metamaterial.,” *Sci. Rep.*, vol. 4, p. 4969, 2014.
[66] W. L. Barnes, “Fluorescence near interfaces: the role of photonic mode density,” *J. Mod. Opt.*, vol. 45, no. 4, pp. 661–699, 1998.
[67] G. W. Ford and W. H. Weber, “Electromagnetic interactions of molecules with metal surfaces,” *Physics Reports*, vol. 113, no. 4. pp. 195–287, 1984.
[68] J. Yang, X. Hu, X. Li, Z. Liu, X. Jiang, and J. Zi, “Cancellation of reflection and transmission at metamaterial surfaces.,” *Opt. Lett.*, vol. 35, no. 1, pp. 16–18, 2010.
[69] A. a. Orlov, P. M. Voroshilov, P. a. Belov, and Y. S. Kivshar, “Engineered optical nonlocality in nanostructured metamaterials,” *Phys. Rev. B - Condens. Matter Mater. Phys.*, vol. 84, no. 4, pp. 1–4, 2011.
[70] S. Dai, Q. Ma, M. K. Liu, T. Andersen, Z. Fei, M. D. Goldflam, M. Wagner, K. Watanabe, T. Taniguchi, M. Thiemens, F. Keilmann, G. C. a M. Janssen, S.-E. Zhu, P. Jarillo-Herrero, M. M. Fogler, and D. N. Basov, “Graphene on hexagonal boron nitride as a tunable hyperbolic metamaterial.,” *Nat. Nanotechnol.*, no. June, pp. 1–6, 2015.
[71] G. V Naik, B. Saha, J. Liu, S. M. Saber, E. a Stach, J. M. K. Irudayaraj, T. D. Sands, V. M. Shalaev, and A. Boltasseva, “Epitaxial superlattices with titanium nitride as a plasmonic component for optical hyperbolic metamaterials.,” *Proc. Natl. Acad. Sci. U. S. A.*, vol. 111, no. 21, pp. 7546–51, 2014.
[72] C. Zhang, L. Chen, and L. J. Guo, “Ultrathin and Smooth Silver Film by Aluminum-doping and Applications in Plasmonics and Meta-materials - OSA Technical Digest (online),” in *Frontiers in Optics 2014*, 2014, p. FTu1E.7.
[73] C. Ciraci, R. T. Hill, J. J. Mock, Y. Urzhumov, a. I. Fernandez-Dominguez, S. a. Maier, J. B. Pendry, a. Chilkoti, and D. R. Smith, “Probing the Ultimate Limits of Plasmonic Enhancement,” *Science (80-. ).*, vol. 337, no. 6098, pp. 1072–1074, 2012.
[74] C. Ciracì, J. B. Pendry, and D. R. Smith, “Hydrodynamic model for plasmonics: A

macroscopic approach to a microscopic problem," *ChemPhysChem*, vol. 14, pp. 1109–1116, 2013.
[75] N. a Mortensen, S. Raza, M. Wubs, T. Søndergaard, and S. I. Bozhevolnyi, "A generalized non-local optical response theory for plasmonic nanostructures.," *Nat. Commun.*, vol. 5, no. May, p. 3809, 2014.
[76] G. Toscano, J. Straubel, A. Kwiatkowski, C. Rockstuhl, F. Evers, H. Xu, N. Asger Mortensen, and M. Wubs, "Resonance shifts and spill-out effects in self-consistent hydrodynamic nanoplasmonics," *Nat. Commun.*, vol. 6, no. May, p. 7132, 2015.
[77] Y. Luo, a. I. Fernandez-Dominguez, A. Wiener, S. a. Maier, and J. B. Pendry, "Surface plasmons and nonlocality: A simple model," *Phys. Rev. Lett.*, vol. 111, no. 9, pp. 1–5, 2013.
[78] A. Wiener, A. I. Fernández-Domínguez, A. P. Horsfield, J. B. Pendry, and S. a. Maier, "Nonlocal effects in the nanofocusing performance of plasmonic tips," *Nano Lett.*, vol. 12, pp. 3308–3314, 2012.
[79] C. David and F. J. García De Abajo, "Spatial nonlocality in the optical response of metal nanoparticles," *J. Phys. Chem. C*, vol. 115, no. 40, pp. 19470–19475, 2011.
[80] S. Raza, T. Christensen, M. Wubs, S. I. Bozhevolnyi, and N. A. Mortensen, "Nonlocal response in thin-film waveguides: Loss versus nonlocality and breaking of complementarity," *Phys. Rev. B - Condens. Matter Mater. Phys.*, vol. 88, no. 11, pp. 1–9, 2013.
[81] S. Raza, M. Wubs, S. I. Bozhevolnyi, and N. A. Mortensen, "Nonlocal study of ultimate plasmon hybridization," *Opt. Lett.*, vol. 40, no. 5, p. 839, 2015.
[82] C. David and F. J. Garcia de Abajo, "Surface plasmon dependence on the electron density profile at metal surfaces.," *ACS Nano*, no. 9, pp. 9558–9566, 2014.
[83] W. Yan, N. A. Mortensen, and M. Wubs, "Hyperbolic metamaterial lens with hydrodynamic nonlocal response," *Opt. Express*, vol. 21, no. 12, pp. 15026–15036, 2013.
[84] W. Yan, M. Wubs, and N. A. Mortensen, "Hyperbolic metamaterials: Nonlocal response regularizes broadband supersingularity," *Phys. Rev. B - Condens. Matter Mater. Phys.*, vol. 86, no. 20, pp. 1–8, 2012.
[85] a. Moreau, C. Ciracì, and D. R. Smith, "Impact of nonlocal response on metallodielectric multilayers and optical patch antennas," *Phys. Rev. B - Condens. Matter Mater. Phys.*, vol. 87, no. 4, pp. 1–11, 2013.
[86] S. Raza, S. I. Bozhevolnyi, M. Wubs, and N. A. Mortensen, "Nonlocal optical response in metallic nanostructures," *J. Phys. Condens. Matter*, vol. 27, p. 183204, 2015.
[87] C. L. Cortes, W. Newman, S. Molesky, and Z. Jacob, "Quantum nanophotonics using hyperbolic metamaterials," *J. Opt.*, vol. 14, no. 6, p. 063001, 2012.
[88] T. Xu and H. J. Lezec, "Visible-frequency asymmetric transmission devices incorporating a hyperbolic metamaterial.," *Nat. Commun.*, vol. 5, no. May, p. 4141, 2014.
[89] E. H. Hwang and S. Das Sarma, "Dielectric function, screening, and plasmons in two-dimensional graphene," *Phys. Rev. B - Condens. Matter Mater. Phys.*, vol. 75, no. 20, pp. 1–6, 2007.

[90] B. Wunsch, T. Stauber, F. Sols, and F. Guinea, “Dynamical polarization of graphene at finite doping,” *New J. Phys.*, vol. 8, no. 12, p. 318, 2006.
[91] M. Jablan, H. Buljan, and M. Soljačić, “Plasmonics in graphene at infrared frequencies,” *Phys. Rev. B - Condens. Matter Mater. Phys.*, vol. 80, no. 24, pp. 1–7, 2009.
[92] D. Correas-Serrano, J. S. Gomez-Diaz, M. Tymchenko, and A. Alù, “Nonlocal response of hyperbolic metasurfaces,” *Opt. Express*, vol. 23, no. 23, pp. 29434–29448, Nov. 2015.
[93] J. S. Gomez-Diaz, M. Tymchenko, and A. Alu, “Hyperbolic Plasmons and Topological Transitions Over Uniaxial Metasurfaces,” *Phys. Rev. Lett.*, vol. 114, no. 23, p. 233901, 2015.
[94] P. Wachsmuth, R. Hambach, G. Benner, and U. Kaiser, “Plasmon bands in multilayer graphene,” *Phys. Rev. B*, vol. 90, no. 23, p. 235434, Dec. 2014.
[95] A. Politano and G. Chiarello, “Plasmon modes in graphene: status and prospect,” *Nanoscale*, vol. 6, no. 19, pp. 10927–10940, 2014.
[96] X. Luo, T. Qiu, W. Lu, and Z. Ni, “Plasmons in graphene: Recent progress and applications,” *Mater. Sci. Eng. R Reports*, vol. 74, no. 11, pp. 351–376, 2013.
[97] W. Yan, M. Wubs, and N. Asger Mortensen, “Projected Dipole Model for Quantum Plasmonics,” *Phys. Rev. Lett.*, vol. 115, no. 13, p. 137403, Sep. 2015.
[98] Y.-C. Chang, C.-H. Liu, C.-H. Liu, Z. Zhong, and T. B. Norris, “Extracting the complex optical conductivity of mono- and bilayer graphene by ellipsometry,” *Appl. Phys. Lett.*, vol. 104, no. 26, p. 261909, 2014.
[99] R. Warmbier, G. S. Manyali, and A. Quandt, “Surface plasmon polaritons in lossy uniaxial anisotropic materials,” *Phys. Rev. B*, vol. 85, no. 8, p. 085442, 2012.
[100] V. N. Kotov, B. Uchoa, V. M. Pereira, F. Guinea, and a. H. Castro Neto, “Electron-electron interactions in graphene: Current status and perspectives,” *Rev. Mod. Phys.*, vol. 84, no. 3, pp. 1067–1125, 2012.
[101] K. W.-K. Shung, “Dielectric function and plasmon structure of stage-1 intercalated graphite,” *Phys. Rev. B*, vol. 34, no. 2, pp. 426–429, 1986.
[102] M. a K. Othman, C. Guclu, and F. Capolino, “Graphene-based tunable hyperbolic metamaterials and enhanced near-field absorption.,” *Opt. Express*, vol. 21, no. 6, pp. 7614–32, 2013.
[103] T. Zhan, X. Shi, Y. Dai, X. Liu, and J. Zi, “Transfer matrix method for optics in graphene layers.,” *J. Phys. Condens. Matter*, vol. 25, no. 21, p. 215301, 2013.
[104] I. V Iorsh, I. S. Mukhin, I. V Shadrivov, P. A. Belov, and Y. S. Kivshar, “Hyperbolic metamaterials based on multilayer graphene structures,” *Phys. Rev. B*, vol. 87, no. 7, p. 75416, Feb. 2013.
[105] J. Sun, J. Zhou, B. Li, and F. Kang, “Indefinite permittivity and negative refraction in natural material: Graphite,” *Appl. Phys. Lett.*, vol. 98, no. 10, p. 101901, 2011.
[106] E. E. Narimanov and A. V. Kildishev, “Metamaterials: Naturally hyperbolic,” *Nat. Photonics*, vol. 9, no. 4, pp. 214–216, 2015.
[107] K. Korzeb, M. Gajc, and D. A. Pawlak, “Compendium of natural hyperbolic materials,” *Opt. Express*, vol. 23, no. 20, pp. 25406–25424, Oct. 2015.
[108] J. S. Ross, P. Klement, A. M. Jones, N. J. Ghimire, J. Yan, D. G. Mandrus, T.

Taniguchi, K. Watanabe, K. Kitamura, W. Yao, D. H. Cobden, and X. Xu, "Electrically tunable excitonic light-emitting diodes based on monolayer WSe2 p-n junctions.," *Nat. Nanotechnol.*, vol. 9, no. 4, pp. 268–72, 2014.
[109] B. Radisavljevic, A. Radenovic, J. Brivio, V. Giacometti, and A. Kis, "Single-layer MoS2 transistors," *Nat. Nanotechnol.*, vol. 6, no. 3, pp. 147–50, 2011.
[110] M. Chiu, C. Zhang, H. Shiu, C. Chuu, C.-H. Chen, C. S. Chang, C. Chen, M. Chou, C. Shih, and L. Li, "Determination of band alignment in the single-layer MoS2/WSe2 heterojunction.," *Nat. Commun.*, vol. 6, no. May, p. 7666, 2015.
[111] P. Tonndorf, R. Schmidt, P. Böttger, X. Zhang, J. Börner, A. Liebig, M. Albrecht, C. Kloc, O. Gordan, D. R. T. Zahn, S. Michaelis de Vasconcellos, and R. Bratschitsch, "Photoluminescence emission and Raman response of monolayer MoS_2, MoSe_2, and WSe_2," *Opt. Express*, vol. 21, no. 4, p. 4908, 2013.
[112] Z. Wang, Z. Dong, Y. Gu, Y.-H. Chang, L. Zhang, L.-J. Li, W. Zhao, G. Eda, W. Zhang, G. Grinblat, S. A. Maier, J. K. W. Yang, C.-W. Qiu, and A. T. S. Wee, "Giant photoluminescence enhancement in tungsten-diselenide–gold plasmonic hybrid structures," *Nat. Commun.*, vol. 7, no. May, p. 11283, 2016.
[113] K. C. J. Lee, Y.-H. Chen, H.-Y. Lin, C.-C. Cheng, P.-Y. Chen, T.-Y. Wu, M.-H. Shih, K.-H. Wei, L.-J. Li, and C.-W. Chang, "Plasmonic Gold Nanorods Coverage Influence on Enhancement of the Photoluminescence of Two-Dimensional MoS2 Monolayer," *Sci. Rep.*, vol. 5, p. 16374, 2015.
[114] B. Lee, J. Park, G. H. Han, H. S. Ee, C. H. Naylor, W. Liu, A. T. C. Johnson, and R. Agarwal, "Fano resonance and spectrally modified photoluminescence enhancement in monolayer MoS<inf>2</inf> integrated with plasmonic nanoantenna array," *Nano Lett.*, vol. 15, no. 5, pp. 3646–3653, 2015.
[115] S. Najmaei, A. Mlayah, A. Arbouet, C. Girard, J. Léotin, and J. Lou, "Plasmonic pumping of excitonic photoluminescence in hybrid MoS2-Au nanostructures," *ACS Nano*, vol. 8, no. 12, pp. 12682–12689, 2014.
[116] K. M. Goodfellow, R. Beams, C. Chakraborty, L. Novotny, and a N. Vamivakas, "Integrated nanophotonics based on nanowire plasmons and atomically thin material," *Optica*, vol. 1, no. 3, p. 149, 2014.
[117] H. S. Lee, M. S. Kim, Y. Jin, G. H. Han, Y. H. Lee, and J. Kim, "Efficient Exciton-Plasmon Conversion in Ag Nanowire/Monolayer MoS<inf>2</inf> Hybrids: Direct Imaging and Quantitative Estimation of Plasmon Coupling and Propagation," *Adv. Opt. Mater.*, vol. 3, no. 7, pp. 943–947, 2015.
[118] A. N. Sidorov, G. W. Sławiński, A. H. Jayatissa, F. P. Zamborini, and G. U. Sumanasekera, "A surface-enhanced Raman spectroscopy study of thin graphene sheets functionalized with gold and silver nanostructures by seed-mediated growth," *Carbon N. Y.*, vol. 50, no. 2, pp. 699–705, 2012.
[119] Z. Li, Y. Xiao, Y. Gong, Z. Wang, Y. Kang, S. Zu, P. M. Ajayan, P. Nordlander, and Z. Fang, "Active Light Control of the MoS2 Monolayer Exciton Binding Energy," *ACS Nano*, vol. 9, no. 10, pp. 10158–10164, 2015.
[120] M. O. Scully and A. A. Svidzinsky, "The Super of Superradiance," *Science (80-. ).*, vol. 325, no. September, pp. 1510–1512, 2009.
[121] M. Palummo, M. Bernardi, and J. C. Grossman, "Exciton radiative lifetimes in

two-dimensional transition metal dichalcogenides," *Nano Lett.*, vol. 15, no. 5, pp. 2794–2800, 2015.
[122] S. Wu, S. Buckley, A. M. Jones, J. S. Ross, N. J. Ghimire, J. Yan, D. G. Mandrus, W. Yao, F. Hatami, J. Vučković, A. Majumdar, and X. Xu, "Control of two-dimensional excitonic light emission via photonic crystal," *2D Mater.*, vol. 1, no. 1, p. 011001, 2014.
[123] Q. Zhang, G. Li, X. Liu, F. Qian, Y. Li, T. C. Sum, C. M. Lieber, and Q. Xiong, "A room temperature low-threshold ultraviolet plasmonic nanolaser.," *Nat. Commun.*, vol. 5, p. 4953, 2014.
[124] J. Li, S. K. Cushing, F. Meng, T. R. Senty, A. D. Bristow, and N. Wu, "Plasmon-induced resonance energy transfer for solar energy conversion," *Nat. Photonics*, vol. 9, no. 9, pp. 601–607, 2015.
[125] A. Kumar, P. Tyagi, R. Srivastava, D. S. Mehta, and M. N. Kamalasanan, "Energy transfer process between exciton and surface plasmon: Complete transition from Forster to surface energy transfer," *Appl. Phys. Lett.*, vol. 102, no. 20, 2013.
[126] T. Shin, K.-S. Cho, D.-J. Yun, J. Kim, X.-S. Li, E.-S. Moon, C.-W. Baik, S. Il Kim, M. Kim, J. H. Choi, G.-S. Park, J.-K. Shin, S. Hwang, and T.-S. Jung, "Exciton Recombination, Energy-, and Charge Transfer in Single- and Multilayer Quantum-Dot Films on Silver Plasmonic Resonators," *Sci. Rep.*, vol. 6, p. 26204, May 2016.